

**NATIONAL AERONAUTICS AND
SPACE ADMINISTRATION**

**TECHNICAL REPORT
R-93**

**THEORETICAL AND EXPERIMENTAL INVESTIGATION OF
SUPERCAVITATING HYDROFOILS OPERATING
NEAR THE FREE WATER SURFACE**

By VIRGIL E. JOHNSON, JR.

1961

*1N-34
380335
P. 82*

NASA TR R-93

TECHNICAL REPORT R-93

THEORETICAL AND EXPERIMENTAL INVESTIGATION OF SUPERCAVITATING HYDROFOILS OPERATING NEAR THE FREE WATER SURFACE

By VIRGIL E. JOHNSON, JR.

**Langley Research Center
Langley Field, Va.**

TECHNICAL REPORT R-93

THEORETICAL AND EXPERIMENTAL INVESTIGATION OF SUPERCAVITATING HYDROFOILS OPERATING NEAR THE FREE WATER SURFACE ¹

By VIRGIL E. JOHNSON, Jr.

SUMMARY

The linearized theory for infinite depth is applied to the design of two new low-drag supercavitating hydrofoils. The linearized solution for the characteristics of supercavitating hydrofoils operating at zero cavitation number at finite depth is also accomplished. The effects of camber determined from the linear theory are combined with the exact nonlinear flat-plate solution to produce nonlinear expressions for the characteristics of arbitrary sections. The resulting theoretical expressions are corrected for aspect ratio by conventional aeronautical methods.

An experimental investigation was made in Langley tank no. 2 of two aspect-ratio-1 hydrofoils, one with a flat surface and one with a cambered lower surface. A zero cavitation number was obtained in the tank by operating the hydrofoils near the free water surface so that their upper surfaces were completely ventilated. Some data were also obtained on these sections at finite cavitation numbers. For the condition of zero cavitation number the theoretical expressions developed are compared with the results of the present experimental investigation and with experimental results from other sources. Agreement between theory and experiment is found to be good for the lift coefficient, drag coefficient, center of pressure, and location of the upper cavity streamline provided the magnitude of camber is not excessive.

The theory is used to compare the maximum lift-drag ratios obtainable from various cambered sections of approximately equal strength. The analysis reveals that the maximum lift-drag ratio is not greatly dependent on the type of camber and that for operation at depths greater than about 1 chord, a lift-drag ratio of about 10 is close to the maximum

value that can be attained on a single hydrofoil supported by one strut and operating at speeds in excess of 80 knots at zero cavitation number.

INTRODUCTION

The desirability of using an auxiliary lifting surface such as a hydro-ski for reducing seaplane hull loads and for improving rough-water performance has been established. It is possible that hydrofoils with higher aspect ratio and thus higher efficiencies could be superior to the hydro-ski; however, only the low-aspect-ratio planing hydro-ski has so far been successfully applied as landing gear to modern high-speed aircraft because the conventional hydrofoil presents problems not experienced by a hydro-ski.

As a hydrofoil nears the free surface (during a take-off run) the low-pressure side of the hydrofoil almost always becomes ventilated from the atmosphere. This phenomenon results in a severe and usually abrupt loss in lift and a reduction in the lift-drag ratio. For conventional airfoil sections the loss in lift may exceed 75 percent. The speed at the inception of ventilation depends on the angle of attack and depth of submersion; however, except for very small angles of attack and relatively low take-off speeds, the inception speed is usually well below the take-off speed of the aircraft.

Even if the ventilation problem is overcome by using small angles of attack and incorporating "fences" or other devices for suppressing ventilation, the onset of cavitation presents a second deterrent to the use of conventional hydrofoils at high speeds. The loss in lift accompanying cavitation of conventional airfoil sections is not

¹ Supersedes declassified NACA Research Memorandum L57G11a and NACA Research Memorandum L57I16 by Virgil E. Johnson, Jr., 1957.

abrupt, but the ultimate reduction in lift and lift-drag ratio is comparable to that of ventilated flow. Even thin airfoil sections of small design lift coefficient start to cavitate and experience poor lift-drag ratios at speeds in excess of about 80 knots.

Since the take-off speed of supersonic aircraft may be in the range of 150 to 200 knots, lifting surfaces with cavitating or ventilating characteristics superior to those of conventional airfoil sections are desirable. Fortunately, the theoretical work of Tulin and Burkart (ref. 1) has shown that superior configurations do exist and they have selected a cambered configuration for operation in cavitating or ventilated flow which has a two-dimensional lift-drag ratio at its design angle of attack and zero cavitation number that is about six times that of a flat plate. If such a cambered foil can be induced to ventilate at very low speeds while the aircraft hull still supports most of the load, a stable and efficient take-off may be possible. This new philosophy is to design for operation with a cavity; whereas in the past the philosophy has been to try to avoid cavitation and ventilation.

The present paper is concerned with some theoretical and experimental work on supercavitating hydrofoils which has been carried out during the last few years by the Langley Research Center. Some of the theoretical work concerns the development of supercavitating sections which produce higher lift-drag ratios than the Tulin-Burkart section of reference 1. However, the principal purpose of the investigation has been to determine the characteristics of practical supercavitating hydrofoils; thus, the effects of aspect ratio, depth of submersion, and hydrofoil thickness are subjects of particular interest. The theoretical discussion makes frequent use of the linearized theory for cavitating flows developed in reference 1 and extends this theory to include the problem of hydrofoils which operate in a ventilated condition near the free surface. Conventional aeronautical corrections for finite span are employed. The theoretical results obtained are compared with a variety of experimental data obtained in the towing tanks of the Langley Research Center.

SYMBOLS

A	aspect ratio
A_n, A_0	coefficients of sine-series expansion of vorticity distribution on equiv-

alent airfoil section; that is,

$$\Omega(x) = 2V \left(A_0 \cot \frac{\theta}{2} + A_1 \sin \theta + A_2 \sin 2\theta \dots A_n \sin n\theta \right)$$

where

$$A_n = \frac{2}{\pi} \int_0^\pi \frac{d\bar{y}}{d\bar{x}} \cos n\theta d\theta$$

$$A_0 = -\frac{1}{\pi} \int_0^\pi \frac{d\bar{y}}{d\bar{x}} d\theta + \alpha = \alpha + A_0'$$

$$A_0' = A_0 - \alpha$$

$$A_{n,h}, A_{0,h}$$

coefficients of sine-series expansion of vorticity distribution on hydrofoil section

a

distance in chords from equivalent airfoil leading edge to center of pressure

$$B_n, B_0$$

coefficients of cosine-series expansion defining location of image vortex in airfoil plane using $Z = -\sqrt{Z}$ transformation

b

parameter defining location of spray at infinity in t -plane (see ref. 2)

$$C_D$$

total drag coefficient, $\frac{D}{qS}$

$$C_f$$

skin-friction drag coefficient, $\frac{D_f}{qS}$

$$C_L$$

total lift coefficient, $\frac{L}{qS}$

$$\bar{C}_L$$

total lift coefficient of equivalent airfoil section, $\frac{\bar{L}}{qS}$

$$C_{L,1}$$

lift coefficient exclusive of cross-flow, $\frac{L_1}{qS}$

$$C_{L,c}$$

crossflow lift coefficient, $\frac{L_c}{qS}$

$$C_{L,d}$$

two-dimensional lift coefficient at infinite depth for $\alpha=0$

$$C_m$$

pitching-moment coefficient (about leading edge), $\frac{M}{qSc}$

$$C_{m,1}$$

pitching-moment coefficient (about leading edge), excluding crossflow

$$\bar{C}_m$$

pitching-moment coefficient of equivalent airfoil section (about leading edge), $\frac{\bar{M}}{qSc}$

$\bar{C}_{m,3}$	third-moment coefficient of equivalent airfoil section (see ref. 1), $\frac{\bar{M}_3}{qSc^4}$	R	cavity-ordinate—aspect-ratio correction factor
C_N	resultant-force coefficient on arbitrary section, $\frac{F}{qS}$	S	area, sq ft
$C_{N,f}$	resultant-force coefficient of flat plate, $\frac{F_f}{qS}$	s	span, ft
C_n, C_0	coefficients of sine-series expansion of vorticity distribution on equivalent airfoil section at arbitrary depth using $Z = -\sqrt{Z}$ transformation	t	arbitrary parameter (see eqs. (114) and (115)); also thickness, ft
C_p	pressure coefficient, $\frac{p-p_\infty}{q}$	u	perturbation velocity in X -direction, fps
c	chord, ft	V	speed of advance, fps
D	total drag force, lb	v	perturbation velocity in Y -direction, fps
D_f	drag force due to skin friction, lb	\bar{v}_i	velocity induced by image vortex, fps
d	leading-edge depth of submersion, ft unless otherwise specified	X, Y	coordinate axes
E	Jones' edge correction, ratio of hydrofoil semiperimeter to span	Z	complex plane, $x+iy$
F	resultant force, lb	x	distance from leading edge along X -axis, ft
F_f	resultant force on flat plate, lb	x_{cp}	distance from leading edge to center of pressure of hydrofoil, ft
f	distance from hydrofoil leading edge to stagnation point in chords	$x_{cp,c}$	distance from leading edge to center of pressure of hydrofoil due to crossflow, ft
g	acceleration due to gravity, ft/sec ²	$x_{cp,1}$	distance from leading edge to center of pressure of hydrofoil excluding crossflow, ft
h	arbitrary parameter	y	distance along Y -axis, ft
L	total lift force, lb	α	geometric angle of attack, radians unless otherwise specified
L_1	lift force exclusive of crossflow, $L-L_c$, lb	α_c	angle-of-attack increase due to camber, radians unless otherwise specified
L_c	lift force due to crossflow, lb	α_i	induced angle of attack, radians unless otherwise specified
l	perpendicular distance from hydrofoil reference line to upper cavity streamline, ft	α_o	angle between hydrofoil chord line and reference line, positive when measured clockwise from the reference line, radians unless otherwise specified
M	moment about leading edge, ft-lb	α'	angle of attack measured from hydrofoil chord line, $\alpha' = \alpha + \alpha_o$, radians unless otherwise specified
\bar{M}_3	third moment about leading edge, $2 \int_0^{\bar{c}} p(\bar{x}) \bar{x}^3 d\bar{x}$, ft ³ -lb	Γ	circulation strength of single vortex, ft ² /sec
m	ratio of lift coefficient to angle of attack, C_L/α	Γ_c	circulation strength of single vortex due to camber, ft ² /sec
n, k	integers	Γ_i	circulation strength of single image vortex, ft ² /sec
p	pressure, lb/sq ft	γ	central angle subtending chord of circular-arc hydrofoil, radians
p_c	pressure within cavity, lb/sq ft	δ	spray thickness at infinite distance downstream, ft
p_o	pressure at mean depth of hydrofoil, lb/sq ft		
p_v	fluid vapor pressure, lb/sq ft		
q	free-stream dynamic pressure, $\frac{1}{2} \rho V^2$, lb/sq ft		

ϵ	deviation of resultant-force vector from normal to hydrofoil reference line, radians
ζ	complex airfoil plane, η, ξ plane
η	ordinate in the ζ plane
θ	parameter defining distance along airfoil chord, $\bar{x} = \frac{c}{2} (1 - \cos \theta)$
ρ	mass density, $\frac{\text{lb-sec}^2}{\text{ft}^4}$
ξ	abscissa in the ζ plane
σ	cavitation number, $\frac{p_o - p_c}{q}$
σ_i	cavitation number at inception
τ	correction factor for variation from elliptical plan form
ϕ	angle between spray and horizontal, radians unless otherwise specified
ψ	angle between \bar{X} -axis and line joining image vortex with a point on equivalent airfoil, radians unless otherwise specified
Ω	vorticity, ft^2/sec
()	indicates "function of," for example, $C_N(\alpha) = C_{N,r}(\alpha + \alpha_c)$
$\beta = \tan^{-1} \frac{C_D}{C_L} = \alpha + \epsilon$	radians unless otherwise specified
Subscripts:	
e	effective
0	zero depth of submersion
t	total
∞	infinite depth of submersion
cp	center of pressure
A_0	due to A_0

Barred symbols refer to equivalent airfoil section and unbarred symbols refer to the supercavitating hydrofoil section.

DESCRIPTION OF SUPERCAVITATING FLOW

The dimensionless number defining cavity flow is $\sigma = \frac{p_o - p_c}{q}$ where p_o is the pressure at the mean depth; p_c , the pressure within the cavity; and q , the dynamic pressure. The magnitude of σ for the condition at which cavitation is incipient is denoted by the particular value σ_i . If σ is reduced to values less than σ_i , cavitation becomes more severe; that is, the cavitation zone extends over

a larger area. When a hydrofoil operates at sufficiently low values of σ , the cavity formed may completely enclose the upper or suction surface and extend several chords downstream as shown in figure 1(a). The reentrant flow formed at the rear of the cavity is caused by the necessity for constant pressure along the cavity streamline. When the cavity is sufficiently long so that the reentrant flow is dissipated without impinging on the body creating the cavity (as shown in fig. 1(a)), the flow is defined as supercavitating. Theoretically, if the cavitation number is reduced to zero, the cavity formed will extend to infinity.

Low values of cavitation number, and thus supercavitating flow, may be obtained by either increasing the velocity or cavity pressure or both. At a constant depth and water temperature, σ for normal vapor-filled cavities is dependent only on the velocity since $p_o - p_c$ is then $p_o - p_v$ and is constant.

If part or all the boundary layer of a configuration is separated, the eddying fluid in the separated region can be replaced by a continuous flow of a lighter fluid such as air. (See refs. 3 and 4.) Regulation of the amount of air supplied will control the cavity pressure and thus the length of the cavity formed. If the quantity of air supplied is very large, the cavity pressure will approach the ambient pressure p_o and a very long cavity will result even at low stream velocities.

The ventilation of a surface-piercing hydrofoil therefore results in a supercavitating flow because of large quantities of air being supplied from the atmosphere to separated flow on the suction surface of the hydrofoil. Supercavitating flow as a result of ventilation also occurs when a nonsurface-piercing hydrofoil of moderate aspect ratio operates near the free surface. (See fig. 1(b).) As pointed out in reference 5, air is entrained in the trailing vortices and is drawn to the suction side of the hydrofoil so that a long trailing cavity completely encloses the hydrofoil upper surface and extends far downstream. The ventilated type of cavity described in reference 5 differs in shape from those formed in deeply submerged flow because of the proximity of the free surface. Ventilated flow near the free surface is similar to planing, the spray forming the upper surface of the cavity. Since the cavity pressure is approximately the same as the ambient pressure

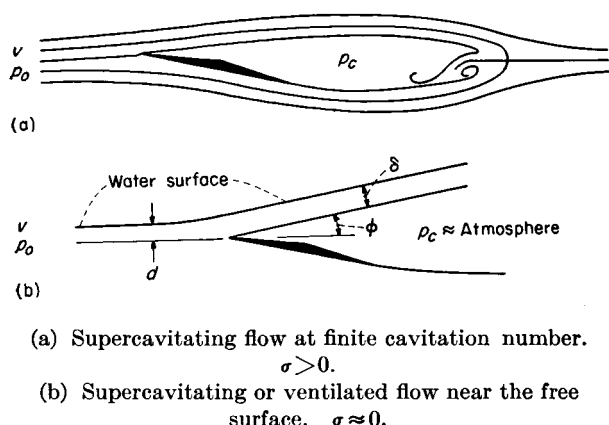


FIGURE 1.—Definition sketch.

(at small depths of submersion), the cavitation number for this type of flow is nearly zero. The present paper is principally concerned with the theoretical predictions of the characteristics of practical hydrofoils operating in the ventilated or zero-cavitation-number flow condition.

THEORETICAL INVESTIGATION

FORCES AND MOMENTS

TWO-DIMENSIONAL THEORY

Flat plate; infinite depth.—The characteristics of a two-dimensional inclined flat plate in an infinite fluid, operating at zero cavitation number, have been obtained by Kirchhoff and Rayleigh. (See ref. 6). The resultant force on the plate is given by the well-known equation

$$C_{N,f} = \frac{2\pi \sin \alpha}{4 + \pi \sin \alpha} \quad (1)$$

Flat plate; finite depth.—Similar work was performed by A. E. Green (refs. 2 and 7) which included the effect of the free surface but neglected gravity. The solution is necessarily obtained in terms of the spray thickness δ rather than the more useful depth of submersion and is given as two parametric equations in terms of the parameter b

$$C_L = C_{N,f} \cos \alpha = \frac{2(b - \sqrt{b^2 - 1}) \sin \alpha \cos \alpha}{K} = m\alpha \quad (2a)$$

$$\frac{\delta}{c} = \frac{b - \cos \alpha}{K} \quad (2b)$$

where

$$K = (b - \sqrt{b^2 - 1}) \sin \alpha + \frac{1}{\pi} \left[2 \cos \alpha + (b \cos \alpha - 1) \log_e \frac{b-1}{b+1} \right]$$

This result is plotted as the variation of C_L/α or m with δ/c for various angles of attack in figure 2.

Although gravity is neglected in Green's solution, the forces on the plate can still be obtained in terms of δ/c from equation (2) if the Froude number V^2/gc is large. On the other hand, the relationship between the spray thickness and the actual leading-edge depth of submersion cannot be determined from Green's two-dimensional analysis. However, in the practical case, at small angles of attack the depth of submersion and spray thickness may be taken as identical even at relatively shallow depths. From figure 2 it may be seen that, for depths greater than about 1 chord, the depth and spray thickness may be considerably different without affecting the value of m . Thus, at depths greater than about 1 chord, the assumption that $d/c = \delta/c$ is adequate to determine the forces. However, at large angles of attack and shallow depths, a better relationship is needed between d/c and δ/c if adequate accuracy is to be maintained. No theoretical solution for the relationship has been obtained. However, in order to give an idea of the relationship between these variables, experimentally obtained lines of constant d/c for an aspect-ratio-1 flat plate are shown in figure 2. Experience has shown that these lines are sufficiently accurate for determining the value of m for moderate aspect ratios. The lines of constant d/c were faired to a value of $\alpha = 90^\circ$ obtained from the equation

$$\frac{\delta}{c} = \frac{d}{c} + \frac{f}{c} \quad (3)$$

where f/c is the dimensionless distance from the leading edge to the stagnation point for the condition of $\alpha = 90^\circ$. The distance f/c can be obtained from Green's work and is for $\alpha = 90^\circ$

$$\frac{f}{c} = \frac{1 + \frac{\pi b}{2} + \log_e \frac{b}{b-1} - \sqrt{b^2 - 1} \left(\frac{\pi}{2} - \sin^{-1} \frac{1}{b} \right)}{\pi(b - \sqrt{b^2 - 1}) + \log_e \frac{b+1}{b-1}} \quad (4)$$

where b has been previously defined for equation

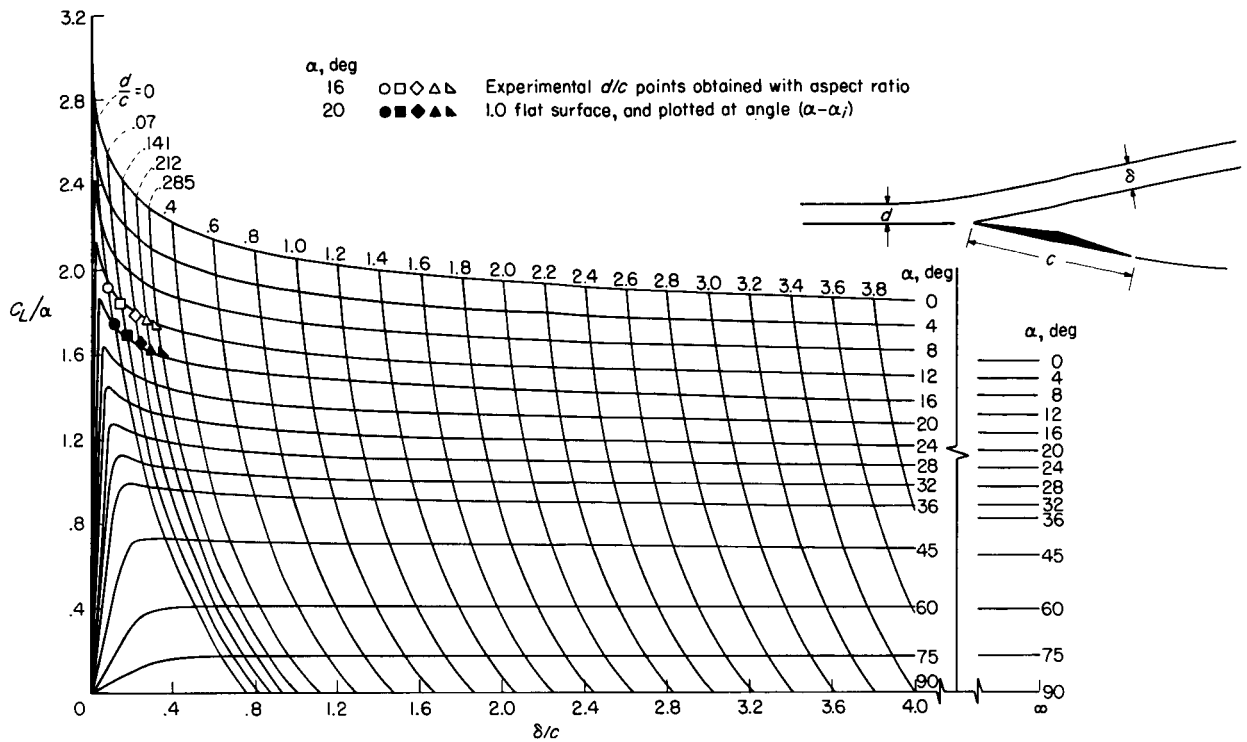


FIGURE 2.—Green's solution for the lift-curve slope of a two-dimensional flat plate (with approximate lines of constant $\frac{d}{c}$).

(2). Equation (3) is based on the assumption that the stagnation streamline for the condition $\alpha = 90^\circ$ is parallel to the undisturbed water surface.

Linearized solution for cambered sections at infinite depth.—The case of cambered surfaces at infinite depth can theoretically be analyzed in two dimensions by the method of Levi-Civita (ref. 7). However, like many conformal mapping problems the method is very difficult to apply to a particular configuration and only a few specific solutions have been obtained. Among these is the work of Rosenhead (ref. 8) and that of Wu (ref. 9). Although the solution of Wu is applicable in principle to arbitrary sections, it has been carried out only for the circular arc. A particular advantage of Wu's solution is that it includes the effects of nonzero cavitation number.

The most useful treatment of cambered surfaces is the linearized theory of Tulin and Burkart (ref. 1) which is readily applicable to any surface configuration (with positive lower surface pressures) as long as the angle of attack and camber are small. The principal results of this linearized theory are summarized as follows:

The supercavitating hydrofoil problem in the Z -plane is transformed into an airfoil problem in the \bar{Z} -plane by the relationship $Z = -\sqrt{\bar{Z}}$. If properties of the equivalent airfoil are denoted with barred symbols and those of the hydrofoil, with unbarred symbols, the following relationships are derived:

$$\frac{d\bar{y}}{d\bar{x}}(\bar{x}) = \frac{dy}{dx}(x^2) \quad (5)$$

$$\bar{u}(\bar{x}) = u(x^2) \quad (6)$$

$$C_L = \bar{C}_m = \frac{\pi}{2} \left(A_0 + A_1 - \frac{A_2}{2} \right) \quad (7)$$

$$C_D = \frac{1}{8\pi} \bar{C}_L^2 = \frac{\pi}{2} \left(A_0 + \frac{A_1}{2} \right)^2 \quad (8)$$

$$C_m = \bar{C}_{m,3} = \frac{\pi}{32} \left(5A_0 + 7A_1 - 7A_2 + 3A_3 - \frac{A_4}{2} \right) \quad (9)$$

The coefficients A_n are the thin-airfoil coefficients in the sine-series expansion of the airfoil vorticity

distribution

$$\Omega(x) = 2V \left(A_0 \cot \frac{\theta}{2} + \sum_{n=1}^{\infty} A_n \sin n\theta \right) \quad (10a)$$

where

$$\bar{x} = \frac{1}{2} \bar{c} (1 - \cos \theta) \quad (0 \leq \theta \leq \pi) \quad (10b)$$

The A coefficients can be found for a given configuration from the following equations:

$$A_0 = -\frac{1}{\pi} \int_0^\pi \frac{d\bar{y}}{d\bar{x}} d\theta + \alpha$$

$$= A_0' + \alpha \quad (11a)$$

$$A_n = \frac{2}{\pi} \int_0^\pi \frac{d\bar{y}}{d\bar{x}} \cos n\theta d\theta \quad (11b)$$

The first term in equation (10a), that is, the A_0 term, represents the vorticity due to incidence with the stream and the second term represents that due to camber. The coefficient A_0 may be separated into two parts A_0' and α as shown in equation (11a). The term A_0' is the value of the integral expression involving the local slope of the hydrofoil when its reference axis is at an angle of attack of 0° . The usual reference axis of an airfoil section is the chord line or line joining the leading edge and trailing edge; however, any line passing through the leading edge may be used as the reference axis. A more convenient reference axis (for the purpose of this report) is the line which makes the integral expression A_0' in equation (11a) zero. When this particular axis is used, the total coefficient A_0 is then simply the angle of attack α , and when α is zero, A_0 is zero and all the lift is produced by the camber.

When A_0 is set equal to zero, the hydrofoil lift-drag ratio for a given lift coefficient is obtained from equations (7) and (8) as follows:

$$\frac{C_L}{C_D} = \frac{\left(A_1 - \frac{A_2}{2} \right)^2}{\frac{A_1^2}{4}} \frac{\pi}{2C_L}$$

$$= 4 \left(1 - \frac{1}{2} \frac{A_2}{A_1} \right)^2 \frac{\pi}{2C_L} \quad (12)$$

Obviously, for maximum lift-drag ratio, $-A_2/A_1$ must be as large as possible. However, if the

assumed condition that a cavity exists only on the upper surface is to be real, the vorticity distribution given by equation (10) must be positive in the interval $0 \leq \theta \leq \pi$, that is, the pressure on the hydrofoil lower surface must be positive over the entire chord; otherwise, a cavity will exist on the lower surface. Thus, for maximum hydrofoil lift-drag ratio, $-A_2/A_1$ must be as large as possible and still satisfy the condition that

$$\Omega(\bar{x}) = 2V \sum_{n=1}^{\infty} A_n \sin n\theta \geq 0 \quad (0 \leq \theta \leq \pi) \quad (13)$$

Tulin-Burkart section: With the stipulation that the vorticity distribution is defined by only two terms in equation (13), reference 1 finds the optimum relationship between A_1 and A_2 as

$$-\frac{A_2}{A_1} = \frac{1}{2}. \quad \text{This relationship results in a hydrofoil}$$

configuration given by the equation

$$\frac{y}{c} = \frac{A_1}{2} \left[\frac{x}{c} + \frac{8}{3} \left(\frac{x}{c} \right)^{3/2} - 4 \left(\frac{x}{c} \right)^2 \right] \quad (14)$$

From equation (7) the design lift coefficient (that is, for $\alpha=0$) for this section is

$$C_{L,d} = \frac{5\pi A_1}{8} \quad (15)$$

and the lift-drag ratio for this condition as obtained from equation (12) is

$$\frac{L}{D} = \frac{25}{4} \frac{\pi}{2C_L} \quad (16)$$

Since $\pi/2C_L$ represents the lift-drag ratio of a flat plate, the configuration given by equation (14) has a lift-drag ratio 25/4 times as great as that of the flat plate. When the hydrofoil given in equation (14) is operated at an angle of attack, the lift-drag ratio becomes

$$\frac{L}{D} = \frac{\alpha + \frac{2}{\pi} C_{L,d}}{\left(\alpha + \frac{4}{5\pi} C_{L,d} \right)^2} \quad (17)$$

In reference 1 it is pointed out that shapes superior to the one given by equation (14) are possible. Two such superior shapes are derived in the following sections.

Three-term section: When the vorticity

distribution is defined by three terms, equation (13) becomes

$$\Omega(\bar{x}) = 2V(A_1 \sin \theta + A_2 \sin 2\theta + A_3 \sin 3\theta) \geq 0 \quad (18)$$

The solution of equation (18) is obtained in the following manner. Let

$$a_2 = -\frac{A_2}{A_1} \quad (19)$$

$$a_3 = \frac{A_3}{A_1} \quad (20)$$

Equation (12) shows that maximum lift-drag ratio for a given lift coefficient is obtained by making the ratio $-A_2/A_1$ as large as possible. The problem is now to find a_2 and a_3 so that a_2 is a maximum and

$$\sin \theta - a_2 \sin 2\theta + a_3 \sin 3\theta \geq 0 \quad (0 \leq \theta \leq \pi) \quad (21)$$

Substituting trigonometric identities for the functions of the multiples of θ , equation (21) may be written as

$$1 - 2a_2 \cos \theta + 3a_3 - 4a_3 \sin^2 \theta \geq 0 \quad (22)$$

The minimum of equation (22) occurs when

$$\theta = \cos^{-1} \frac{a_2}{4a_3}$$

Substituting this value of θ into equation (22) gives

$$1 - \frac{2a_2^2}{4a_3} + 3a_3 - 4a_3 \left(1 - \frac{a_2^2}{16a_3^2}\right) \geq 0 \quad (23)$$

or

$$4a_3 - 4a_3^2 - a_2^2 \geq 0 = h \quad (h \geq 0) \quad (24)$$

Therefore,

$$a_2 = \pm \sqrt{4a_3 - 4a_3^2 - h} \quad (25)$$

and the term under the radical has a maximum at

$a_3 = \frac{1}{2}$. Thus,

$$a_2 = \pm \sqrt{1 - h} \quad (26)$$

and the maximum possible value of a_2 is 1 which

occurs when $h=0$ and $a_3 = \frac{1}{2}$. Since these values

are obtained by considering the minimum value of the vorticity or pressure on the airfoil, the

condition $\Omega(\bar{x}) \geq 0$ is satisfied for all values of θ ($0 \leq \theta \leq \pi$). Thus the solution for the vorticity distribution for the three-term section is

$$\Omega(\bar{x}) = 2VA_1 \left(\sin \theta - \sin 2\theta + \frac{1}{2} \sin 3\theta \right) \quad (27)$$

The airfoil slope which has the vorticity distribution given by equation (27) is obtained from reference 10 and is given as follows:

$$\frac{d\bar{y}}{d\bar{x}} = A_1 \left(\cos \theta - \cos 2\theta + \frac{1}{2} \cos 3\theta \right) \quad (28)$$

When trigonometric identities are substituted for the functions of the multiples of θ , equation (28) becomes

$$\frac{d\bar{y}}{d\bar{x}} = A_1 \left(2 \cos^3 \theta - 2 \cos^2 \theta - \frac{1}{2} \cos \theta + 1 \right) \quad (29)$$

and since $\cos \theta = 1 - 2 \frac{\bar{x}}{c}$

$$\begin{aligned} \frac{d\bar{y}}{d\bar{x}}(\bar{x}) = A_1 \left[2 \left(1 - 2 \frac{\bar{x}}{c} \right)^3 \right. \\ \left. - 2 \left(1 - 2 \frac{\bar{x}}{c} \right)^2 - \frac{1}{2} \left(1 - 2 \frac{\bar{x}}{c} \right) + 1 \right] \quad (30) \end{aligned}$$

The slope of the equivalent hydrofoil as obtained in reference 1 is given as follows:

$$\frac{dy}{dx}(x) = \frac{d\bar{y}}{d\bar{x}}(\sqrt{x}) \quad (31)$$

Equation (31) states that the slope of the hydrofoil can be obtained from equation (30) by replacing \bar{x} with \sqrt{x} .

Thus, since $\bar{c} = \sqrt{c}$,

$$\begin{aligned} \frac{dy}{dx} = A_1 \left[2 \left(1 - 2 \sqrt{\frac{x}{c}} \right)^3 - 2 \left(1 - 2 \sqrt{\frac{x}{c}} \right)^2 \right. \\ \left. - \frac{1}{2} \left(1 - 2 \sqrt{\frac{x}{c}} \right) + 1 \right] \quad (32) \end{aligned}$$

Integrating from 0 to x and dividing both sides by c gives the desired nondimensional hydrofoil shape; that is,

$$\frac{y}{c} = \frac{A_1}{10} \left[5 \left(\frac{x}{c} \right) - 20 \left(\frac{x}{c} \right)^{3/2} + 80 \left(\frac{x}{c} \right)^2 - 64 \left(\frac{x}{c} \right)^{5/2} \right] \quad (33)$$

By using equation (7), the lift coefficient of this

hydrofoil becomes

$$C_L = \frac{\pi}{2} \left(\alpha + \frac{3A_1}{2} \right) \quad (34)$$

or for $\alpha=0$, the design lift coefficient is

$$C_{L,d} = \frac{3\pi A_1}{4} \quad (35)$$

The following drag coefficient may be obtained by using equation (8):

$$\begin{aligned} C_D &= \frac{\pi}{2} \left(\alpha + \frac{A_1}{2} \right)^2 \\ &= \frac{\pi}{2} \left(\alpha + \frac{2C_{L,d}}{3\pi} \right)^2 \end{aligned} \quad (36)$$

For $\alpha=0$, the lift-drag ratio is

$$\frac{L}{D} = 9 \frac{\pi}{2C_L} \quad (37)$$

This value is nine times as large as that for a flat plate and 1.44 times as large as the value for the

hydrofoil of reference 1 where $\frac{L}{D} = \frac{25}{4} \frac{\pi}{2C_L}$. The

following lift-drag ratio may be obtained for finite angles of attack by dividing equation (34) by equation (36)

$$\frac{L}{D} = \frac{\alpha + \frac{2}{\pi} C_{L,d}}{\left(\alpha + \frac{2C_{L,d}}{3\pi} \right)^2} \quad (38)$$

Five-term section: Another hydrofoil section which theoretically has lower drag than either of the previously discussed profiles can be obtained by assigning five terms to equation (13) and finding the coefficients in the resulting equation; that is,

$$\begin{aligned} \Omega(\bar{x}) &= 2V(A_1 \sin \theta + A_2 \sin 2\theta + A_3 \sin 3\theta \\ &\quad + A_4 \sin 4\theta + A_5 \sin 5\theta) \end{aligned} \quad (39)$$

so that $\Omega(\bar{x}) \geq 0$ and $-A_2/A_1$ is a maximum.

First attempts at a solution were made on a Fourier synthesizer. The synthesizer is an electronic device which is capable of generating 80 harmonics of a Fourier series and recording the summation of these components over any desired interval. The amplitude and phase angle of each

harmonic generator is controllable. By using only the first five components and zero phase angle, it was discovered that a solution with $-A_2/A_1$ roughly equal to 1.6 was apparently possible. Unfortunately, the sensitivity of the equipment was not sufficient to assure positive values of the summation of components near the leading edge. However, the synthesizer result was encouraging, since it showed that there was a considerable advantage to using five terms, and revealed some of the characteristics of the solution; for example, the algebraic sign and relative magnitude of each term. The most helpful method for obtaining the best results was that used in obtaining the three-term solution. This was to find first the minimums of equation (39) in terms of the coefficients. The term $-A_2/A_1$ was then assigned a value and the other coefficients were determined analytically so that three of these control points (possible minimums) were zero and the values of the others were examined. By varying the value of $-A_2/A_1$ and the choice of control points, a solution was obtained. The method is one of trial and error and, since the process is somewhat lengthy, the details are omitted. The best solution obtained was

$$\begin{aligned} \Omega(\bar{x}) &= 2VA_1 \left(\sin \theta - \frac{4}{3} \sin 2\theta \right. \\ &\quad \left. + \frac{4}{3} \sin 3\theta - \frac{2}{3} \sin 4\theta + \frac{1}{3} \sin 5\theta \right) \end{aligned} \quad (40)$$

In the course of deriving the solution it was proven that the value of $-A_2/A_1$ must be less than $\sqrt{2}$. Since in the solution given by equation (40) the term $-A_2/A_1$ has a value of $4/3$ (very close to the established maximum), further efforts to find a better solution were not considered to be worthwhile.

By following the method used for the three-term solution, the shape of the hydrofoil corresponding to equation (40) is obtained as follows:

$$\begin{aligned} \frac{y}{c} &= \frac{A_1}{315} \left[210 \left(\frac{x}{c} \right) - 2,240 \left(\frac{x}{c} \right)^{3/2} + 12,600 \left(\frac{x}{c} \right)^2 \right. \\ &\quad \left. - 30,912 \left(\frac{x}{c} \right)^{5/2} + 35,840 \left(\frac{x}{c} \right)^3 - 15,360 \left(\frac{x}{c} \right)^{7/2} \right] \end{aligned} \quad (41)$$

If equation (7) is used, the lift coefficient of

this hydrofoil may be given as

$$C_L = \frac{\pi}{2} \left(\alpha + \frac{5A_1}{3} \right) \quad (42)$$

or for $\alpha=0$ the design lift coefficient is

$$C_{L,d} = \frac{5\pi A_1}{6} \quad (43)$$

The following drag coefficient is obtained by using equation (8):

$$C_D = \frac{\pi}{2} \left(\alpha + \frac{A_1}{2} \right)^2 = \frac{\pi}{2} \left(\alpha + \frac{3C_{L,d}}{5} \right)^2 \quad (44)$$

and for $\alpha=0$ the lift-drag ratio is

$$\frac{L}{D} = \frac{100}{9} \frac{\pi}{2C_{L,d}} \quad (45)$$

This lift-drag ratio is about 11 times as large as the value for a flat plate and nearly twice as efficient as the configuration of reference 1.

For finite angles of attack, the lift-drag ratio is given by the following equation:

$$\frac{L}{D} = \frac{\alpha + \frac{2}{\pi} C_{L,d}}{\left(\alpha + \frac{3}{5\pi} C_{L,d} \right)^2} \quad (46)$$

Circular-arc section: Because of the geometrical simplicity of the circular-arc profile, it is desirable to include its characteristics so that the circular arc may be compared with the other low drag sections. If the central angle subtending the chord is denoted as γ and the chord line is used as the reference axis, the coefficients for the circular arc determined from the linearized theory are:

$$A_0' = -\frac{\gamma}{8} \quad (47a)$$

$$A_1 = \frac{\gamma}{2} \quad (47b)$$

$$A_2 = -\frac{\gamma}{8} \quad (47c)$$

$$A_n = 0 \quad (n > 2) \quad (47d)$$

For the reference axis used, A_0' is negative; therefore, positive lower surface pressures cannot possibly be realized near the leading edge unless

the angle of attack is increased at least to the point where $\alpha - \frac{\gamma}{8} = 0$. Because $A_n = 0$ for $n > 2$ and $A_1 \sin \theta + A_2 \sin 2\theta$ is everywhere positive in the interval $0 \leq \theta \leq \pi$, the condition $\alpha - \frac{\gamma}{8} = 0$ is sufficient to specify positive pressures over the entire chord of the hydrofoil. A convenient way of treating the circular-arc section to make it comparable to the other low drag sections is to reorient its reference line an angle $\frac{\gamma}{8}$ above the chord line so that for this orientation $A_0' = 0$ and $\alpha = 0$. When this new reference line is used, the lift coefficient of the circular-arc section is

$$C_L = \frac{\pi}{2} \left(\alpha + \frac{9}{16} \gamma \right) \quad (48)$$

or for $\alpha=0$ the design lift coefficient is

$$C_{L,d} = \frac{9\pi}{32} \gamma \quad (49)$$

The following drag coefficient is obtained by using equations (8) and (47)

$$C_D = \frac{\pi}{2} \left(\alpha + \frac{\gamma}{4} \right)^2 = \frac{\pi}{2} \left(\alpha + \frac{8}{9\pi} C_{L,d} \right)^2 \quad (50)$$

and for $\alpha=0$ the lift-drag ratio is

$$\frac{L}{D} = \frac{81}{16} \frac{\pi}{2C_{L,d}} \quad (51)$$

This lift-drag ratio is about 5 times as large as the value for a flat plate and almost as great as the Tulin-Burkart section. For finite angles of attack

$$\frac{L}{D} = \frac{\alpha + \frac{2}{\pi} C_{L,d}}{\left(\alpha + \frac{8}{9\pi} C_{L,d} \right)^2} \quad (52)$$

Comparison of sections.—The shape of the four sections discussed in the preceding paragraphs are shown for comparison in figure 3. It may be noted that the Tulin-Burkart and circular-arc sections are very similar. Also it should be noted that the location of maximum camber moves progressively rearward with increasing magnitude of the parameter $-A_2/A_1$.

Pressure distribution: From equations (6) and (10) and the linearized Bernoulli equation, it can be shown that the pressure distribution over the

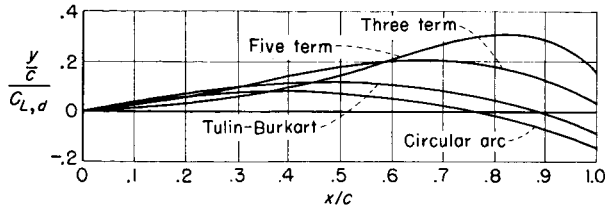


FIGURE 3.—Lower-surface profile of four low-drag supercavitating hydrofoil sections. $\alpha=0^\circ$; infinite depth.

hydrofoil chord is for $A_0'=0$

$$C_p = \frac{p-p_o}{q} = 2 \left(\alpha \cot \frac{\theta}{2} + \sum_{n=1}^k A_n \sin n\theta \right) \quad (53)$$

or, when the two components are separated into the contributions of angle of attack $C_{p,\alpha}$ and camber $C_{p,c}$,

$$\frac{C_{p,\alpha}}{\alpha} = 2 \cot \frac{\theta}{2} \quad (54)$$

and

$$C_{p,c} = 2A_1 \sum_{n=1}^k \frac{A_n}{A_1} \sin n\theta \quad (55)$$

In equations (54) and (55) the location on the hydrofoil corresponding to a given value of θ can be found from the relationship

$$\frac{x}{c} = \frac{1}{4} (1 - \cos \theta)^2$$

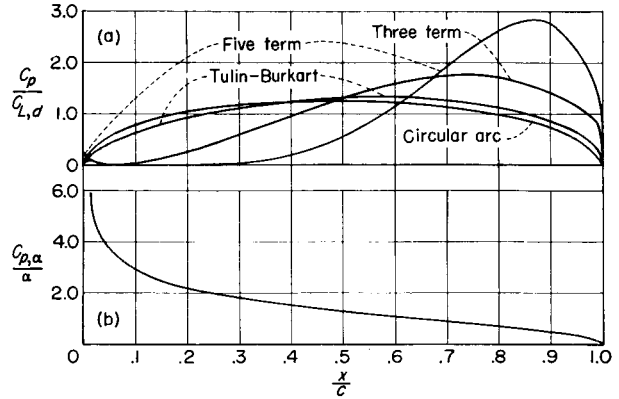
since $\frac{x}{c} = \left(\frac{\bar{x}}{\bar{c}} \right)^2$. For a given hydrofoil A_1 defines a particular value of the hydrofoil lift coefficient at $\alpha=0$; that is, the design lift coefficient $C_{L,d}$ as given by equations (15), (35), (43), and (49). Therefore, with the aid of these equations, equation (55) can also be written in terms of $C_{L,d}$ as

$$\frac{C_{p,c}}{C_{L,d}} = 2 \frac{A_1}{C_{L,d}} \sum_{n=1}^k \frac{A_n}{A_1} \sin n\theta \quad (56)$$

Thus the total-pressure distribution on the hydrofoils can be obtained from

$$C_p = \frac{C_{p,\alpha}}{\alpha} \alpha + \frac{C_{p,c}}{C_{L,d}} C_{L,d} \quad (57)$$

Equations (55) and (57) are plotted in figure 4 for the four hydrofoils under consideration. It is apparent in figure 4(a) that the location of the maximum pressure moves aft with an increase in magnitude of $-A_2/A_1$. It may also be seen that the adverse pressure gradient to the left of the



(a) Contribution due to camber.
(b) Contribution due to angle of attack.

FIGURE 4.—Pressure distribution on four low-drag supercavitating hydrofoils. $\alpha=0^\circ$; infinite depth;

$$(C_p)_{total} = \frac{C_p}{C_{L,d}} C_{L,d} + \frac{C_{p,\alpha}}{\alpha} \alpha$$

pressure maximum also increases as $-A_2/A_1$ increases. Thus, the five-term hydrofoil is more susceptible to boundary-layer separation than the other two hydrofoils. If such separation occurs, the pressure distribution shown will be considerably altered. This condition, of course, also applies to the other three sections but to a lesser degree.

The small pressure "humps" near the leading edge of the three- and five-term hydrofoils are peculiar to the solutions found but could be eliminated by proper adjustment of the coefficients. However, the existence of these "humps" is probably not important in a practical configuration.

Lift-drag ratio: The lift-drag ratios given by equations (17), (38), (46), and (52) are compared in figure 5. The relationship $\frac{L}{D} = \frac{\pi}{2C_L}$ for a flat plate

is also included. The great improvement over the L/D of a flat plate offered by positively cambering the lower surface and operating at the design angle of attack is most encouraging. However, a comparison at what amounts to a fictional design angle of attack is not justified. From a structural standpoint, hydrofoils with the thickness required for strength must be operated at positive angles of attack in order for the cavity to form from the leading edge. Operation at positive angles of attack reduces the lift-drag ratio as shown by the dashed lines in figure 5. Thus the maximum lift-drag ratio for any section depends on the minimum angle at which it can be operated

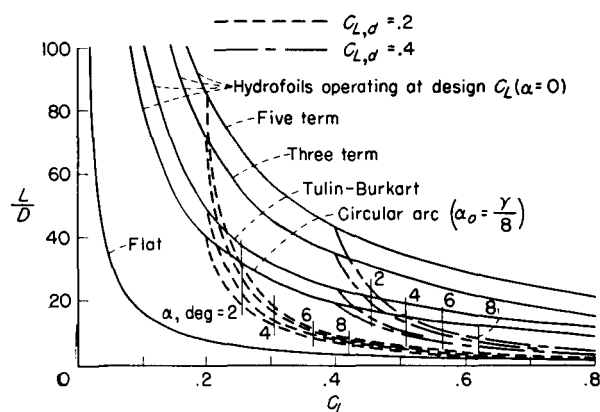


FIGURE 5.—Lift-drag ratios for low-drag hydrofoils calculated from two-dimensional linearized theory.

with a cavity from the leading edge. A meaningful comparison of the hydrofoil sections just discussed is not possible unless the influence of the upper surface of the hydrofoil is also included for it is this surface which controls the maximum lift-drag ratio of the section. If infinite speed and thus zero cavitation number are assumed, it is clear that, if any portion of the upper surface becomes wetted, the lift will decrease and the drag increase. Thus, a knowledge of the profile of the given hydrofoil upper surface combined with the location of the upper cavity streamline at various angles of attack will permit the prediction of the angle of attack at which the maximum lift-drag ratio will occur. Only on the basis of maximum lift-drag ratio can the best supercavitating hydrofoil be selected. A comparison of the various sections based on calculated cavity streamline locations and hydrofoil thickness is presented subsequently.

The practical use of the formulas presented in the preceding discussion is also limited by the assumptions made in their derivation. The restrictions imposed by the assumptions of the linearized theory prevent its use in the calculation of the characteristics of hydrofoils suitable for use as aircraft landing gear. Here, because of the high loads on necessarily thin hydrofoils, the aspect ratio may have to be as low as 1 or 2. Also the hydrofoil must operate near the free water surface and in some instances at large angles of attack. Thus, the effects of these variables on the characteristics of supercavitating hydrofoils (particularly of cambered sections) is needed. Much of this information can be obtained by additional

application of the linearized theory combined with certain modifications to the two-dimensional theory discussed in preceding paragraphs.

MODIFICATIONS OF INFINITE DEPTH THEORY

Nonlinear equation for lift at infinite depth.—

If $\alpha=0$ refers to the reference line which makes $A'_0=0$, then equation (7) may be written as

$$C_L = \frac{\pi}{2} \left(\alpha + A_1 - \frac{A_2}{2} \right) = \frac{\pi}{2} (\alpha + \alpha_c) \quad (58)$$

where α_c is the effective increase in angle of attack due to camber $A_1 - \frac{A_2}{2}$. Thus, the solution for cambered hydrofoils is merely the flat-plate linearized solution $\frac{\pi}{2} \alpha$ with α replaced by $\alpha + \alpha_c$.

This is exactly analogous to the influence of camber on airfoils in an infinite fluid where there is an effective increase in angle of attack due to the camber. By carrying this procedure further and by applying it to the resultant force rather than to the lift, the nonlinear solution of Rayleigh (see eq. (1)) becomes applicable to arbitrary configurations simply by replacing α by $\alpha + \alpha_c$; that is,

$$C_N \approx \frac{2\pi \sin(\alpha + \alpha_c)}{4 + \pi \sin(\alpha + \alpha_c)} \quad (59)$$

The lift will then be

$$C_L \approx \frac{2\pi \sin(\alpha + \alpha_c)}{4 + \pi \sin(\alpha + \alpha_c)} \cos \beta \quad (60)$$

In equation (60) $\beta = \alpha + \epsilon$, where ϵ denotes the deviation of the resultant-force vector from the normal to the hydrofoil reference line. For large values of α , ϵ is small compared with α and $\cos \beta \approx \cos \alpha$. When α is very small, ϵ is a maximum and will almost always be less than about 3° for which the cosine is very nearly 1 or $\cos(\alpha + \epsilon) \approx \cos \alpha \approx 1$. Therefore, $\cos \beta$ in equation (60) may be replaced by $\cos \alpha$ with little loss in accuracy and a great gain in simplicity. Equation (60) then becomes

$$C_L \approx \frac{2\pi \sin(\alpha + \alpha_c)}{4 + \pi \sin(\alpha + \alpha_c)} \cos \alpha \quad (61)$$

For a circular-arc hydrofoil of central angle γ , it has been shown in equation (48) that $\alpha_c = \frac{9}{16} \gamma$. It has also been shown that for the circular arc

the reference line must be chosen at an angle $-\gamma/8$ to the chord line so that $A'_0=0$. The result obtained by substituting $\alpha_c = \frac{9}{16}\gamma$ into equation (61) is compared in figure 6 with the linear solution of Tulin and Burkart (eq. (58)) and the nonlinear solution of Wu (ref. 9) for two circular-arc profiles. The agreement of equation (61) with the more exact solution of Wu is good over the entire range of angle of attack from 0° to 90° . Similar agreement is expected for any configuration of small camber.

The successful modification of the Rayleigh equation to include cambered configurations leads at once to a similar modification of the solution of Green. (See ref. 2.) However, in this case the argument for replacing α by $\alpha + \alpha_c$ is very weak unless the section coefficients which determine α_c are known as the depth varies from infinity to zero.

Linearized solution for lift of cambered sections at finite depth.—An examination of the linearized expressions for the lift coefficient of arbitrary hydrofoils at infinite depth and at zero depth reveals that both the lift-curve slope and the increase in angle of attack due to camber change with depth of submersion. At infinite depth the linearized expression for lift coefficient is given by equation (58). At zero depth the lift coefficient must be one-half of the fully wetted value obtained from thin-airfoil theory as pointed out in reference 11;

that is,

$$C_{L,0} = \pi \left(A_{0,h} + \frac{A_{1,h}}{2} \right) \quad (62)$$

where $A_{0,h}$ and $A_{1,h}$ are the thin-airfoil coefficients of the section in the hydrofoil plane and are given by the expressions

$$A_{0,h} = -\frac{1}{\pi} \int_0^\pi \frac{dy}{dx} d\theta \quad (63a)$$

$$A_{1,h} = \frac{2}{\pi} \int_0^\pi \frac{dy}{dx} \cos \theta d\theta \quad (63b)$$

For the Tulin-Burkart section at an angle of attack of 0° , these values may be determined as

$$A_{0,h} = 0.227 A_1 \quad (64a)$$

$$A_{1,h} = 1.151 A_1 \quad (64b)$$

Thus, from equations (58) and (62) it is seen that, for a flat plate at small angles, the lift coefficient goes from $\frac{\pi}{2}\alpha$ at infinite depth to $\pi\alpha$ at zero depth (as given by Green, ref. 2) whereas, for the Tulin-Burkart section (ref. 1) at an angle of attack of 0° these values are $\frac{\pi}{2}(1.25A_1)$ at infinite depth and $\pi(0.802A_1)$ at zero depth. Although the flat-plate lift coefficient doubles in going from infinite to zero depth, the ratio is only 1.28 for the cambered section. The important point to note is that the value of α_c for the Tulin-Burkart section changes from $1.25A_1$ to $0.802A_1$ as the depth changes from infinity to zero.

It is now desirable to determine α_c for finite depths of submersion. This value may be obtained by modifying the linearized theory of reference 1 to include the effects of the free water surface.

Exact linearized solution: The effect of the free water surface may be obtained by finding the transformation which will map the free water surface, the hydrofoil, and the cavity streamlines into the real axis of an auxiliary or equivalent airfoil plane denoted as ζ to distinguish it from the Z -plane used at infinite depth. The transformation required is

$$Z = \frac{d}{\pi} (\zeta - 1 - \log_e \zeta) \quad (65)$$

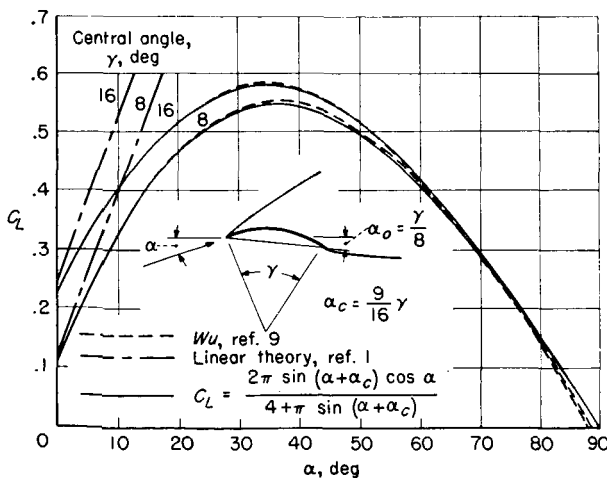


FIGURE 6.—Two-dimensional theories for the lift coefficient of a circular-arc hydrofoil at infinite depth.

where d is the depth of submersion of the leading edge, or more exactly the spray thickness δ . The Z -plane and its transformation in the ζ -plane are shown in figure 7. In the linearized theory developed in reference 1 points of corresponding perturbation velocities u and v remain constant in the transformation; therefore, the boundary conditions shown in the Z -plane are shown in the ζ -plane in their corresponding locations. The potential-flow problem shown in the ζ -plane is exactly the thin-airfoil problem. It is well-known that the thin-airfoil problem can be solved by distributing vortices along the chord so that the condition $\bar{v} = \frac{d\bar{y}}{d\bar{x}} V$ is satisfied. (See ref. 10.) The desired distribution of vorticity is $\Omega(\bar{x})$ as given in equation (10a). With $\Omega(\bar{x})$ known, $\bar{u}(\bar{x})$ and $\bar{v}(\bar{x})$ are known. These values of \bar{u} and \bar{v} on the airfoil are exactly the same as the values of u and v on the hydrofoil if the relationship between x and \bar{x} satisfies the equation

$$x = \frac{d}{\pi} [\bar{x} - \log_e(1 + \bar{x})] \quad (66)$$

Equation (66) is obtained directly from equation (65) by noting that $\zeta = 1 + \bar{x}$. Dividing equation (66) through by c gives

$$\frac{x}{c} = \frac{1}{\pi} \frac{d}{c} [\bar{x} - \log_e(1 + \bar{x})] \quad (67)$$

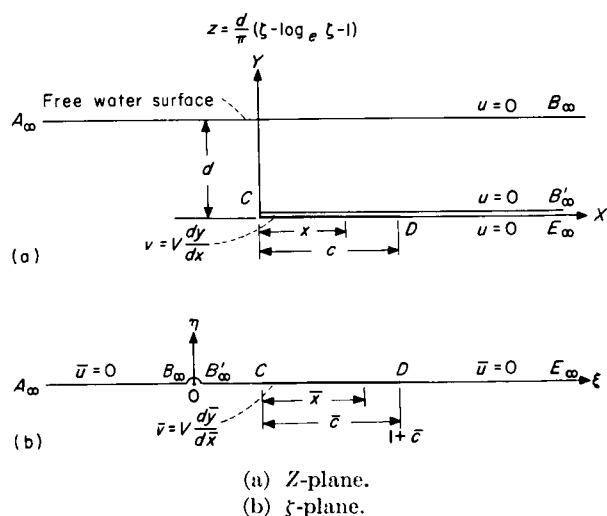


FIGURE 7.—Transformation of hydrofoil at finite depth to equivalent airfoil.

When $\frac{x}{c}=1$, $\bar{x}=\bar{c}$; therefore,

$$\frac{d}{c} = \frac{\pi}{\bar{c} - \log_e(1 + \bar{c})} \quad (68)$$

By using equations (67) and (68) the relationship between $\frac{x}{c}$ and $\frac{\bar{x}}{c}$ may be determined for both positive and negative values of $\frac{\bar{x}}{c}$. It can be seen in figure 7 that negative values of $\frac{\bar{x}}{c}$ correspond to points in front of the airfoil which in turn are related to points on the upper-cavity streamline.

The relationship between $\frac{\bar{x}}{c}$ and $\frac{x}{c}$ is presented in figure 8. With the aid of figure 8 and a knowledge of thin airfoil theory, the solution to the supercavitating hydrofoil problem at finite depth is "easily" determined. The word "easily" refers to the comprehension of the solution; the actual labor is considerably involved because of the necessity to resort frequently to numerical integration.

The procedure for determining the pressure distribution and thus the forces and moments on a hydrofoil at arbitrary depth is as follows:

(1) The shape of the hydrofoil is known as $y=y(x)$ and thus

$$\frac{dy}{dx} = \frac{dy}{dx}(x) \text{ or } \frac{dy}{dx}\left(\frac{x}{c}\right)$$

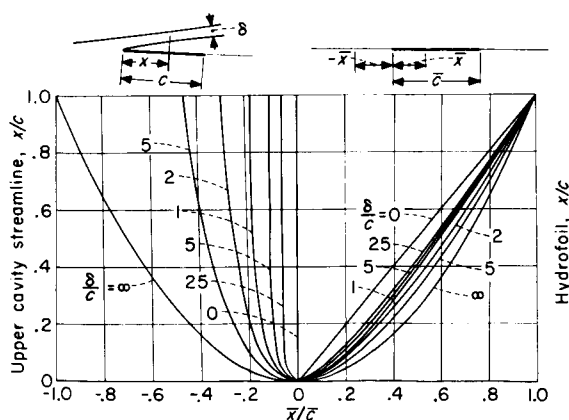


FIGURE 8.—The influence of depth of submersion on the relationship between points in hydrofoil and equivalent airfoil planes.

(2) The slope of the equivalent airfoil at the point $\left(\frac{x}{c}\right)$ is exactly the same as the slope of the hydrofoil $\frac{dy}{dx}\left(\frac{x}{c}\right)$ when $\frac{x}{c}$ and $\frac{\bar{x}}{c}$ are related as shown in figure 8. Thus $\frac{d\bar{y}}{d\bar{x}}\left(\frac{\bar{x}}{c}\right)$ is found.

(3) The vorticity distribution on the airfoil is then obtained from equations (10) and (11).

(4) The perturbation velocity \bar{u} in terms of the vorticity Ω is given by the equation

$$\bar{u}\left(\frac{\bar{x}}{c}\right) = \frac{1}{2}\Omega\left(\frac{\bar{x}}{c}\right) \quad (69)$$

Thus the velocity $\bar{u}\left(\frac{\bar{x}}{c}\right)$ is determined at every point along the airfoil.

(5) The perturbation velocity $u\left(\frac{x}{c}\right)$ on the hydrofoil is exactly the same as the velocity $\bar{u}\left(\frac{\bar{x}}{c}\right)$ if $\frac{\bar{x}}{c}$ and $\frac{x}{c}$ are related as shown in figure 8. Thus, the velocity $u\left(\frac{x}{c}\right)$ is determined.

(6) Step (5) also determines the linearized pressure coefficient since C_p is given by the equation

$$C_p = \frac{p - p_\infty}{q} = 2 \frac{u}{V}$$

or

$$C_p\left(\frac{x}{c}\right) = A_0 \cot \frac{\theta}{2} + \sum A_n \sin n\theta \quad (70)$$

where θ is related to $\frac{x}{c}$ by equation (10b) and figure 8.

(7) With a knowledge of $C_p\left(\frac{x}{c}\right)$ the lift, drag, and moment coefficients are determined as

$$C_L = \int_0^1 C_p\left(\frac{x}{c}\right) d\frac{x}{c} \quad (71a)$$

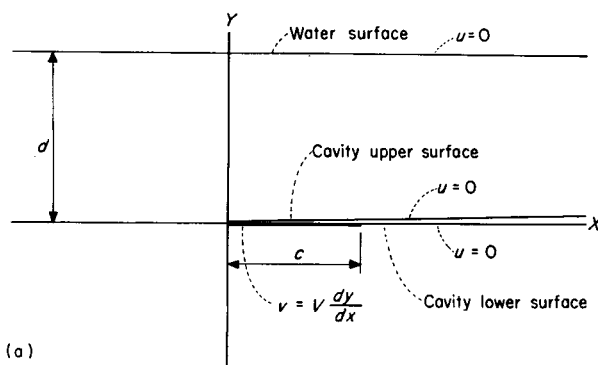
$$C_D = \int_0^1 C_p\left(\frac{x}{c}\right) \frac{dy}{dx} d\frac{x}{c} \quad (71b)$$

$$C_m = \int_0^1 C_p\left(\frac{x}{c}\right) \frac{x}{c} d\frac{x}{c} \quad (71c)$$

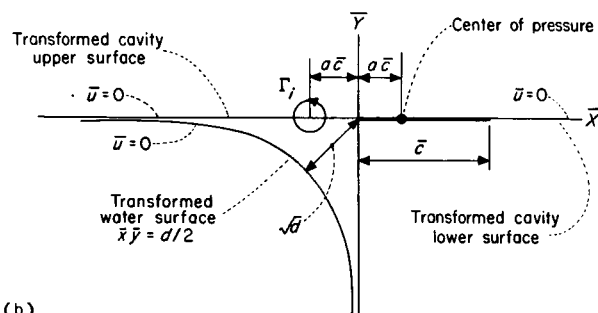
Approximate solution: The calculations by the exact linearized method were rather tedious and

this method of solution was set aside when an approximate method was discovered. The approximate method continues with the simple transformation $\bar{Z} = -\sqrt{Z}$ used in reference 1. The advantage of the simpler transformation is that, if the vorticity distribution in the presence of the water surface can be determined in the \bar{Z} -plane, the simple equations (7) and (9) for the lift and moment coefficient will still be applicable.

In figure 9 it may be seen that $\bar{Z} = -\sqrt{Z}$ transforms the free water surface in the hydrofoil plane, where $u=0$ (see fig. 9(a)), into a hyperbola in the third quadrant of the airfoil plane (fig. 9(b)). The boundary condition that must be satisfied on this hyperbola is that the perturbation velocity \bar{u} be zero because, in complex velocity problems of the type considered here, the lines of constant velocity are transformed and not the lines of constant velocity potential or the stream function.



(a)



(b)

(a) Hydrofoil, Z -plane.
(b) Equivalent airfoil, \bar{Z} -plane.

FIGURE 9.—The linearized boundary conditions in the hydrofoil and equivalent airfoil planes using $\bar{Z} = -\sqrt{Z}$ transformation.

For the particular case of zero depth the hydrofoil problem is transformed by $\bar{Z} = -\sqrt{Z}$ into the fourth quadrant of the airfoil plane. Thus, it may be seen in figure 9(b) that the free water surface adds the condition that $\bar{u}=0$ along the negative \bar{Y} -axis. This additional boundary condition can be satisfied (along with the other infinite-depth boundary conditions) by locating an image of the airfoil-vorticity distribution along the negative \bar{X} -axis. The direction of this vorticity must be opposite to that of the airfoil in order to make $\bar{u}=0$ at all points along the negative \bar{Y} -axis. A simpler and often used approximation is to replace the distributed image vorticity by a single vortex, equal in strength to the airfoil circulation, at a location equal to the distance from the leading edge to the airfoil center of pressure as shown in figure 9(b).

For finite depth of submersion, the condition is that $\bar{u}=0$ must be satisfied at all points on the hyperbola and on the negative \bar{X} -axis. It is not possible to satisfy these conditions with a single vortex as was done for the case of zero depth. However, the influence on the airfoil of the infinite array of vortices needed to satisfy the boundary conditions shown in figure 10 may be approximated by a single vortex of strength Γ in the location shown. The adequacy of the approximation can be determined by calculating the effect of this image vortex on the lift of a flat plate as the depth of submersion is varied and then comparing the result with the exact solution of Green. This depth effect may be determined by concentrating the airfoil circulation at its center of pressure and the image circulation at a point

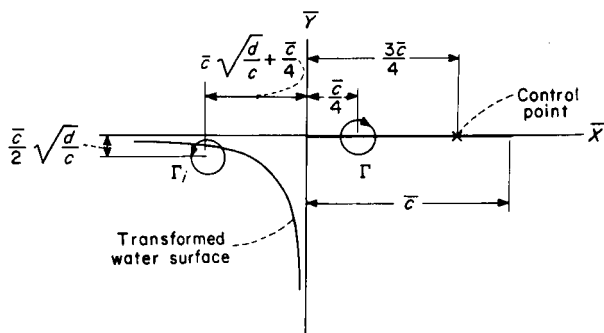


FIGURE 10.—Linearized model in \bar{Z} -plane for calculating the effect of depth of submersion on the lift coefficient of a flat plate. $\sigma=0$.

$\frac{\bar{c}}{4} + \bar{c}\sqrt{\frac{d}{c}}$ forward of the leading edge and $\frac{\bar{c}}{2}\sqrt{\frac{d}{c}}$ below the leading edge (see fig. 10) and computing the total downwash on the flat plate at its $3\bar{c}/4$ point. (See ref. 12.) The method assumes that the center of pressure of the airfoil remains constant at $c/4$ as the depth changes. The resulting downwash angle α at the $3\bar{c}/4$ point is calculated to be

$$\alpha = \frac{\Gamma}{\pi \bar{c} V} \left[1 - \frac{1}{2} \left(\frac{1 + \sqrt{\frac{d}{c}}}{1 + 2\sqrt{\frac{d}{c} + \frac{5d}{4c}}} \right) \right] \quad (72)$$

The ratio of hydrofoil lift at finite depth to the lift at infinite depth is

$$\frac{C_L}{C_{L,\infty}} = \frac{\bar{C}_m}{\bar{C}_{m,\infty}} = \frac{\frac{1}{4}\bar{C}_L}{\frac{1}{4}\bar{C}_{L,\infty}} = \frac{\Gamma}{\Gamma_\infty} \quad (73)$$

Therefore, since $\Gamma_\infty = \pi \bar{c} \alpha V$,

$$\frac{C_L}{C_{L,\infty}} = \frac{\Gamma}{\Gamma_\infty} = \frac{1}{1 - \frac{1}{2} \left(\frac{1 + \sqrt{\frac{d}{c}}}{1 + 2\sqrt{\frac{d}{c} + \frac{5d}{4c}}} \right)} \quad (74)$$

Equation (74) is compared in figure 11 with the exact solution of Green (see fig. 2, $\alpha=0$), and the agreement is excellent.

The adequacy of the method used in determining the influence of free water surface proximity on the lift of a flat plate justifies its use on cambered hydrofoils. However, for cambered hydrofoils the problem is more difficult because

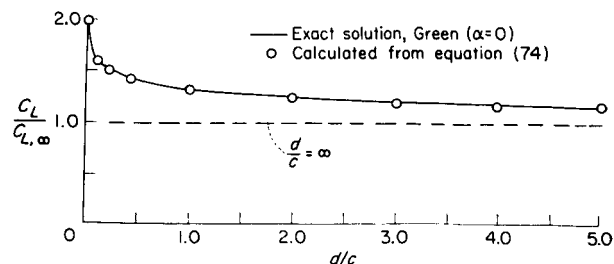


FIGURE 11.—Comparison of linearized solution with exact solution for the effect of depth of submersion on the lift coefficient of a flat plate. $\sigma=0$.

By equating coefficients of like terms, the C coefficients are determined as

$$C_0 = \frac{A_0(4+B_1)+A_1B_0}{4+B_1-2B_0} \quad (86a)$$

$$C_1 = \frac{2A_1(2-B_0)-2A_0B_1}{4+B_1-2B_0} \quad (86b)$$

$$C_n = A_n - \frac{(2A_0+A_1)B_n}{4+B_1-2B_0} \quad (86c)$$

If $A_0 = \alpha$ and $A_n = 0$ where $n \geq 1$, the effect of depth of submersion on the lift coefficient of a flat plate can be computed from the coefficients obtained from equations (86). The values of $\frac{C_L}{C_{L,\infty}}$ computed by this method have been found to be in excellent agreement with the solution of Green for $\alpha = 0$.

For the particular condition of $A_0 = 0$ (the case of hydrofoils such as the Tulin-Burkart section at zero angle of attack) equations (86) become

$$C_0 = \frac{B_0 A_1}{4+B_1-2B_0} \quad (87a)$$

$$C_1 = \frac{2A_1(2-B_0)}{4+B_1-2B_0} \quad (87b)$$

$$C_n = A_n - \frac{B_n A_1}{4+B_1-2B_0} \quad (87c)$$

The coefficients B_0 and B_n as obtained from equation (81) are plotted in figure 13 against the

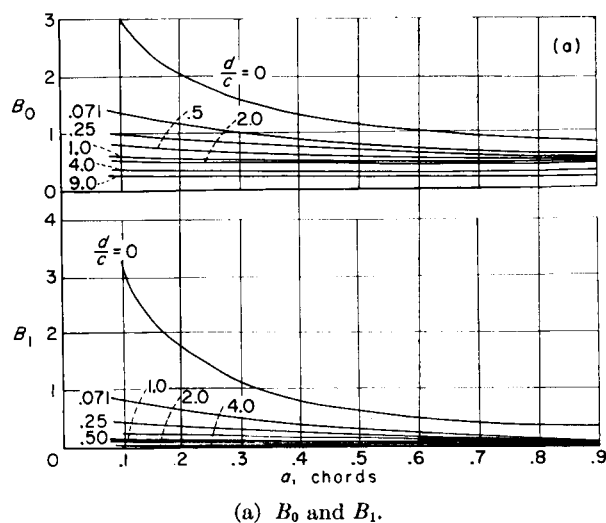
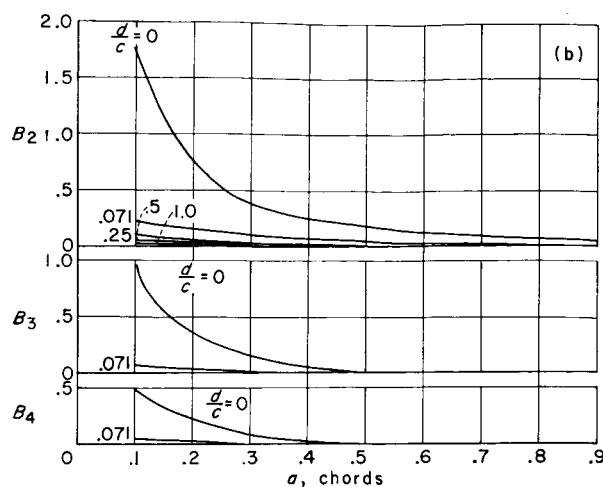


FIGURE 13.—The B coefficients.



(b) B_2 , B_3 , and B_4 .

FIGURE 13.—Concluded.

distance to the center of pressure a for several depths of submersion. For the special condition of zero depth the B coefficients for the Tulin-Burkart section are found to be 1.296, 0.772, and 0.22 for B_0 , B_1 , and B_2 , respectively. In making this computation, the final center-of-pressure location a is used; therefore, a is first given an assumed value, the B and C coefficients determined, then from the resulting C coefficients, a is calculated from equation (80) and the procedure repeated if necessary. For the Tulin-Burkart section a is found to be 0.42 for $d/c = 0$. By using the final B coefficients the C coefficients are determined from equations (87) as $0.595A_1$, $0.646A_1$, and $-0.61A_1$ for C_0 , C_1 , and C_2 , respectively.

The lift coefficient of the Tulin-Burkart section at zero depth may be obtained by substituting the C coefficients obtained in the previous paragraph for the A coefficients in equation (7). The ratio of the lift coefficient at zero depth to the lift at infinite depth is

$$\frac{C_{L,0}}{C_{L,\infty}} = \frac{(0.595 + 0.646 + 0.305)A_1}{\frac{5A_1}{4}} = 1.24 \quad (88)$$

The value 1.24 compares favorably with the more exact value of 1.28 given previously. The results of calculating $\frac{C_L}{C_{L,\infty}}$ for the Tulin-Burkart section along with the other three sections being considered are plotted in figure 14.

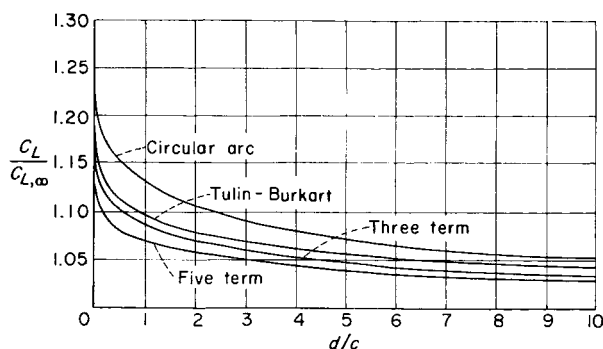


FIGURE 14.—Influence of depth of submersion on the lift coefficient of cambered sections operating at the design angle of attack. $\alpha = 0^\circ$.

The true linearized lift-curve slope m for finite depths of submersion in the equation $C_L = m(\alpha + \alpha_c)$ is that shown in figure 2 for $\alpha = 0$. Therefore, the effective angle of attack due to camber α_c is obtained from the following relationship:

$$\frac{m(\alpha=0)\alpha_c}{\frac{\pi}{2}\alpha_{c,\infty}} = \frac{C_L}{C_{L,\infty}} \text{ or } \frac{\alpha_c}{\alpha_{c,\infty}} = \frac{\pi}{2m(\alpha=0)} \frac{C_L}{C_{L,\infty}} \quad (89)$$

Values of $\frac{\alpha_c}{\alpha_{c,\infty}}$ are plotted against d/c for the Tulin-Burkart section and the other three sections in figure 15.

Equation (89) is obviously limited by the linearizing assumptions made in its derivation. An important limitation is that due to the assumption that the free surface is always horizontal and thus $\delta/c = d/c$. At small depth-chord ratios and particularly for large magnitudes of camber, the free water surface is not horizontal and $\delta/c > d/c$. Thus, for small values of d/c and large magnitudes of camber the values of $\alpha_c/\alpha_{c,\infty}$ given in figure 15

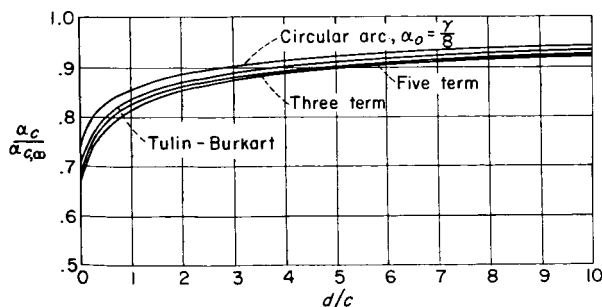


FIGURE 15.—Influence of depth of submersion on the effective angle of attack α_c of cambered sections operating at the design angle of attack. $\alpha = 0^\circ$.

are probably too low.

Nonlinear equation for lift at finite depth.—With a knowledge of the angle of attack due to camber α_c at finite depths of submersion, Green's solution is now modified to include camber by treating the effective angle of attack as $\alpha + \alpha_c$, where α_c is obtained from figure 15. This method is exactly the method used in modifying the Rayleigh equation to obtain the nonlinear approximation for the lift coefficient at infinite depth. With this assumption, the resultant-force coefficient for a cambered hydrofoil at any positive depth of submersion is obtained in terms of the spray thickness δ/c from equations (2) as

$$C_N(\alpha) \approx C_{N,f}(\alpha + \alpha_c) \quad (90)$$

Equation (90) states that the resultant force on a cambered section is approximated by replacing α in Green's solution for a flat plate by the effective angle of attack $\alpha + \alpha_c$. It will be shown that the resultant force will deviate only slightly from the normal (as previously pointed out for the condition of finite depth) and therefore the nonlinear equation for determining the lift coefficient of cambered sections at arbitrary depth is

$$C_L(\alpha) \approx C_{N,f}(\alpha + \alpha_c) \cos \alpha \quad (91)$$

Three-dimensional theory at finite depth.

The preceding two-dimensional theory can now be modified to include the effects of finite span.

Lift: The flow about a supercavitating hydrofoil may be constructed by a suitable combination of sources and vortices. The vortices contribute unsymmetrical velocity components and lift; the sources contribute symmetrical components which provide thickness for the cavity but no lift. Since for a finite span a system of vortices cannot end at the tips of the foil, a system of horseshoe vortices must be combined with the sources to describe the flow. If the assumption is made that the influence of finite span on the two-dimensional lift coefficient is due to the effects of the trailing vorticity, then the resulting effect of aspect ratio is exactly the same as that for a fully wetted airfoil. Jones (ref. 13) gives the lift of a fully wetted elliptical flat plate as

$$\overline{C_L} = \frac{1}{E} 2\pi(\alpha - \alpha_i) \quad (92)$$

where E is the ratio of semiperimeter to the span and α_i is the induced angle of attack caused by the trailing vorticity. Thus the effect of aspect ratio is to decrease the two-dimensional lift-curve slope by a factor $1/E$ and to decrease the effective angle of attack by an increment α_i . Therefore for the finite-aspect-ratio supercavitating hydrofoil at infinite depth, equation (58) is modified to give

$$C_{L,1} = \frac{1}{E} \frac{\pi}{2} (\alpha + \alpha_c - \alpha_i) \quad (93)$$

or more generally for finite depth, equation (91) becomes

$$C_{L,1} \approx \frac{1}{E} C_{N,f} (\alpha + \alpha_c - \alpha_i) \cos \alpha \quad (94)$$

where for rectangular plan form of aspect ratio A , $E = \frac{A+1}{A}$ and

$$\alpha_i = \frac{C_{L,1}}{\pi A} (1 + \tau) \quad (95)$$

where τ is a correction for plan form. (See ref. 10.)

Another effect due to finite aspect ratio is the concept of additional lift due to crossflow. (See refs. 14 and 15.) This crossflow lift is assumed to be due to the drag on the hydrofoil contributed by the component of free-stream velocity normal to the hydrofoil plan form. In the present case of zero cavitation number, the crossflow drag coefficient is the Rayleigh value, 0.88. Since this lift is caused only by the spanwise flow (flow around the ends of the plate), it is also modified to account for the effect of aspect ratio by the Jones' edge correction $1/E$. Since only the spanwise flow is considered, E is now the ratio of the semiperimeter to the chord. Because the flow being considered is normal to the plate, the induced angle for this flow is zero. Thus for a flat plate, the crossflow lift $C_{L,c}$ is

$$C_{L,c} = \frac{1}{A+1} 0.88 \sin^2 \alpha \cos \alpha \quad (96)$$

No experimental or theoretical information on the crossflow lift of cambered surfaces is available in the literature. In order to approximate this component the following assumptions are made:

(1) The crossflow force acts normal to the

hydrofoil chord line.

(2) The effective direction of the free stream on the plate is altered by the increase in angle of attack due to camber α_c .

Thus, the crossflow lift on cambered sections is assumed to be

$$C_{L,c} \approx \frac{1}{A+1} 0.88 \sin^2 (\alpha' + \alpha_c) \cos \alpha' \quad (97)$$

where $\alpha' = \alpha + \alpha_0$, and α_0 is the inclination of the chord line to the reference line of the section (positive when measured clockwise from the reference line) and α_c is obtained from figure 15 for the depth of interest.

The total lift on a finite-aspect-ratio hydrofoil operating near the free water surface is then obtained by adding equation (97) to equation (94) to give

$$C_L(\alpha) \approx \frac{A}{A+1} C_{N,f} (\alpha + \alpha_c - \alpha_i) \cos \alpha + \frac{1}{A+1} 0.88 \sin^2 (\alpha' + \alpha_c) \cos \alpha' \quad (98)$$

In view of the very approximate nature of equation (97) an examination of the effect of this crossflow term on the total-lift coefficient is desirable. For a Tulin-Burkart, aspect-ratio-1 section ($A_1=0.2$) operating at $d/c=0.071$, the ratio of the calculated crossflow lift $C_{L,c}$ to the calculated total lift was 0.157 at $\alpha=4^\circ$ and 0.283 at $\alpha=20^\circ$. For a five-term section with $A_1=0.075$, an aspect ratio of 3, and $d/c=0.071$, the ratio has been calculated as 0.014 at $\alpha=4^\circ$ and 0.072 at $\alpha=20^\circ$. Thus any inaccuracies in the crossflow lift as computed by equation (97) will appreciably affect the total lift coefficient at large angles, small aspect ratios, and large cambers. On the other hand at higher aspect ratios and small cambers, errors in the crossflow component do not greatly influence the total calculated lift.

Equation (98) may be written in terms of the slope m (given in fig. 2) as

$$C_L = \frac{A}{A+1} m (\alpha + \alpha_c - \alpha_i) \frac{\cos \alpha}{\cos (\alpha + \alpha_c - \alpha_i)} + \frac{1}{A+1} 0.88 \sin^2 (\alpha' + \alpha_c) \cos \alpha' \quad (99)$$

where α_c is obtained from figure 14 for the depth-chord ratio of interest and α_i is obtained from

equation (95). The ratio of cosines in the first term is necessary because the vector $m(\alpha + \alpha_e - \alpha_i)$ is directed at an angle $(\alpha + \alpha_e - \alpha_i)$ from the normal instead of the desired α . In equation (95) $C_{L,1}$ is the first term from equation (99). Equation (99) is solved by iteration and the convergence is quite rapid. A sample calculation of the lift coefficient is given in the appendix.

Drag: The drag coefficient of a supercavitating hydrofoil of finite aspect ratio operating at zero cavitation number and finite depth of submersion is

$$C_D = C_{L,1} \tan(\alpha + \epsilon) + C_{L,e} \tan \alpha' + C_f \quad (100)$$

where $C_{L,1}$ is the first term in equation (99) and ϵ is the deviation of the resultant-force vector from the normal. For a flat plate $\epsilon = 0$, $\alpha' = \alpha$, and thus $C_D = C_L \tan \alpha + C_f$. For cambered surfaces similar to the circular-arc or Tulin-Burkart section, the effect of ϵ becomes very small at large angles of attack and may be neglected; however, at small angles of attack, the effect of ϵ on the drag coefficient cannot be neglected. For cambered surfaces similar to the three- and five-term sections, ϵ is found to have appreciable negative values at all except very small angles of attack and thus cannot be neglected. An approximation to the value of ϵ can be made by determining its value from the two-dimensional linearized solution and then modifying the result for the case of finite angles of attack and aspect ratio. Either the rigorous or approximate methods of obtaining the linearized drag coefficient may be used. The approximate solution is obtained in the following manner.

The linearized drag coefficient as given in reference 1 is

$$C_D = - \int_0^{\sqrt{c}} \frac{4\bar{x}\bar{v}\bar{u}}{cV^2} d\bar{x} \quad (101)$$

If \bar{x} is replaced by $\frac{\sqrt{c}}{2}(1 - \cos \theta)$ and $d\bar{x}$ by $\frac{\sqrt{c}}{2} \sin \theta d\theta$, equation (101) becomes

$$C_D = - \int_0^\pi \frac{(1 - \cos \theta) \sin \theta \bar{u}\bar{v}}{V^2} d\theta \quad (102)$$

Now u may be written in terms of the vorticity on the equivalent airfoil operating at finite depth as

$$\bar{u} = \frac{\Omega}{2} = V \left[C_0 \left(\frac{1 + \cos \theta}{\sin \theta} \right) + \sum_{n=1}^{\infty} C_n \sin n\theta \right] \quad (103)$$

and

$$\bar{v} = V \left(-A_0 + \sum_{n=1}^{\infty} A_n \cos n\theta \right) \quad (104)$$

Therefore

$$C_D = - \int_0^\pi (1 - \cos \theta) \sin \theta \left[C_0 \left(\frac{1 + \cos \theta}{\sin \theta} \right) + \sum C_n \sin n\theta \right] \left(-A_0 + \sum A_n \cos n\theta \right) d\theta \quad (105)$$

For the condition where $A_0 = \alpha$, C_D becomes after integrating

$$C_D = \frac{\pi}{2} \alpha \left(C_0 + C_1 - \frac{C_2}{2} \right) + \frac{\pi}{2} \left[\left(\frac{C_1}{4} - \frac{C_2}{2} \right) A_1 + \left(\frac{C_0 + C_1 + \frac{C_4}{2}}{2} \right) A_2 - \frac{A_4 C_2}{4} \right] \quad (106)$$

At infinite depth ($C_0 = A_0$, $C_n = A_n$), equation (106) reduces to the value given by Tulin-Burkart in reference 1

$$C_{D,\infty} = \frac{\pi}{2} \left(A_0 + \frac{A_1}{2} \right)^2 = \frac{1}{8\pi} (\bar{C}_L)^2 \quad (107)$$

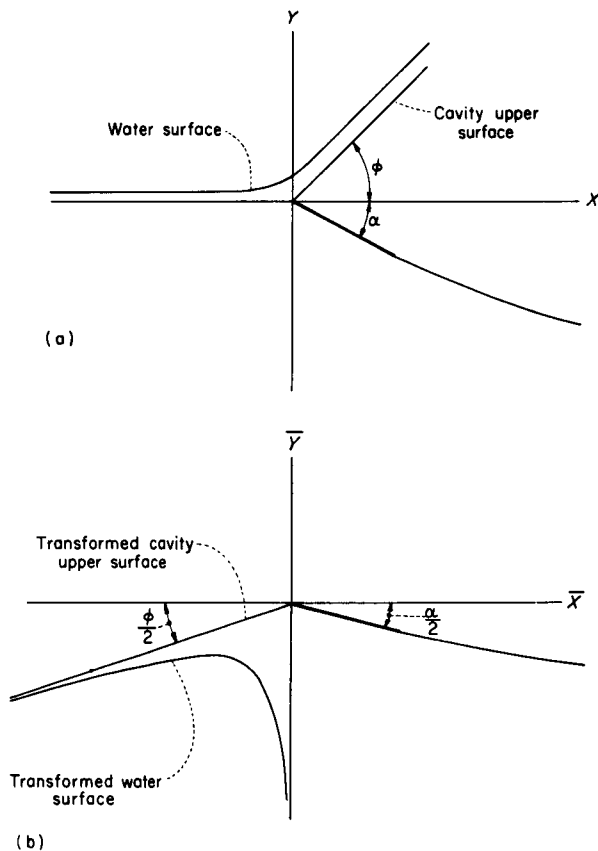
For $A_0 = \alpha$, that is, $A'_0 = 0$,

$$\alpha + \epsilon = \frac{C_D}{C_L} = \frac{\frac{\pi}{2} \alpha \left(C_0 + C_1 - \frac{C_2}{2} \right) + \frac{\pi}{2} \left[\left(\frac{C_1}{4} - \frac{C_2}{2} \right) A_1 + \left(\frac{C_0 + C_1 + \frac{C_4}{2}}{2} \right) A_2 - \frac{A_4 C_2}{4} \right]}{\frac{\pi}{2} \left(C_0 + C_1 - \frac{C_2}{2} \right)} \quad (108)$$

Therefore

$$\epsilon = \frac{(C_1 - 2C_2)A_1 + (2C_0 + 2C_1 + C_4)A_2 - A_4C_2}{4\left(C_0 + C_1 - \frac{C_2}{2}\right)} \quad (109)$$

The value of ϵ given by equation (109) is adequate only for the case of small angle of attack and camber and depth-chord ratios larger than about 1. At small depth-chord ratios it will be shown subsequently that the spray angle becomes very large even for small angles of attack. When such a flow is transformed by $\bar{Z} = -Z$, the cavity streamline and the free surface are rotated as shown in figure 16. It is obvious from figure 16 that the boundary conditions are now different from the simple $\bar{u} = 0$ used in the small-angle theory. If a system of vortices could be located



(a) Hydrofoil, Z -plane.
(b) Equivalent airfoil, \bar{Z} -plane. $\bar{Z} = -\sqrt{Z}$.

FIGURE 16.—The hydrofoil and equivalent airfoil at large angles of attack and small depths of submersion.

to satisfy the boundary conditions along these new lines, a solution for the resulting vorticity on the foil could be obtained. Such a method would involve taking a different calculated spray angle for each depth and angle of attack in order to locate the image vortex or array of vortices. Also, for large angles of attack and spray angles in the linearizing assumption of $\bar{v} \ll V$ is not adequate. When the lift was calculated, these difficulties were avoided by using Green's solution which takes the effect of the spray angle into account. It can be seen in figure 2 that, as the angle of attack increases, the ratio of $\frac{C_L}{C_{L,\infty}}$ diminishes; therefore, the image vortex must have less influence on the resulting hydrofoil vorticity for large angles of attack. An approximation to the correct hydrofoil-vorticity distribution for finite angles of attack operating near the free water surface can be obtained by using the model shown in figure 12, and increasing the value of d/c used so that the resulting $\frac{C_L}{C_{L,\infty}}$ corresponds to that given by Green. Thus, for large angles of attack, camber, and finite aspect ratio an effective depth of submersion, $(d/c)_e$ should be used to determine the coefficients in equation (109). The value of $(d/c)_e$ is the value of d/c on the $\alpha = 0$ line in figure 2 corresponding to the value of $m = m_e$, where

$$m_e = \frac{C_L}{C_{L,\infty}} \frac{\pi}{2} = \frac{m(\alpha + \alpha_c - \alpha_i)}{m(\alpha + \alpha_c - \alpha_i)_\infty} \frac{\pi}{2} \quad (110)$$

The value of the C coefficients are then determined for $(d/c)_e$ and $A_0 = \alpha - \alpha_i$.

A sample calculation of the drag coefficient is given in the appendix. Experience has shown that the value of ϵ , and thus the drag coefficient, is not greatly affected by the depth of submersion. In fact, a rough approximation to ϵ may be obtained by assuming $C_0 = \alpha - \alpha_i$, and $C_n = A_n$ in equation (109).

Center of pressure: The linearized expression for the center of pressure of a finite-aspect-ratio, supercavitating hydrofoil operating at zero cavitation number and finite depth of submersion is from reference 1

$$x_{cp,1} = \frac{C_{m,1}}{C_{L,1}} = \frac{1}{16} \frac{5C_0 + 7C_1 - 7C_2 + 3C_3 - \frac{C_4}{2}}{C_0 + C_1 - \frac{C_2}{2}} \quad (111)$$

where the C coefficients are determined at the

effective depth of submersion given by equation (110) and for $A_0 = \alpha - \alpha_t$. Superimposed on this flow is the crossflow component of lift which is assumed to be distributed uniformly over the chord and acting in a direction normal to the chord line. Thus, the distance from the leading edge to the center of pressure of the crossflow-lift component $x_{cp,c}$ is given by

$$x_{cp,c} = 0.5c \quad (112)$$

This assumption, of course, is crude and accurate only for a flat plate. For cambered surfaces the crossflow will not be uniformly distributed and for low-drag cambered sections such as the five-term section the crossflow is probably concentrated on the rearward portion of the hydrofoil.

The center of pressure of the combined flows may be obtained by adding the moments contributed by the two components given by equations (111) and (112) and dividing by the total lift as

$$x_{cp} = \frac{C_{L,1}x_{cp,1} + 0.5C_{L,c}}{C_L} c \quad (113)$$

As in the case of ϵ , a few calculations reveal that a fair approximation for $x_{cp,1}$ is obtained by using $C_0 = \alpha - \alpha_t$ and $C_n = A_n$ in equation (111). A sample calculation of the center-of-pressure location is given in the appendix.

Design charts and tables.—With equation (99) the lift coefficient has been computed for the four sections of interest at depth-chord ratios of 0.25, 0.50, 1.00, 2.00, and 5.00 for aspect ratios of 1, 3, and 5. These results are presented in figures 17, 18, 19, and 20 for the circular arc, Tulin-Burkart, three-term, and five-term sections, respectively. Flat-section data are included as the $C_{L,a} = 0$ case. Similar drag-coefficient data computed by using equations (100) and (109) are presented in figures 21 to 24. These lift- and drag-coefficient data are also presented in tabular form in tables I to V along with the calculated location of the center of pressure and other results which are considered to be useful.

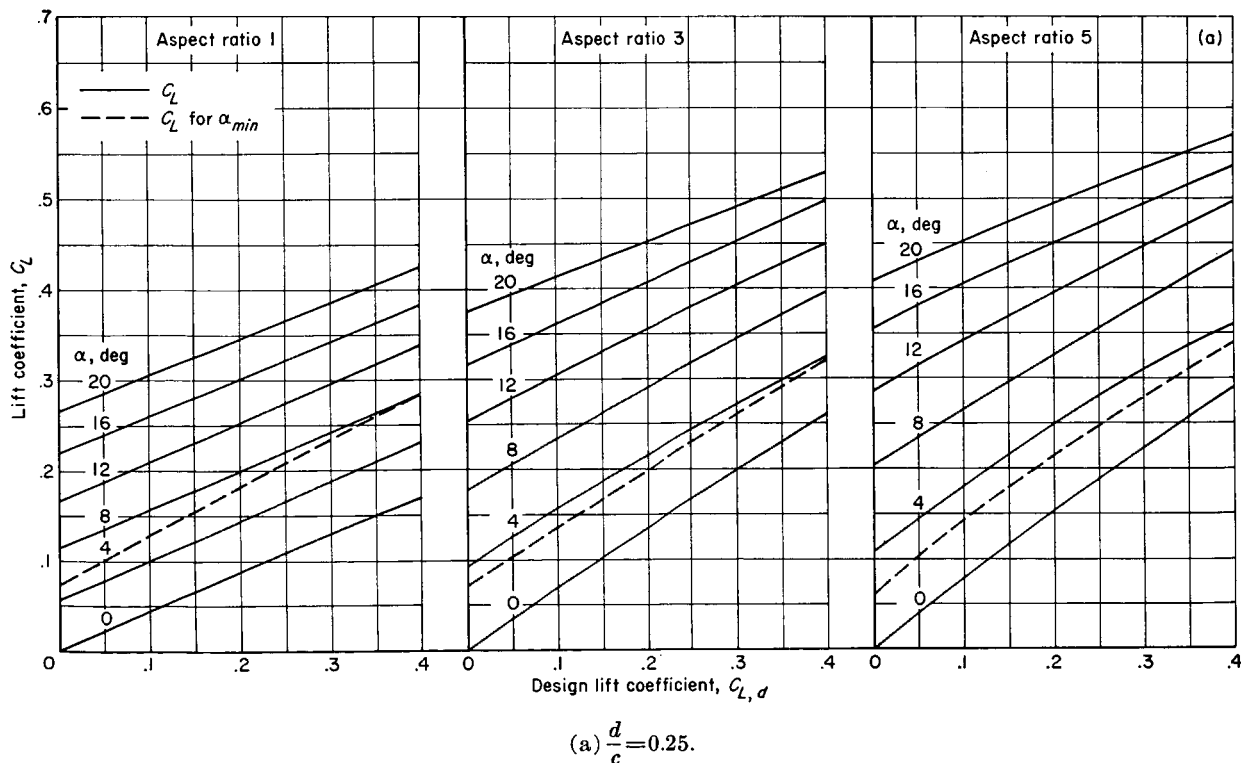


FIGURE 17.—Lift coefficient for circular-arc section including the minimum angle of attack for maximum L/D for $t/c=0.03$ at $x/c=0.2$.

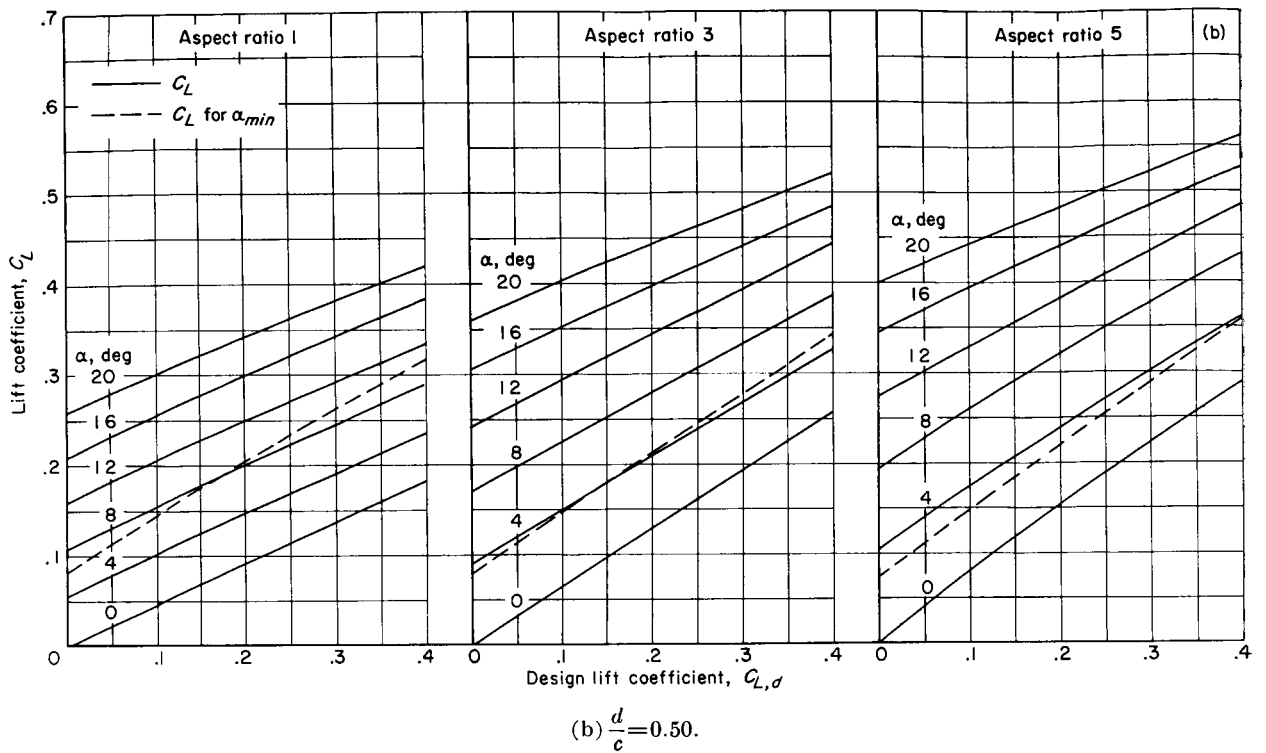


FIGURE 17.—Continued.

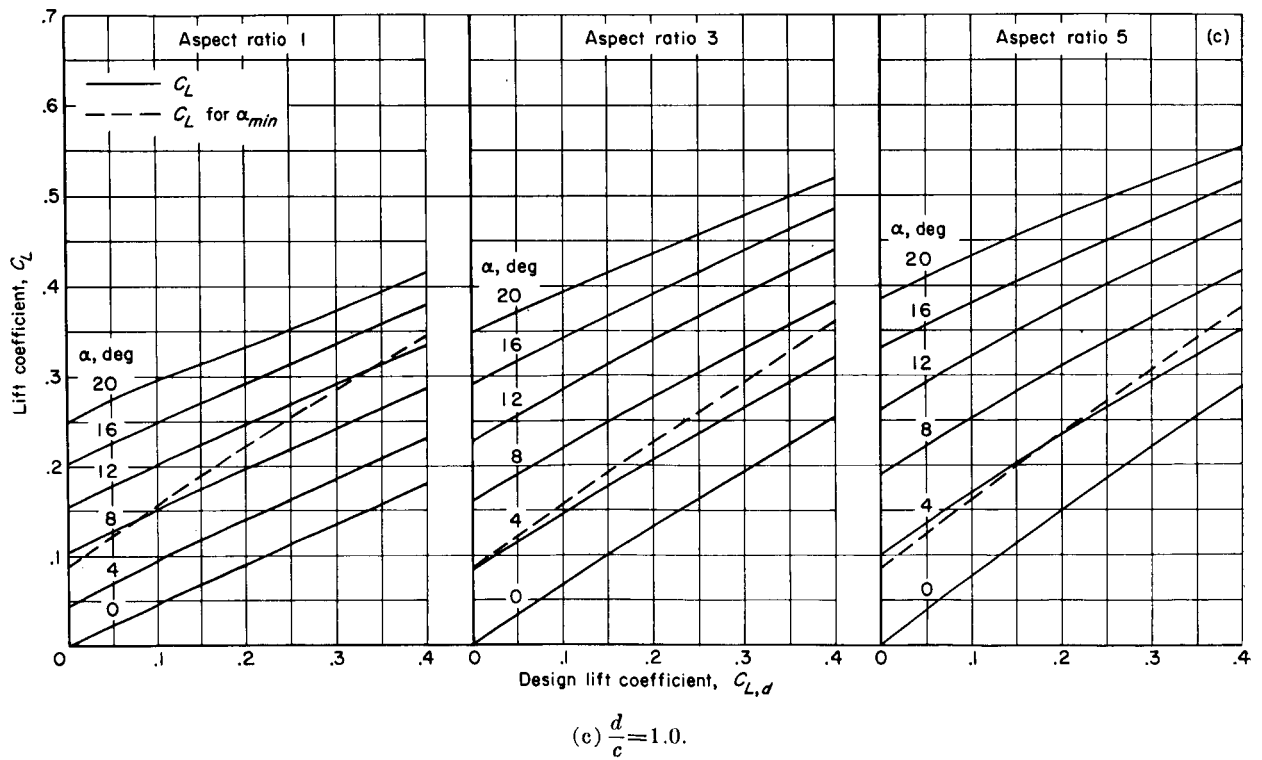


FIGURE 17.—Continued.

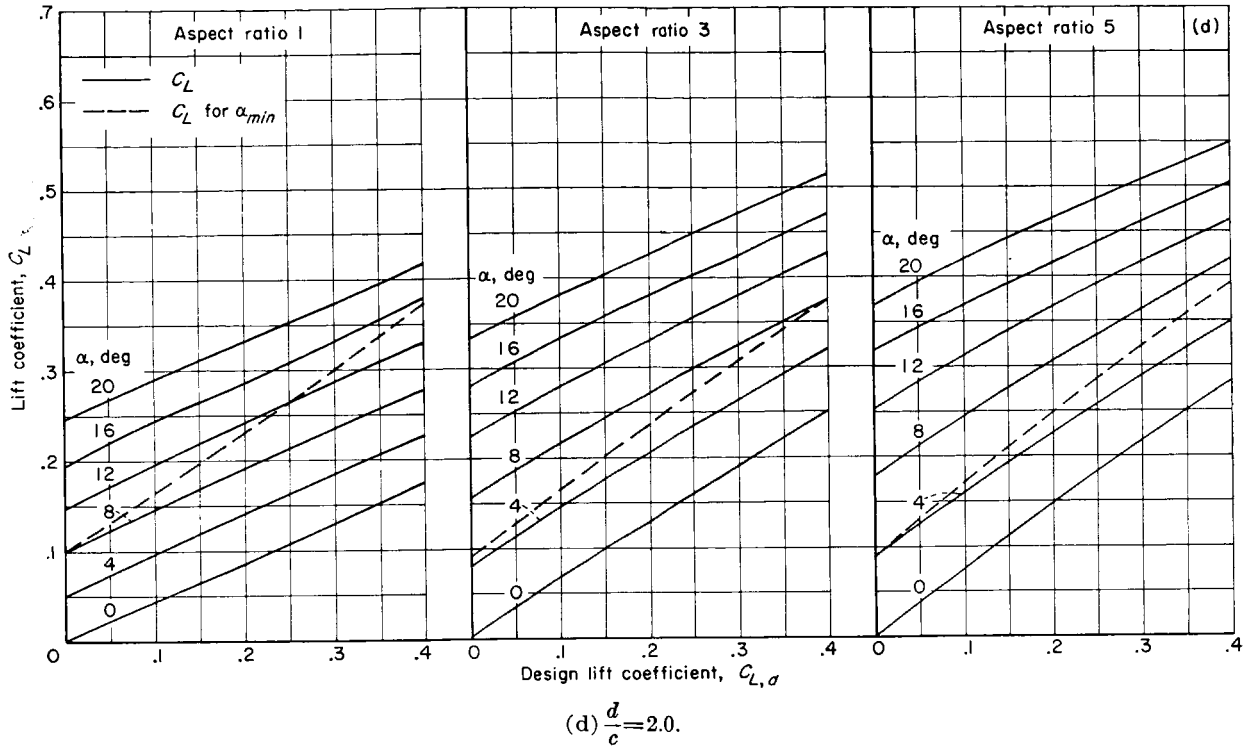


FIGURE 17.—Continued.

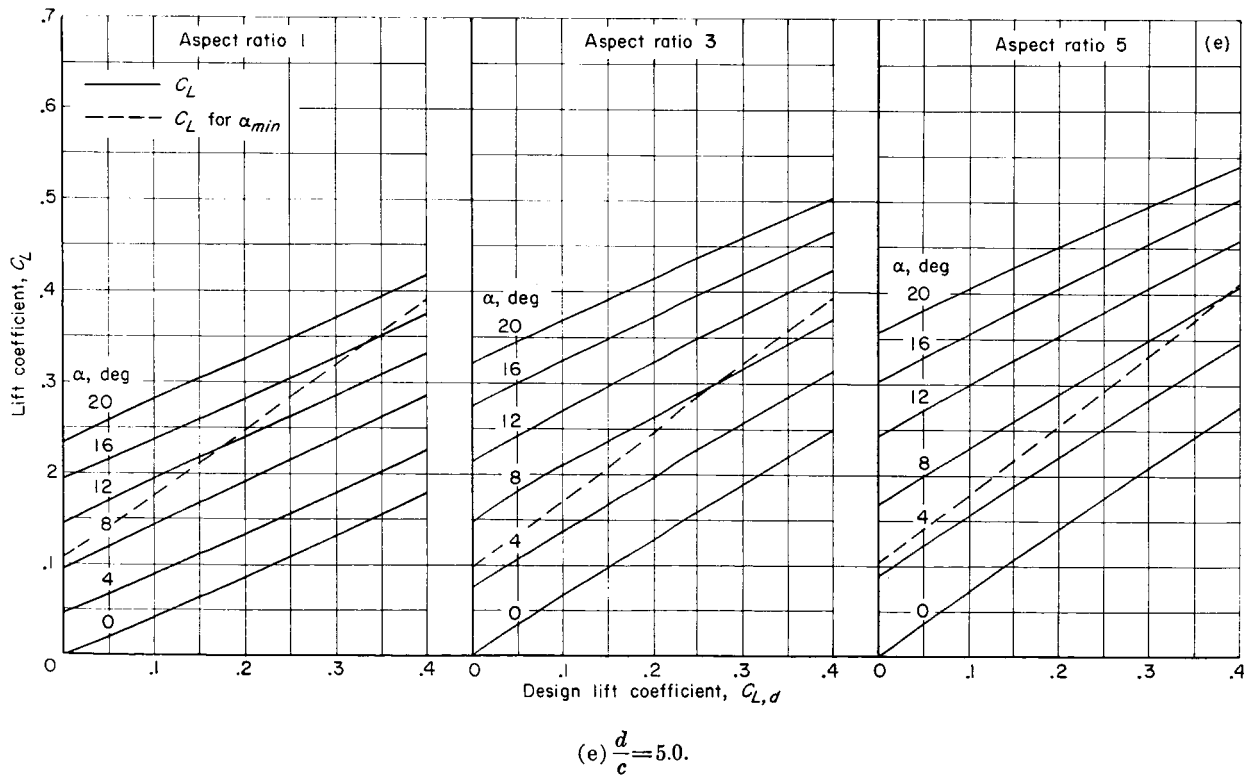


FIGURE 17.—Concluded.

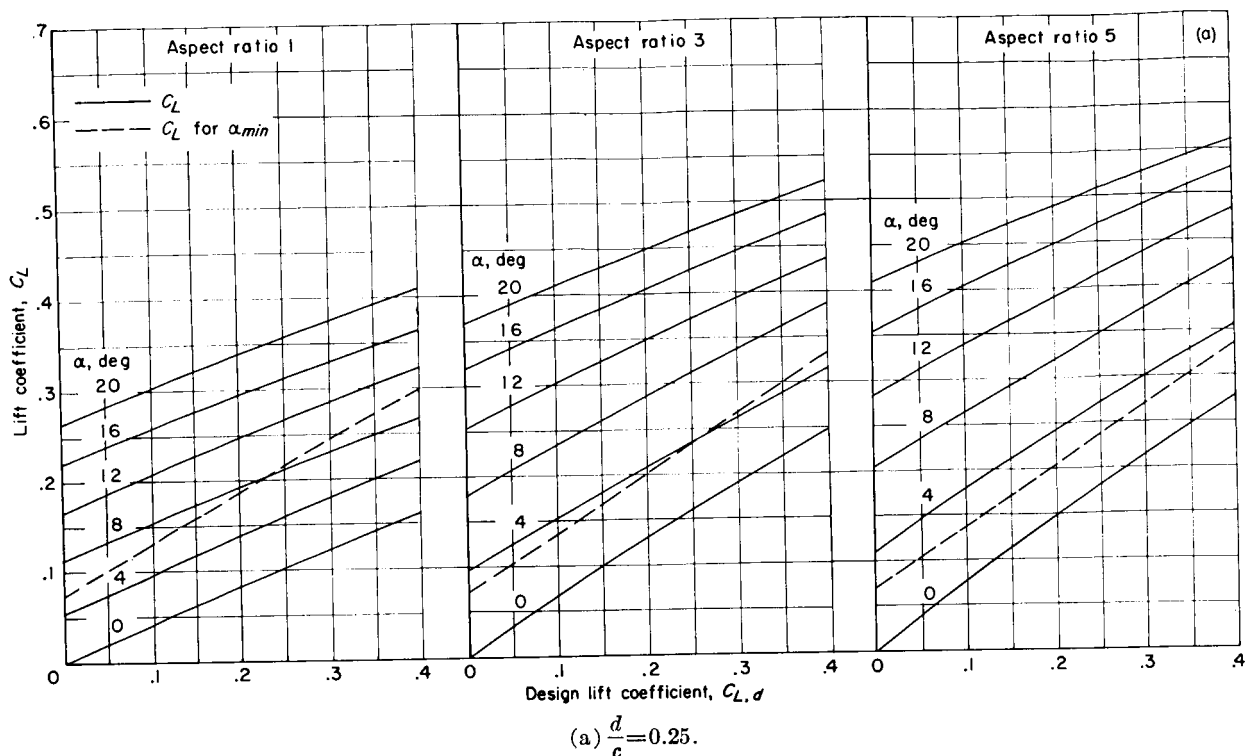


FIGURE 18.—Calculated lift coefficient for Tulin-Burkart section including the minimum angle of attack for maximum L/D for $t/c=0.03$ at $x/c=0.2$.

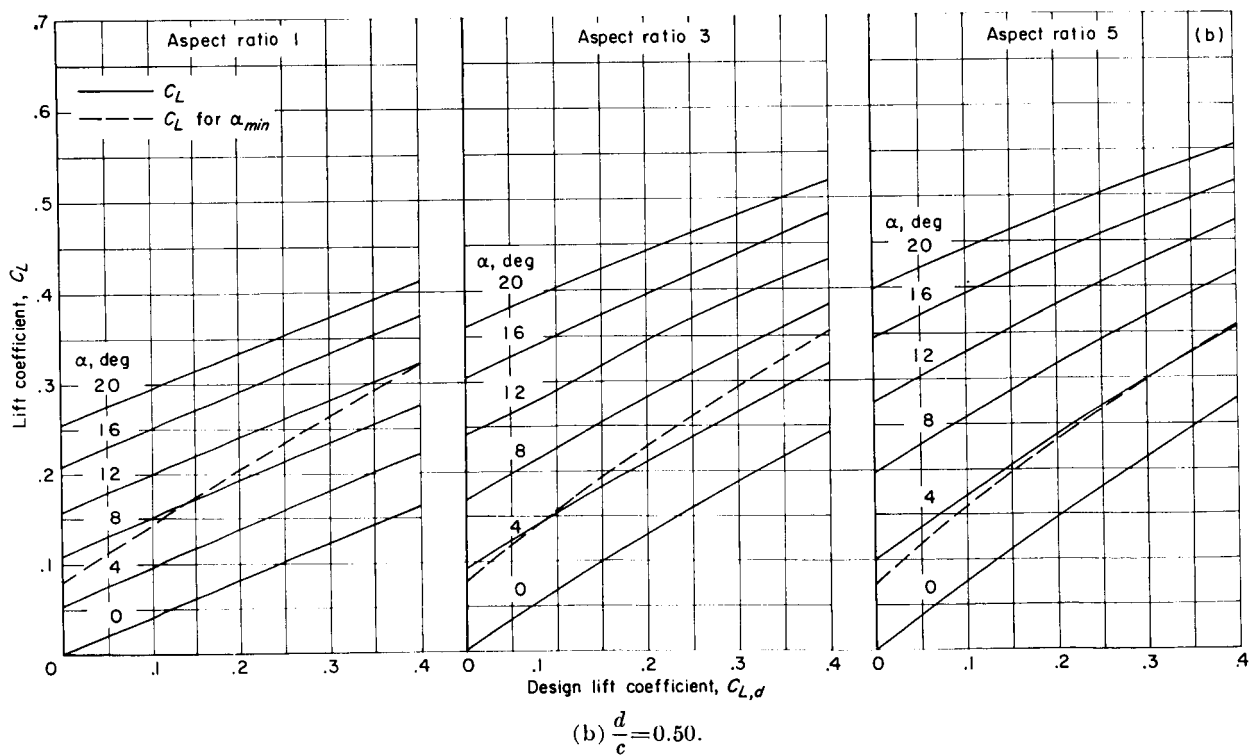


FIGURE 18.—Continued.

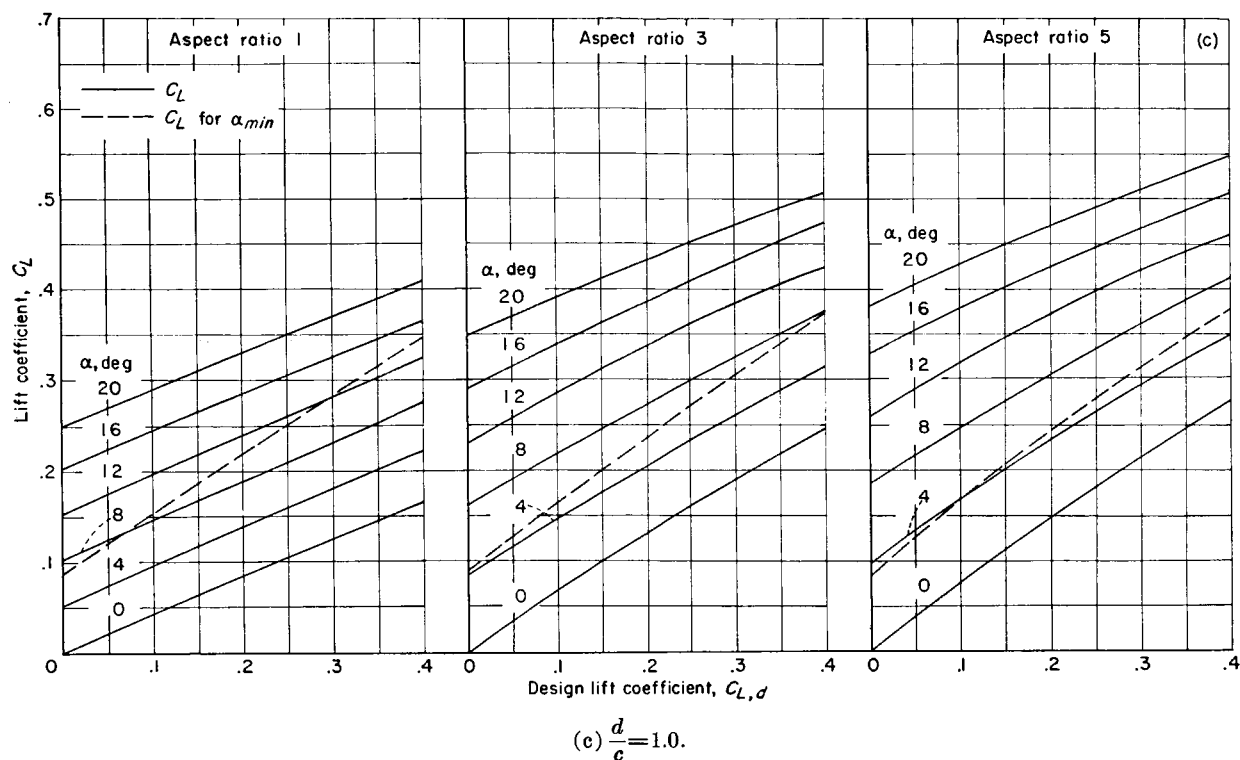


FIGURE 18.—Continued.

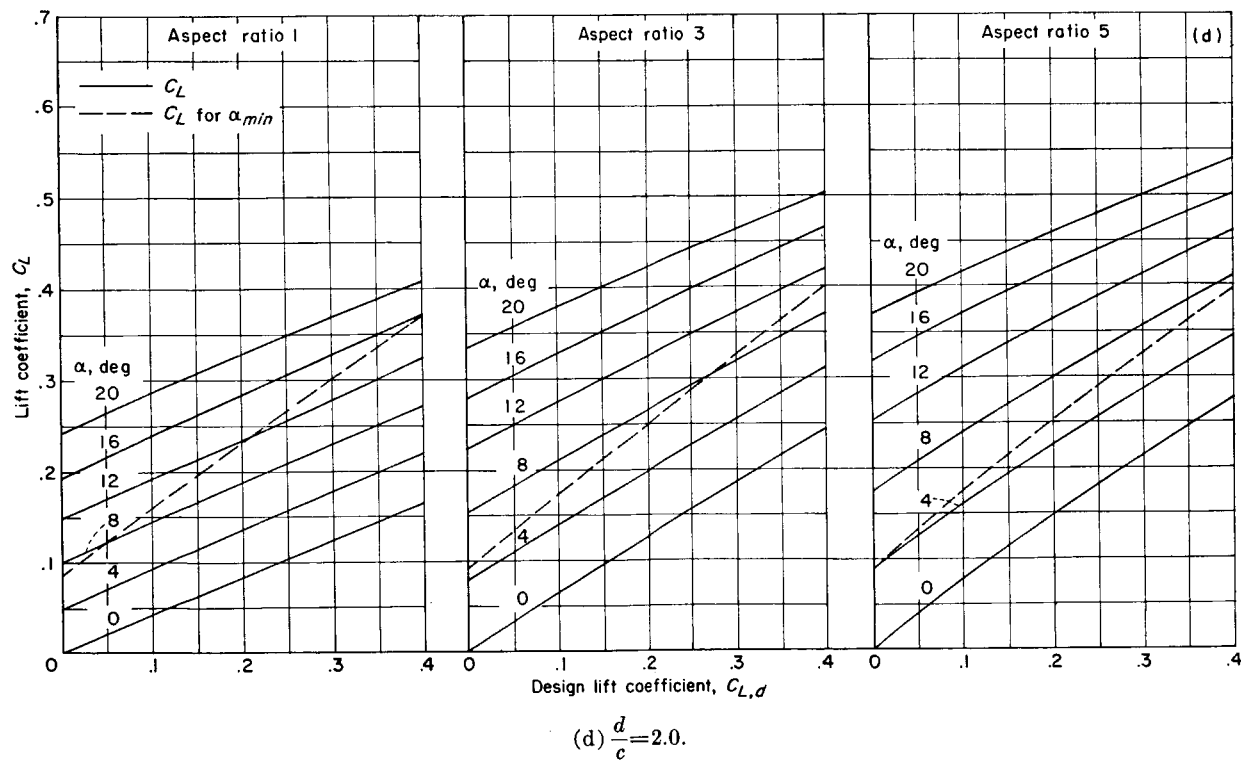


FIGURE 18.—Continued.

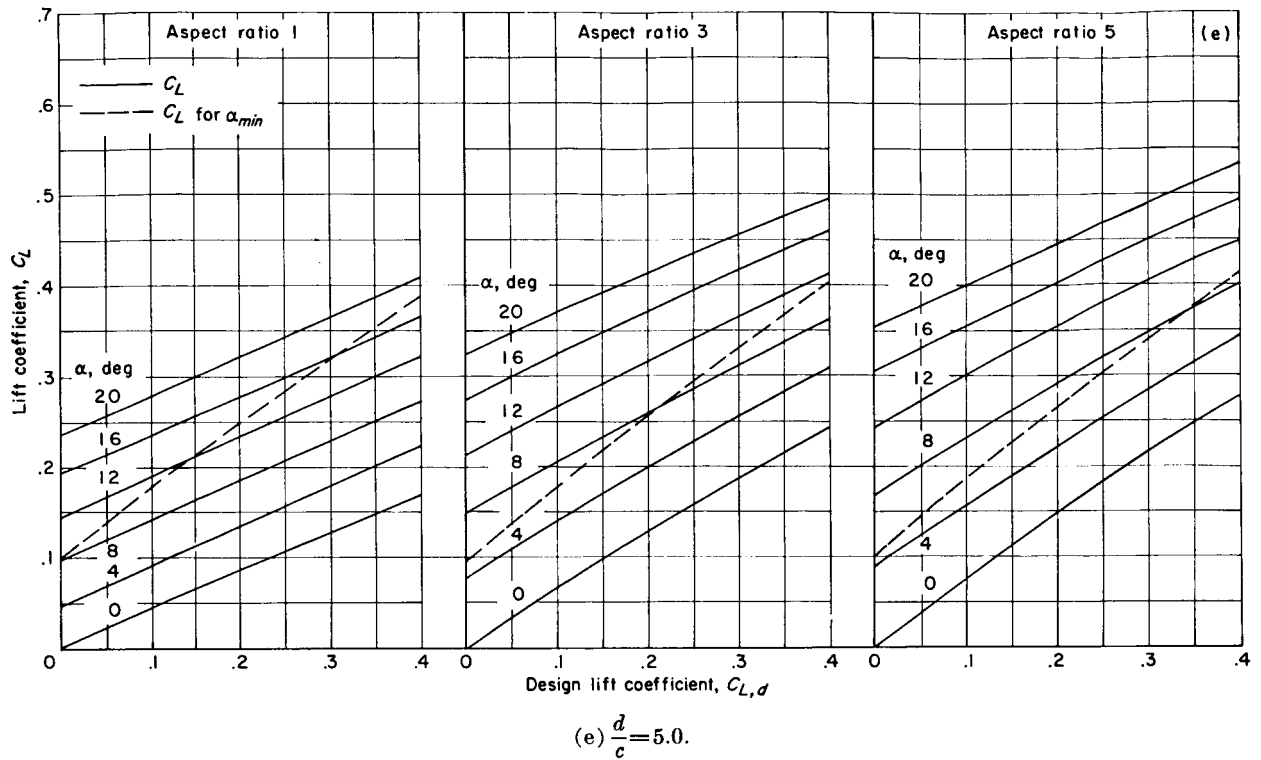
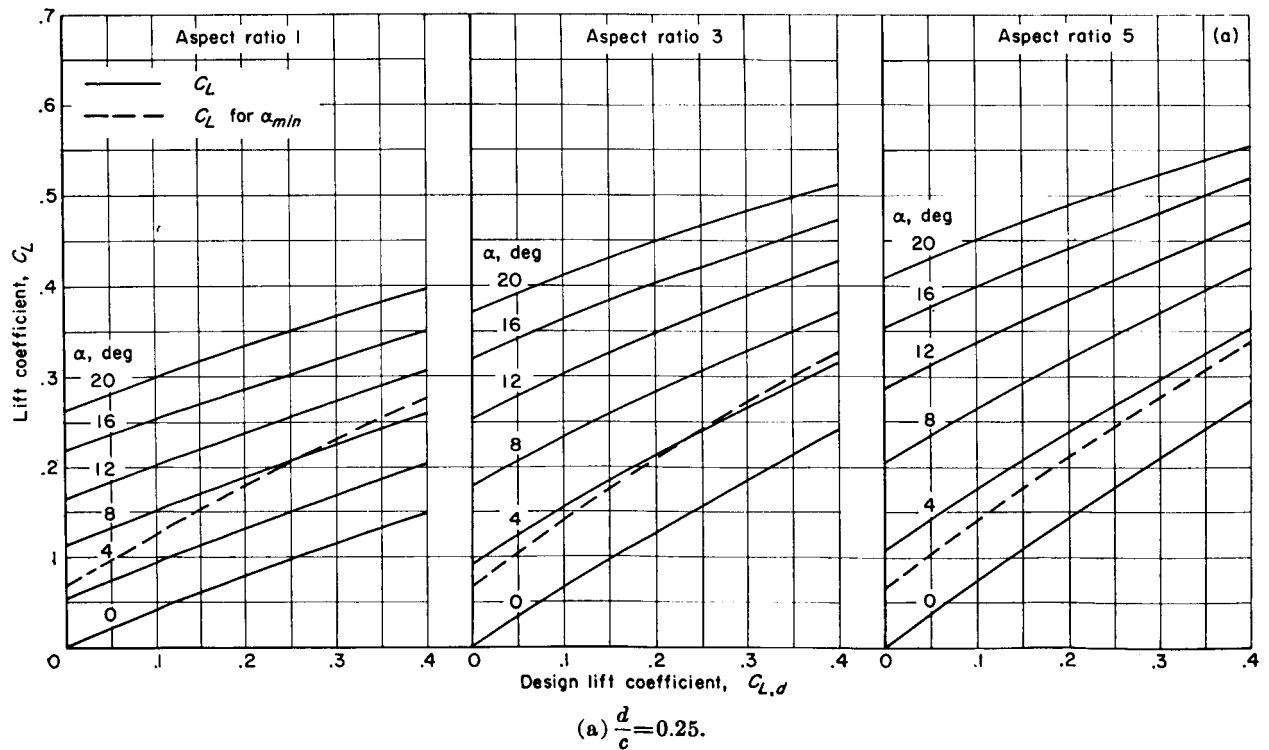
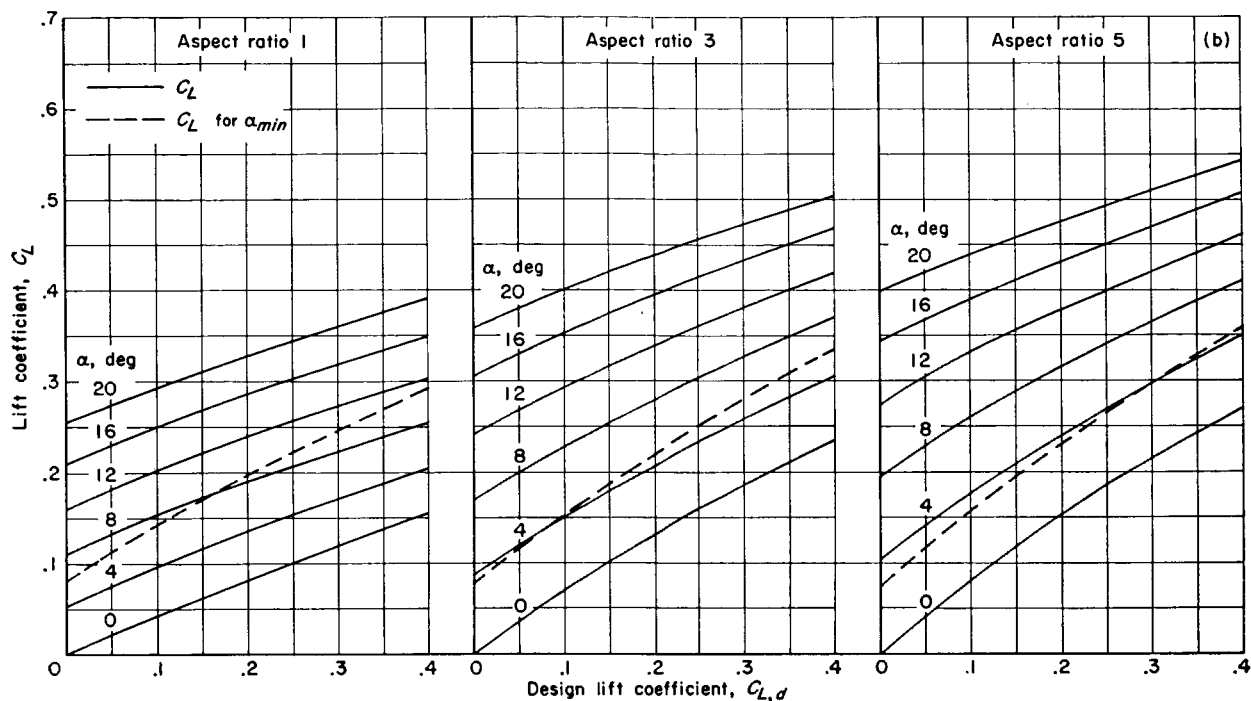


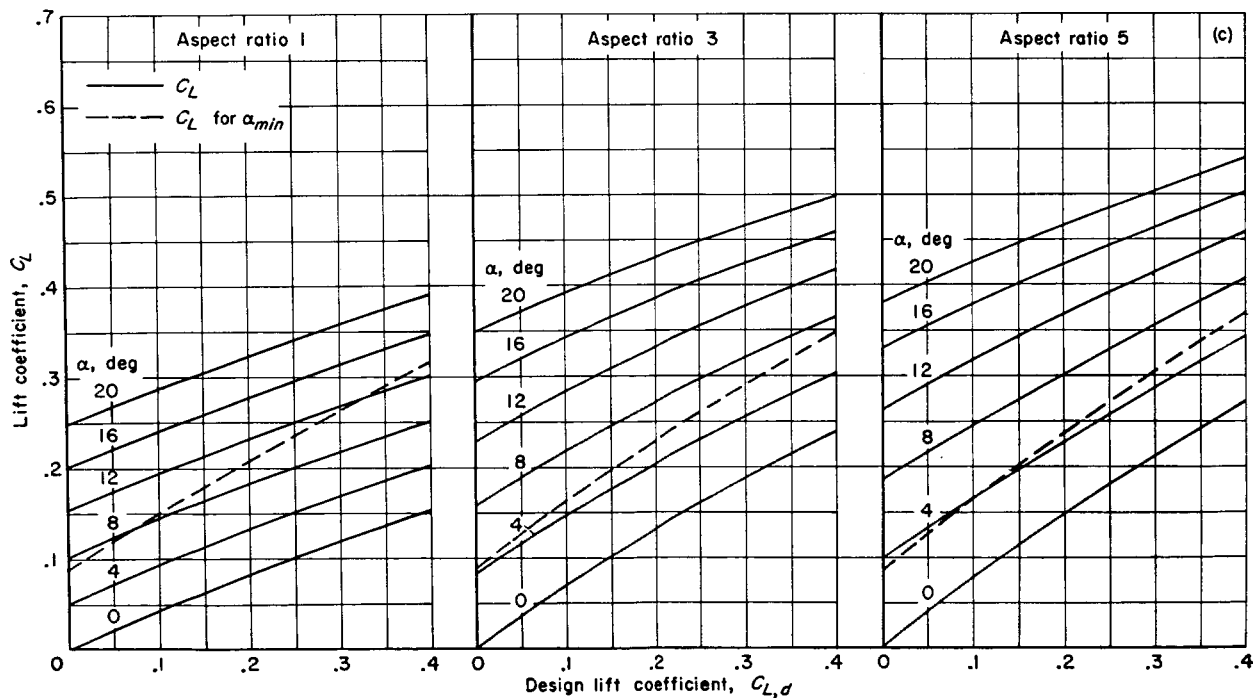
FIGURE 18.—Concluded.

FIGURE 19.—Calculated lift coefficient for a three-term section including the minimum angle of attack for maximum L/D for $t/c=0.03$ at $x/c=0.2$.



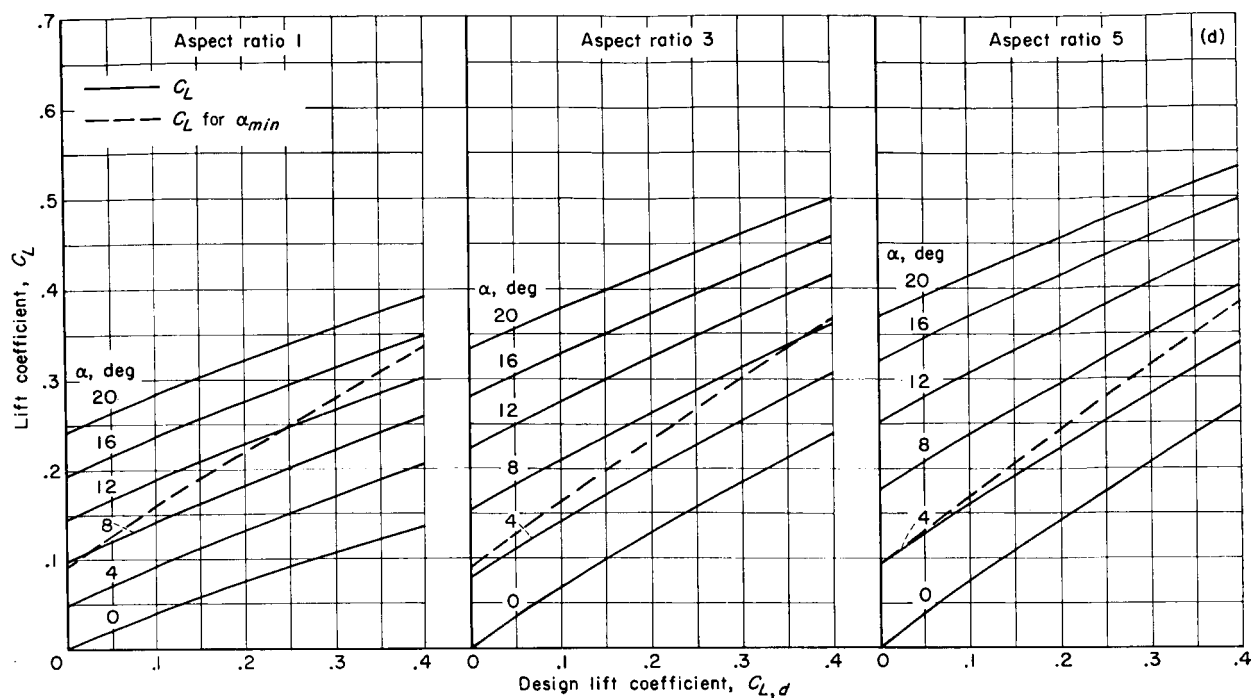
(b) $\frac{d}{c} = 0.50$.

FIGURE 19.—Continued.



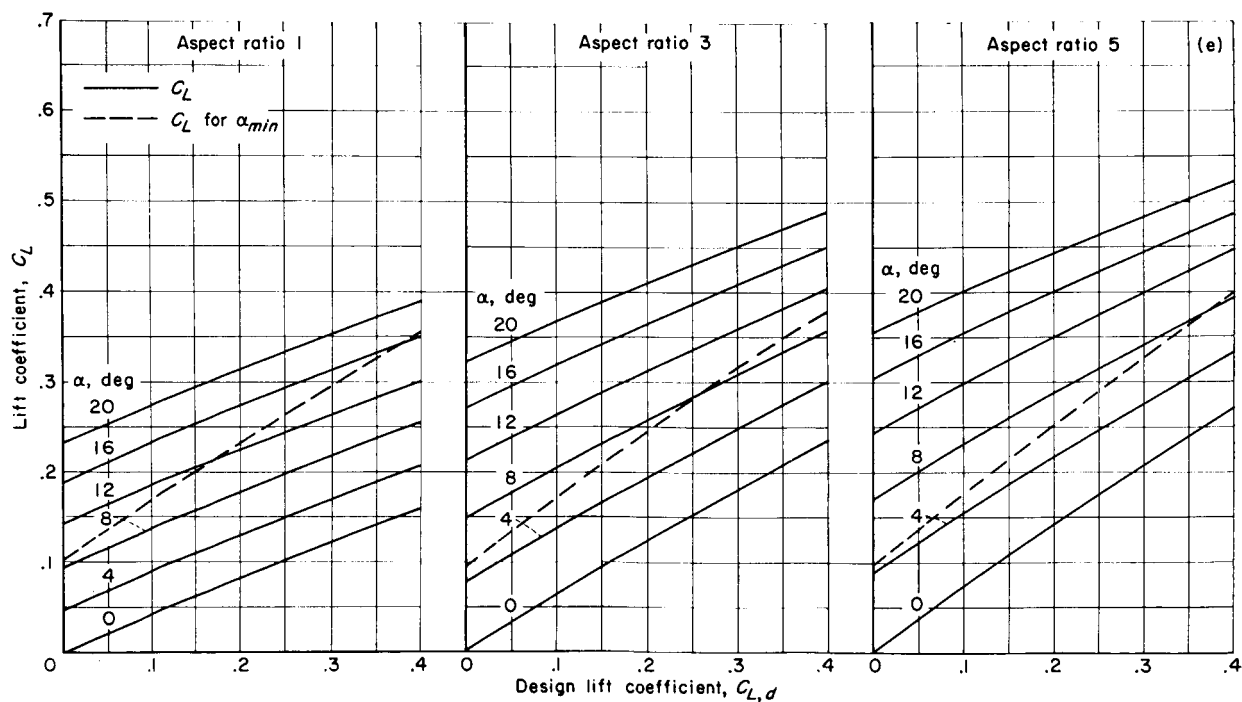
(c) $\frac{d}{c} = 1.0$.

FIGURE 19.—Continued.



$$(d) \frac{d}{c} = 2.0.$$

FIGURE 19.—Continued.



$$(e) \frac{d}{c} = 5.0.$$

FIGURE 19.—Concluded.

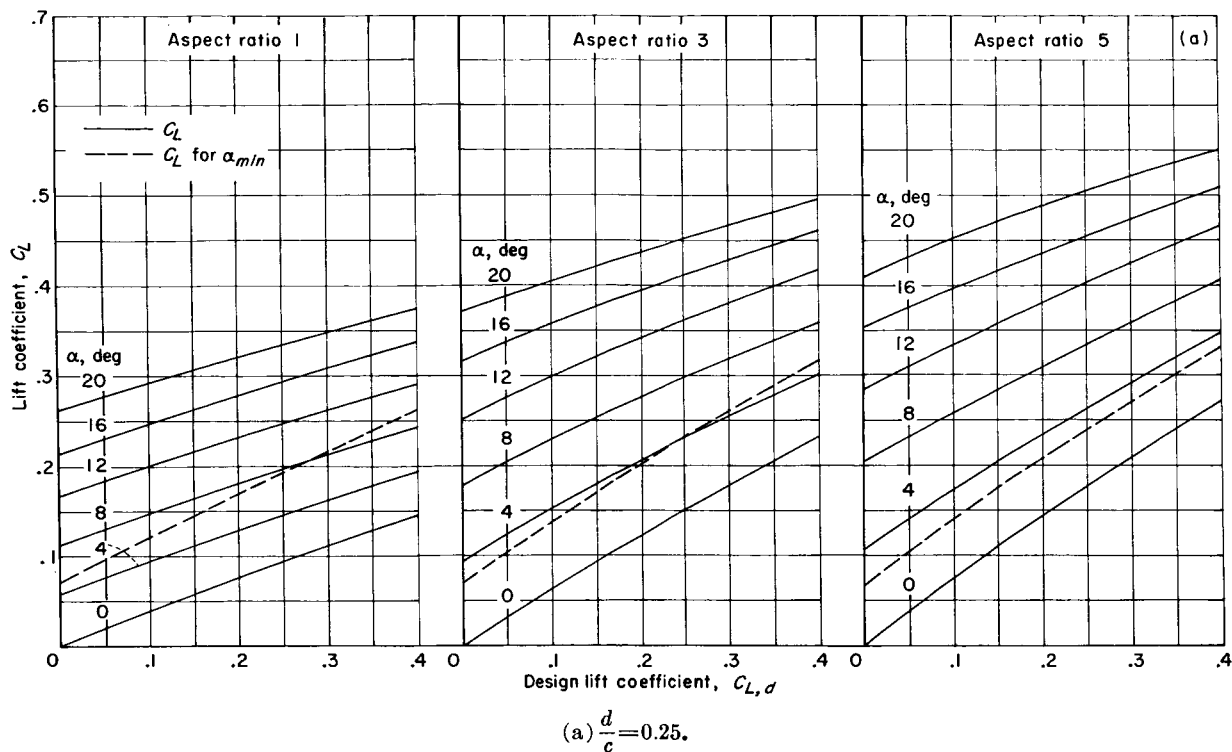


FIGURE 20.—Calculated lift coefficient for a five-term section including the minimum angle of attack for maximum L/D for $t/c=0.03$ at $x/c=0.2$.

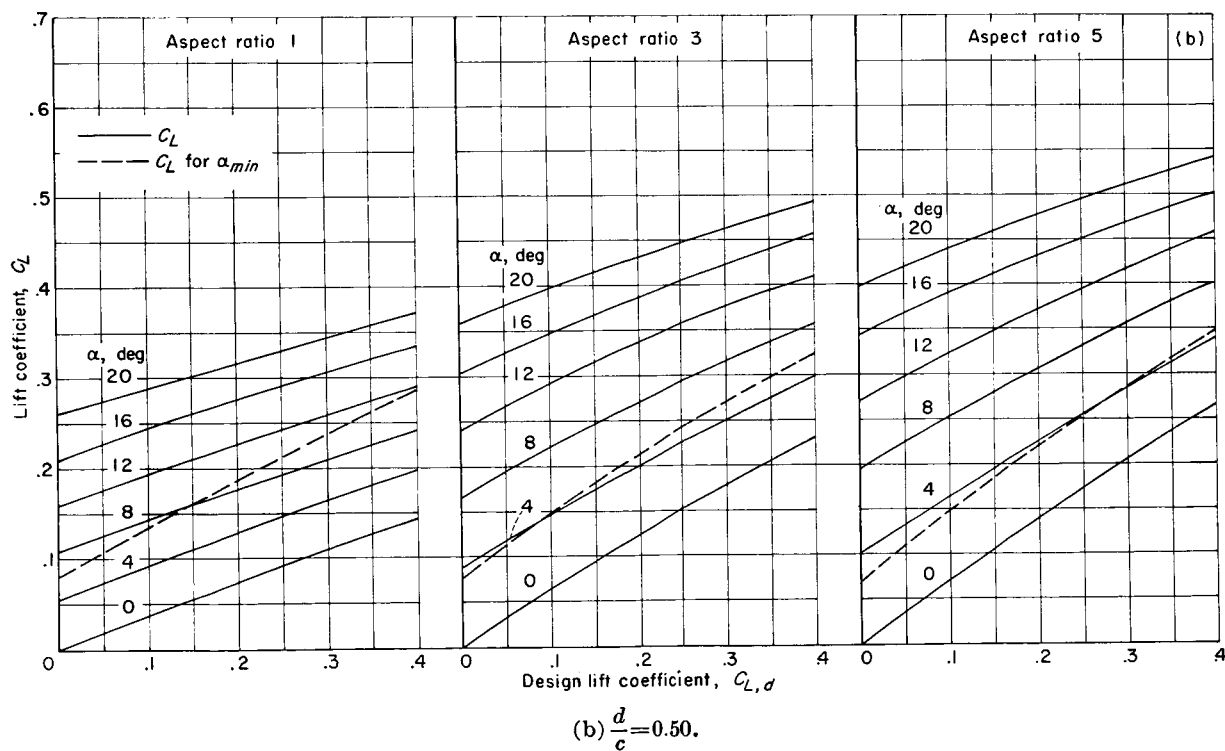


FIGURE 20.—Continued.

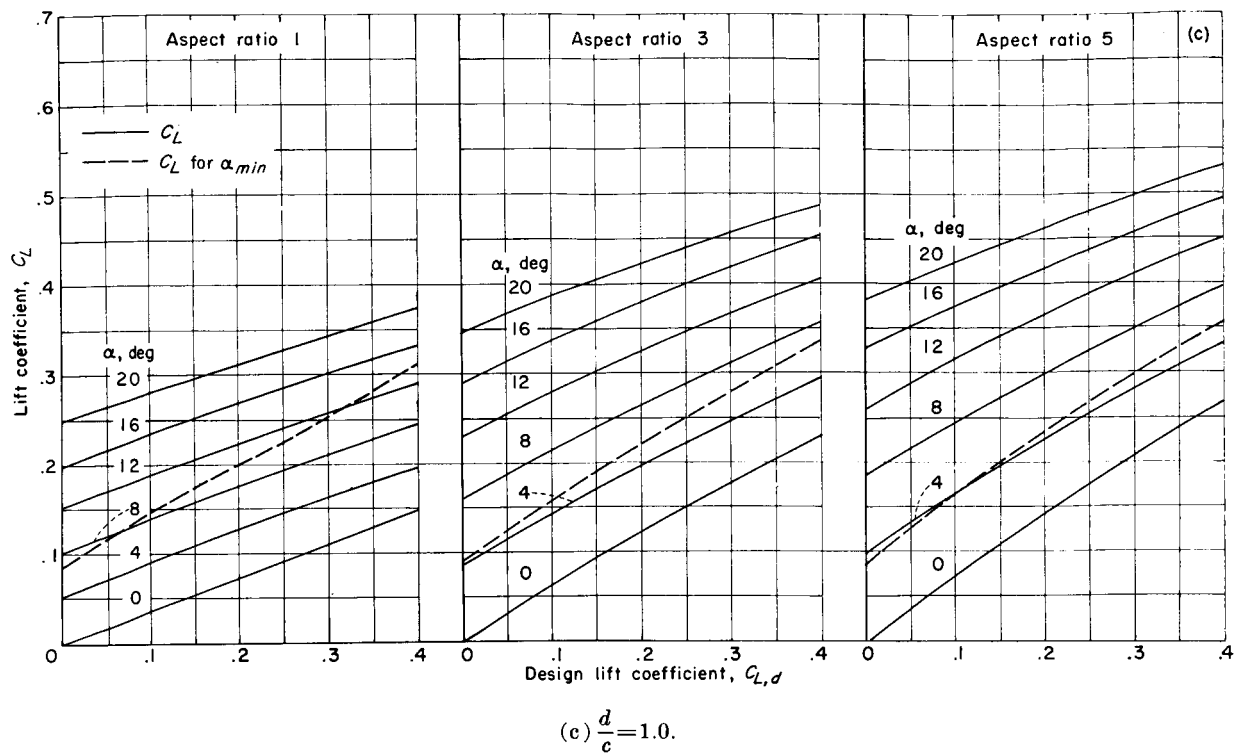


FIGURE 20.—Continued.

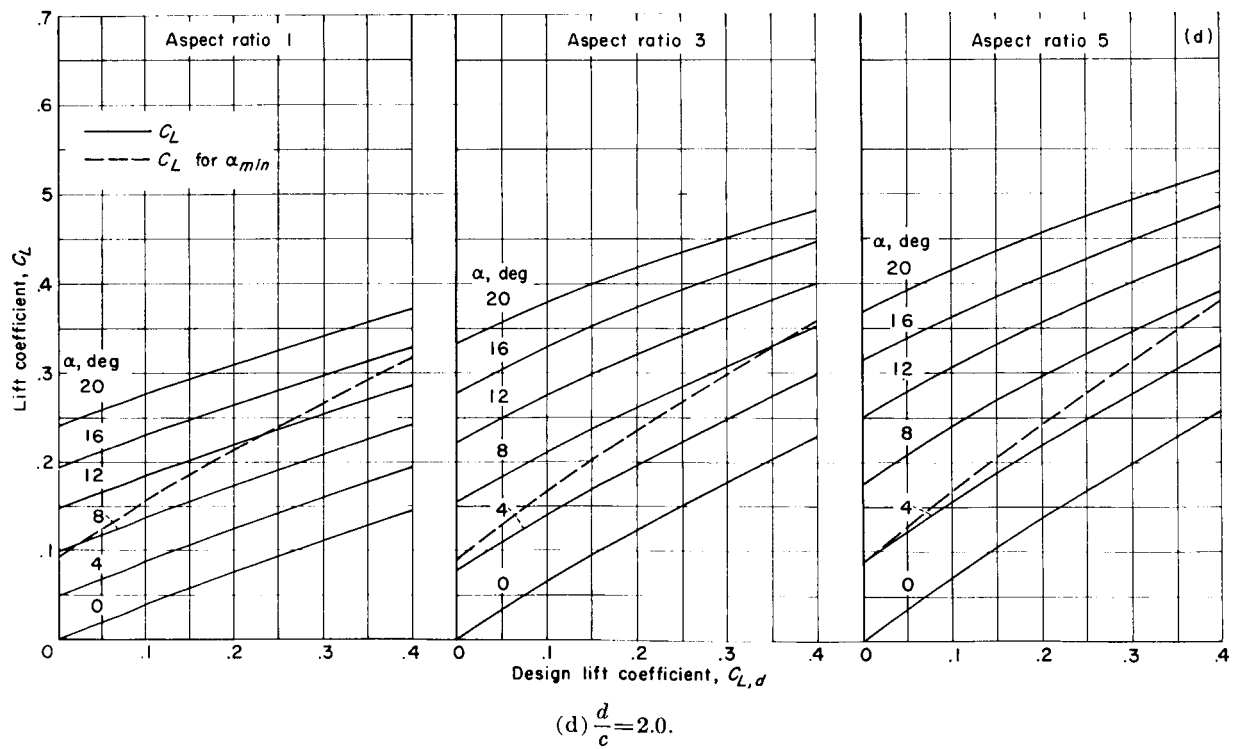


FIGURE 20.—Continued.

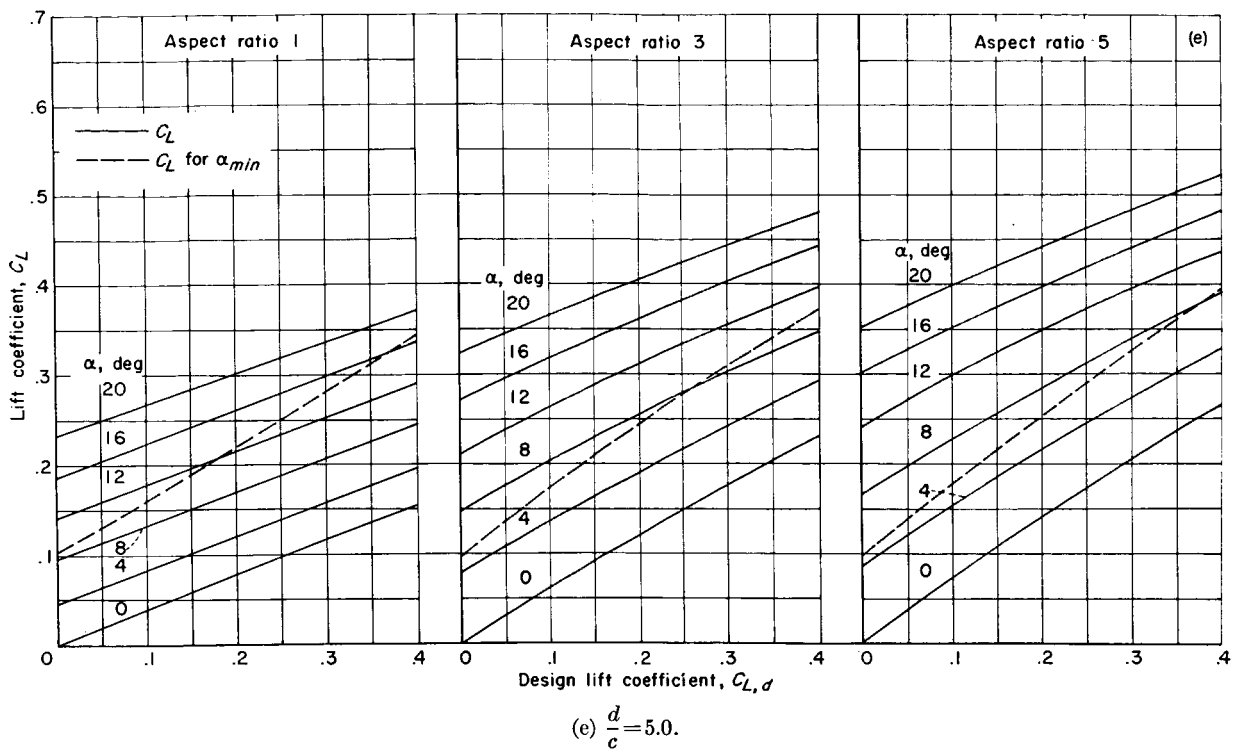
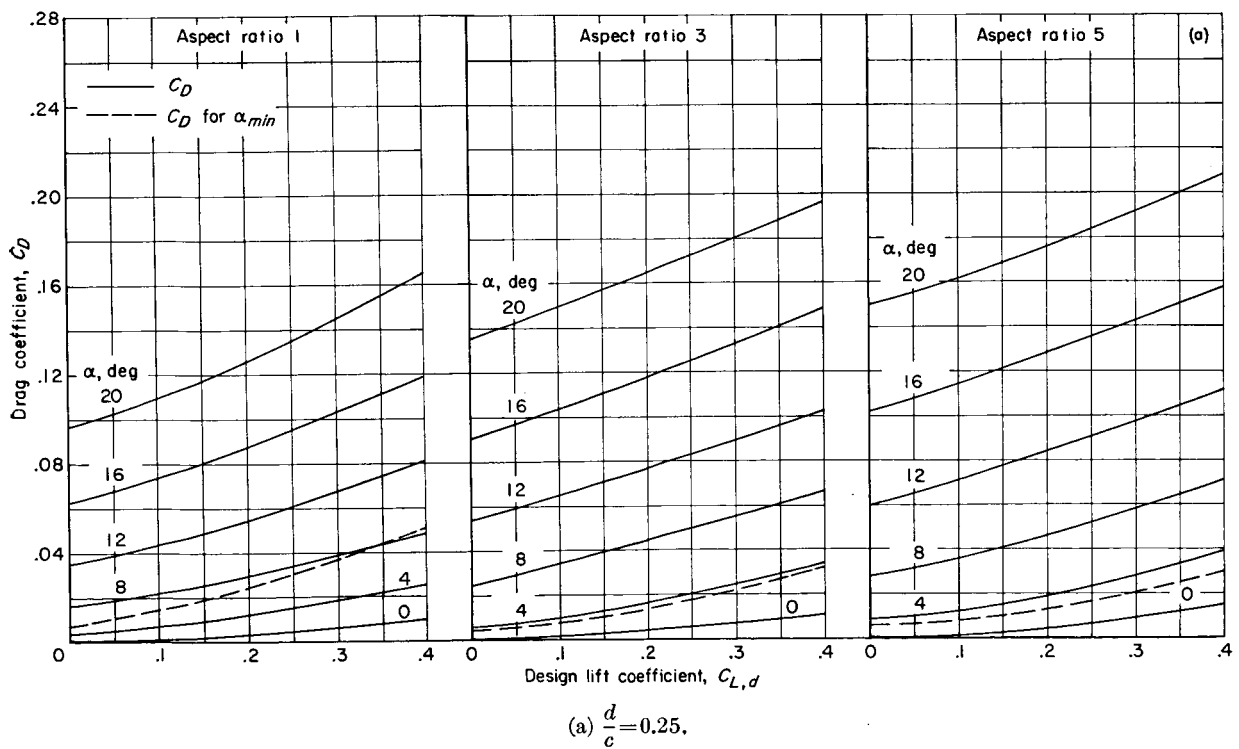
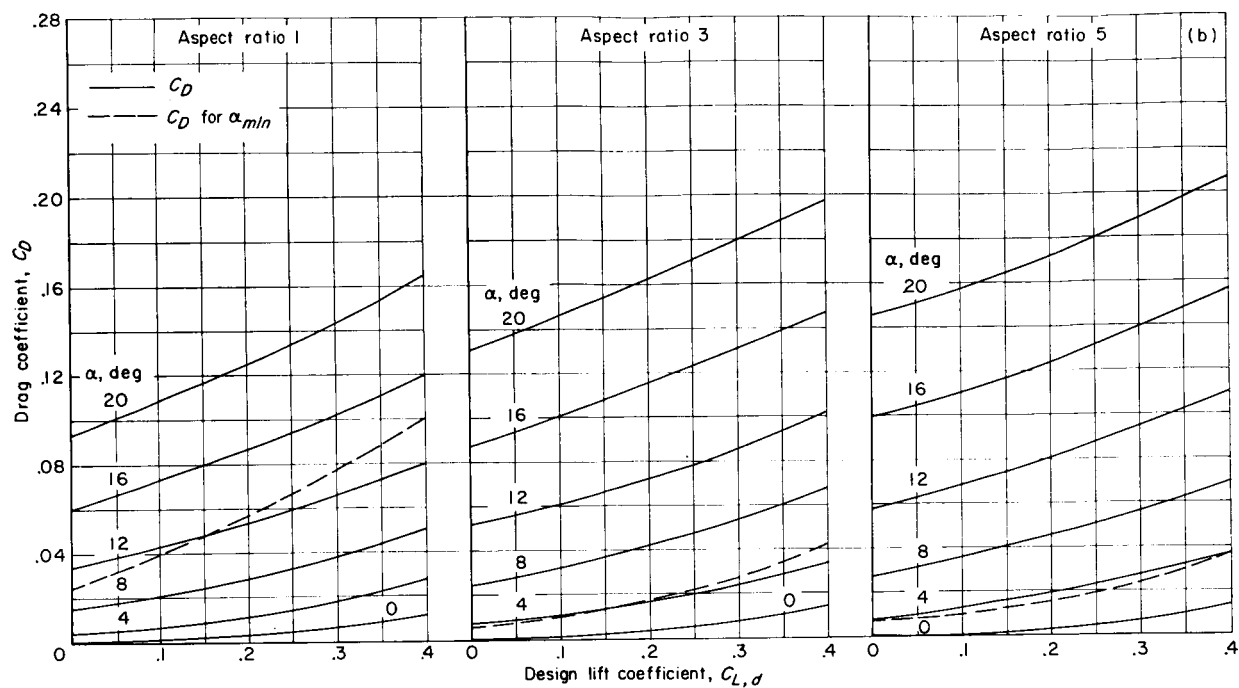


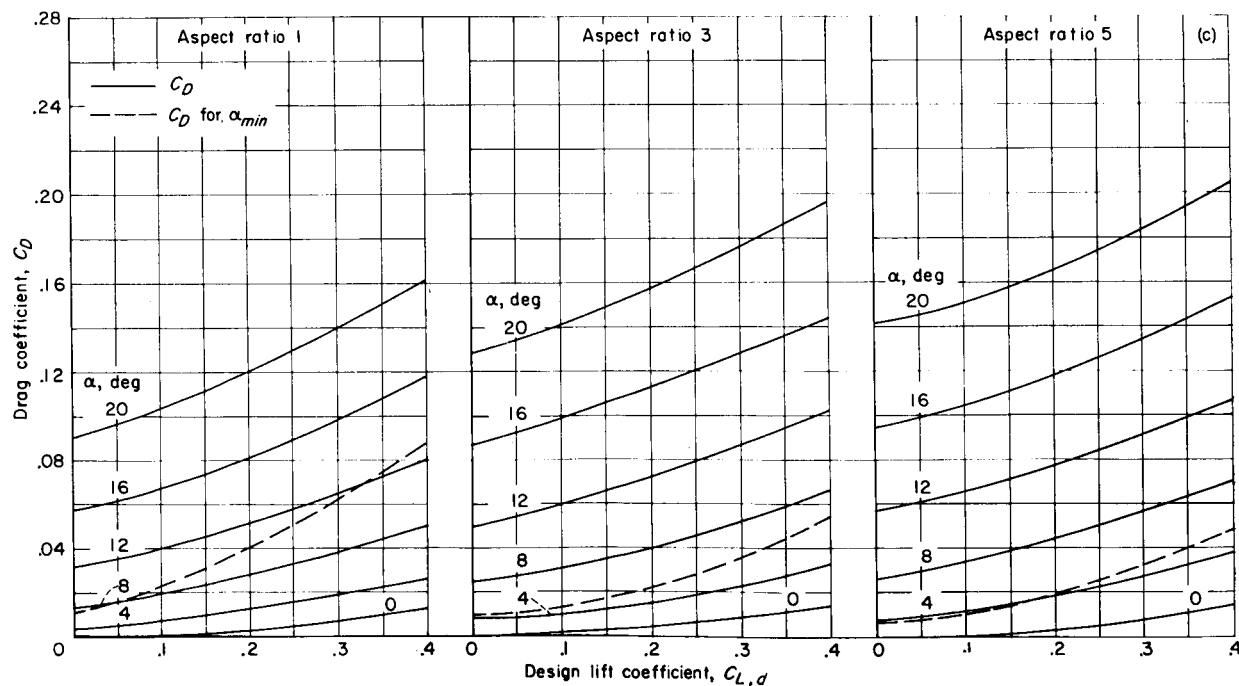
FIGURE 20.—Concluded.


 FIGURE 21.—Calculated drag coefficient for circular-arc section including the minimum angle of attack for maximum L/D for $t/c=0.03$ at $x/c=0.2$.



$$(b) \frac{d}{c} = 0.50.$$

FIGURE 21.—Continued.



$$(c) \frac{d}{c} = 1.0.$$

FIGURE 21.—Continued.

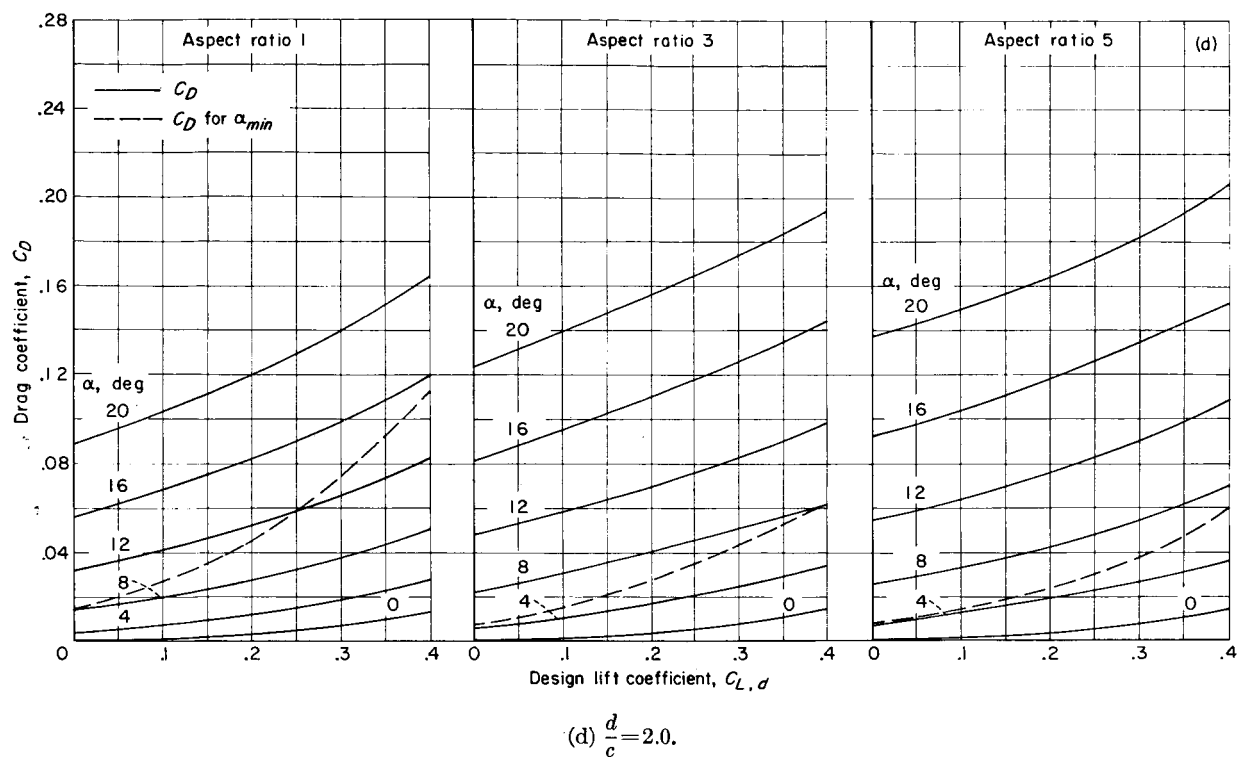


FIGURE 21.—Continued.

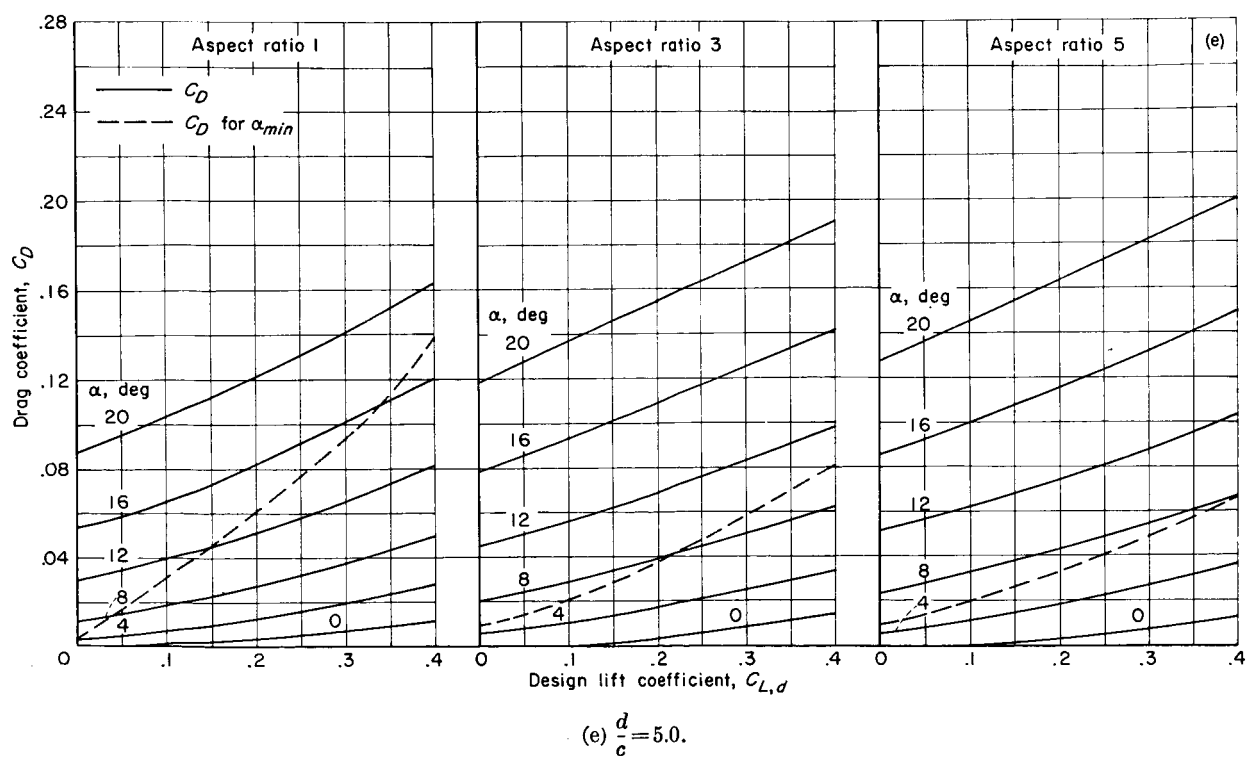


FIGURE 21.—Concluded.

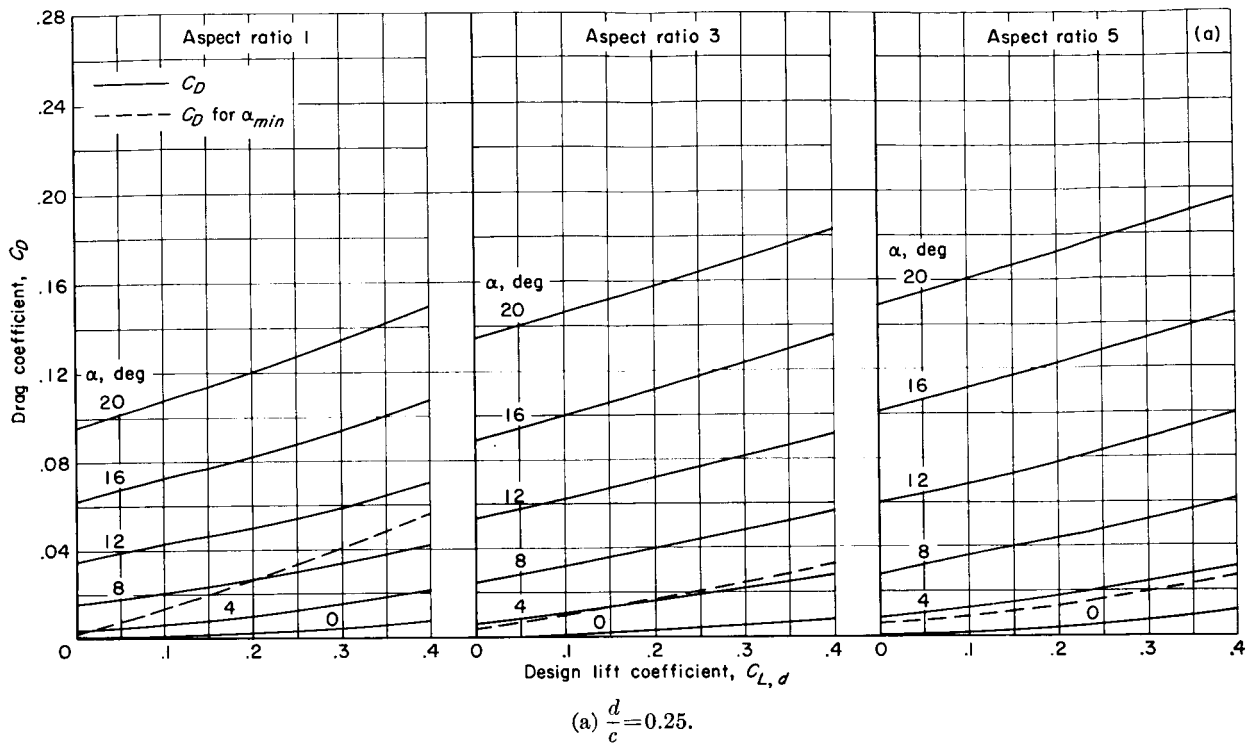


FIGURE 22.—Calculated drag coefficient for Tulin-Burkart section including the minimum angle of attack for maximum L/D for $t/c=0.03$ at $x/c=0.2$.

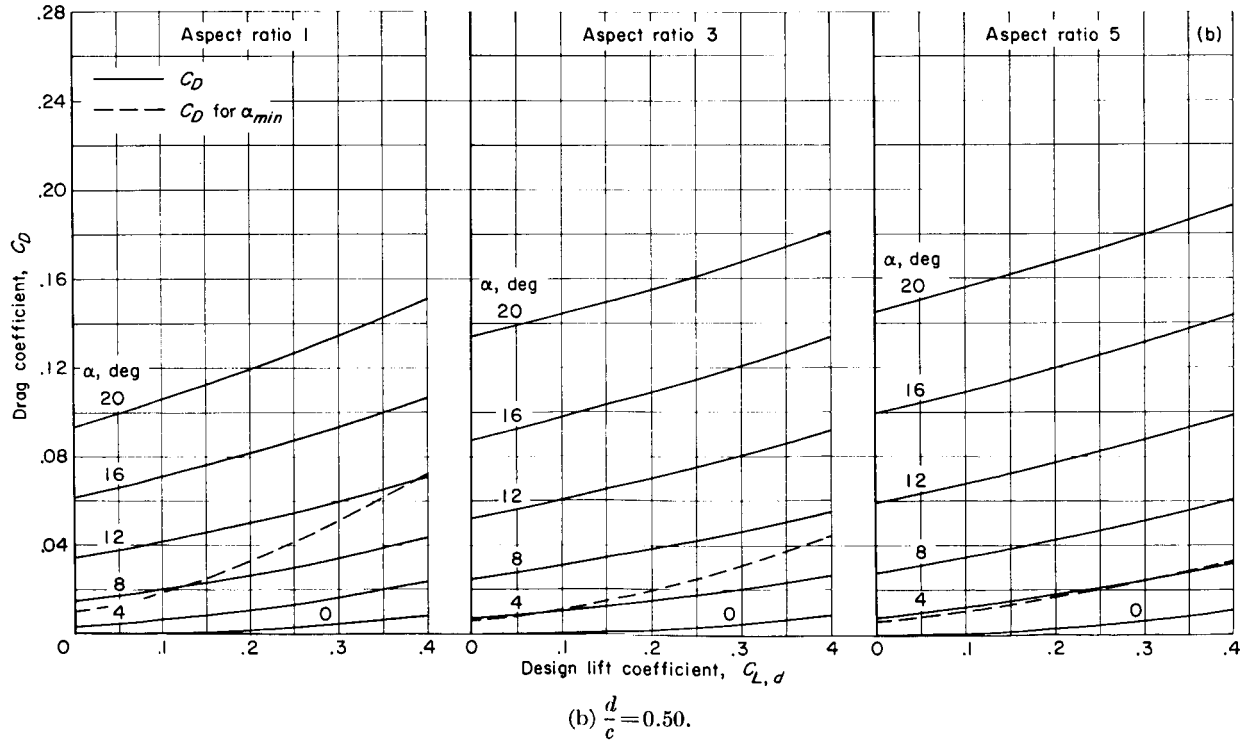


FIGURE 22.—Continued.

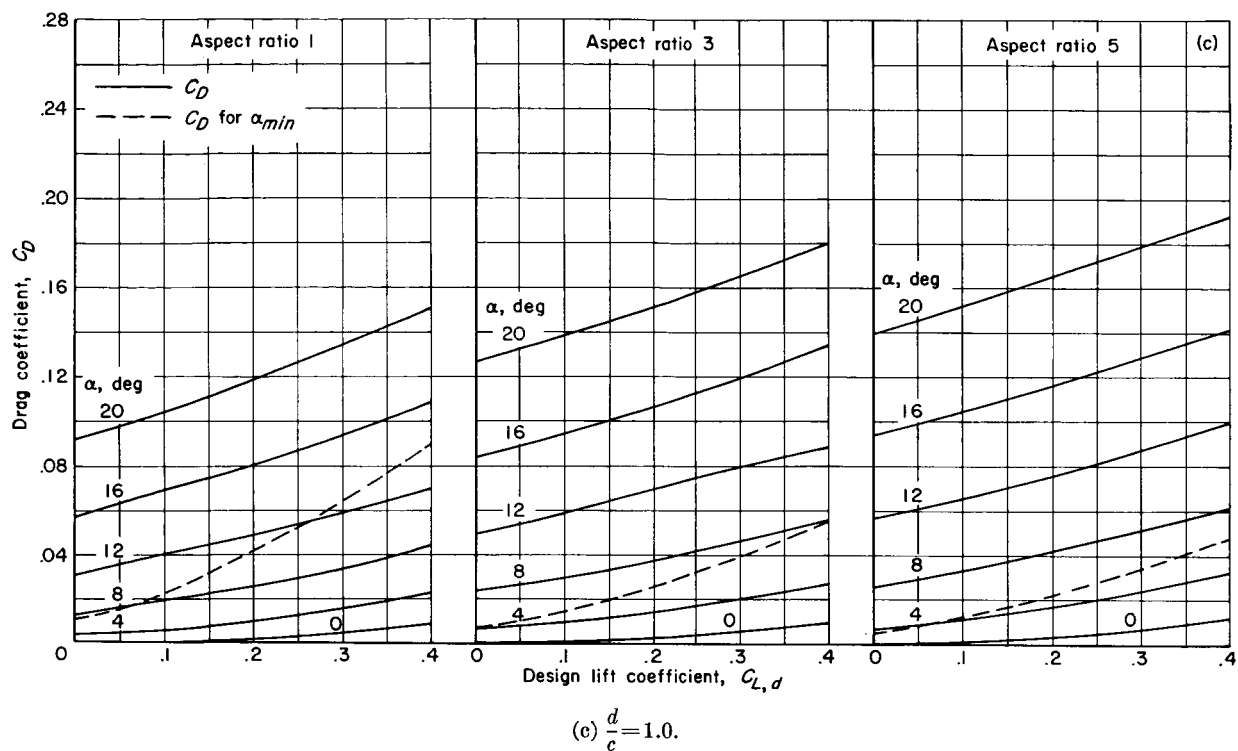


FIGURE 22.—Continued.

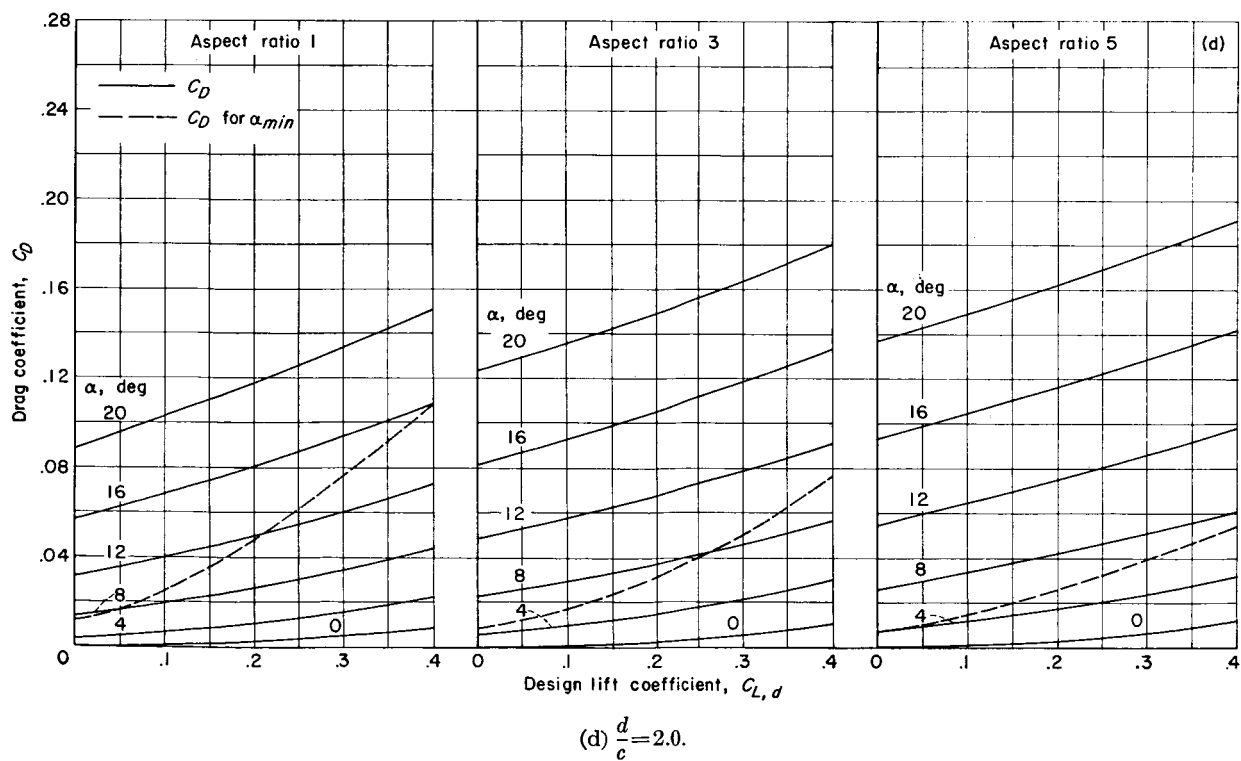


FIGURE 22.—Continued.

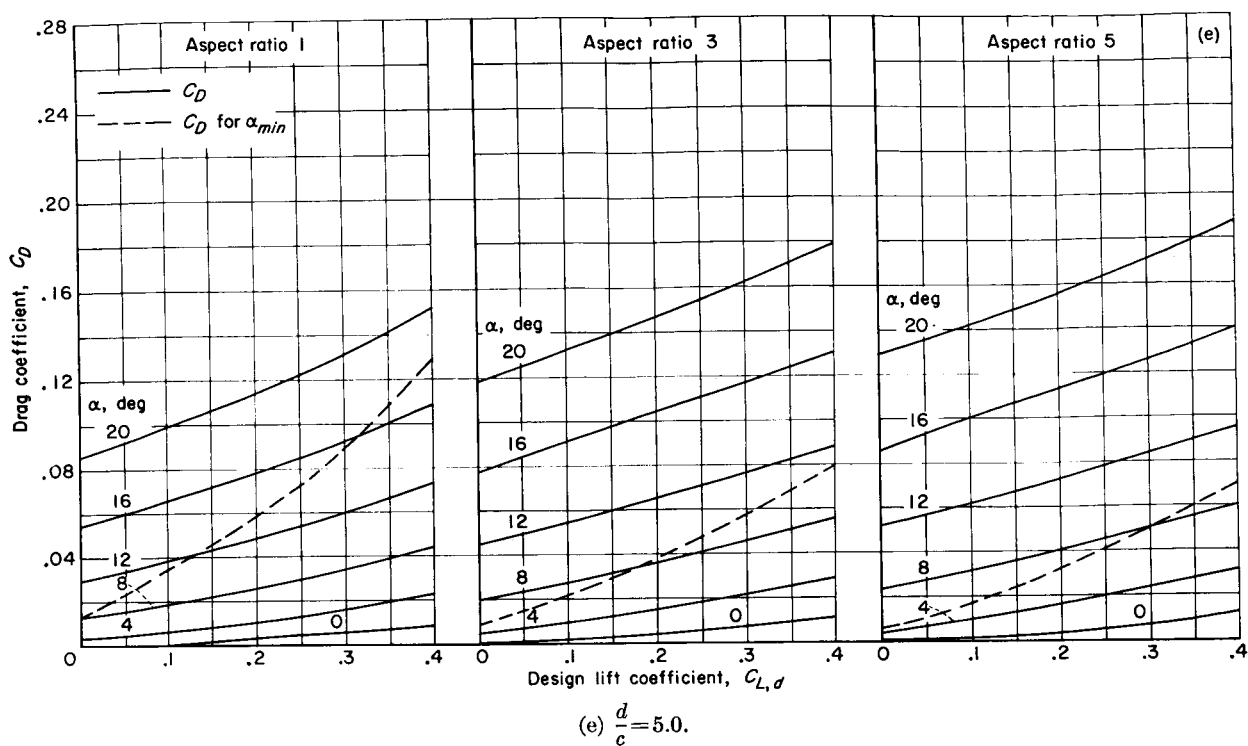
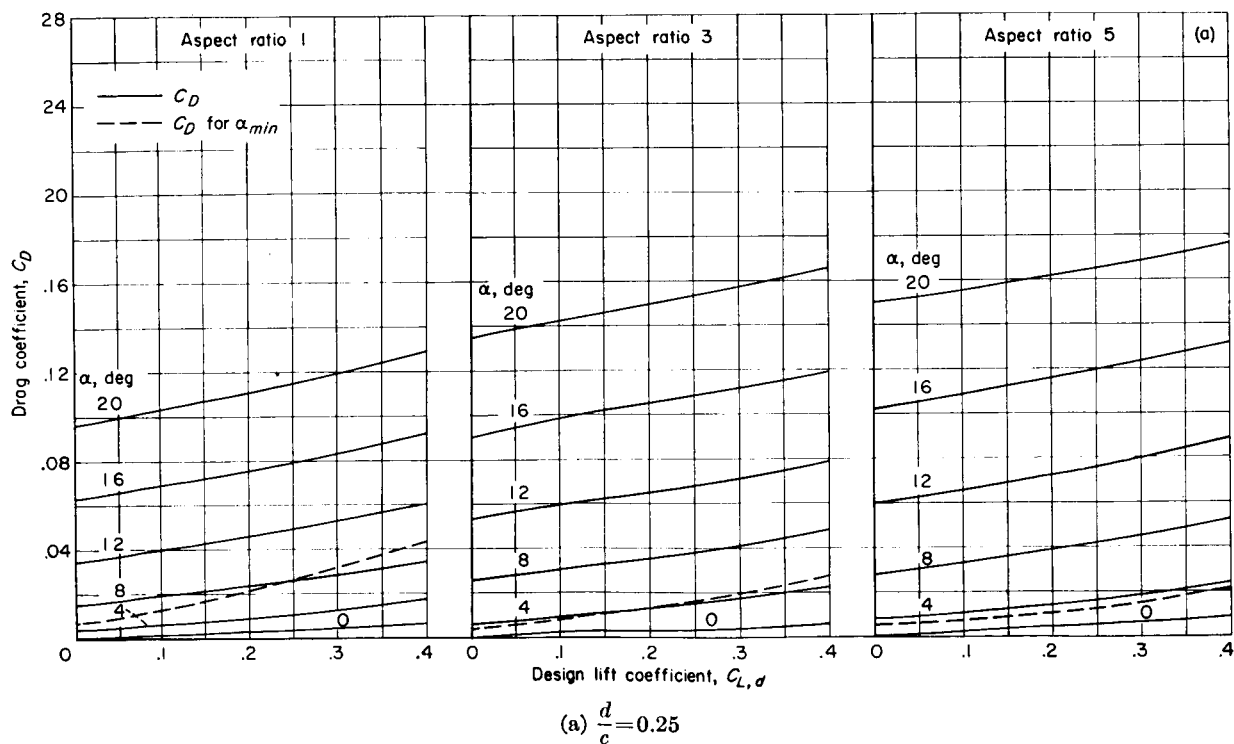
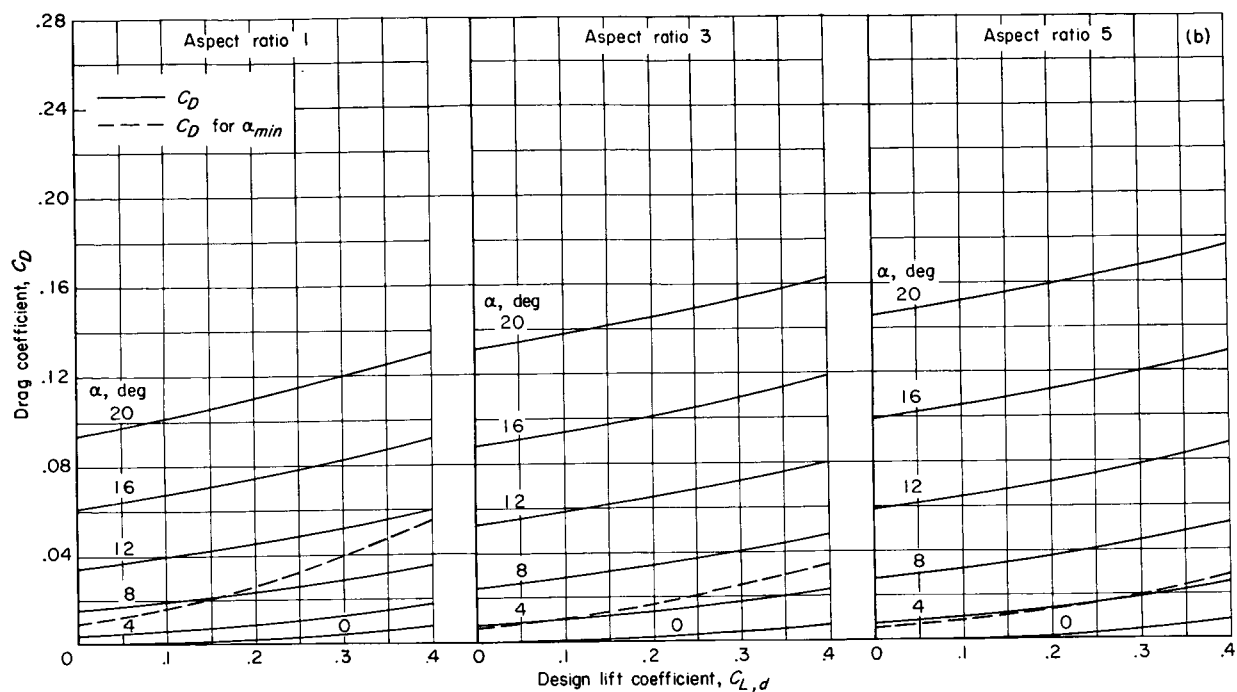


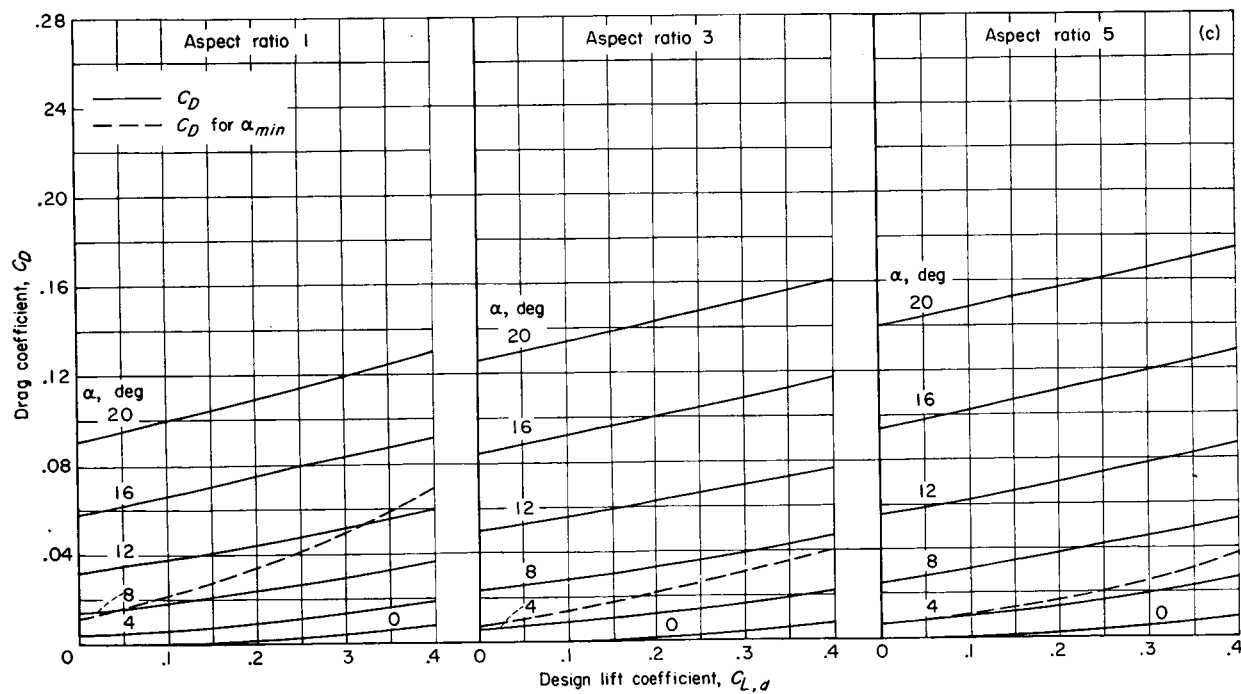
FIGURE 22.—Concluded.

FIGURE 23.—Calculated drag coefficient for three-term section including the minimum angle of attack for maximum L/D for $t/c = 0.03$ at $x/c = 0.2$.



(b) $\frac{d}{c} = 0.50$.

FIGURE 23.—Continued.



(c) $\frac{d}{c} = 1.0$.

FIGURE 23.—Continued.

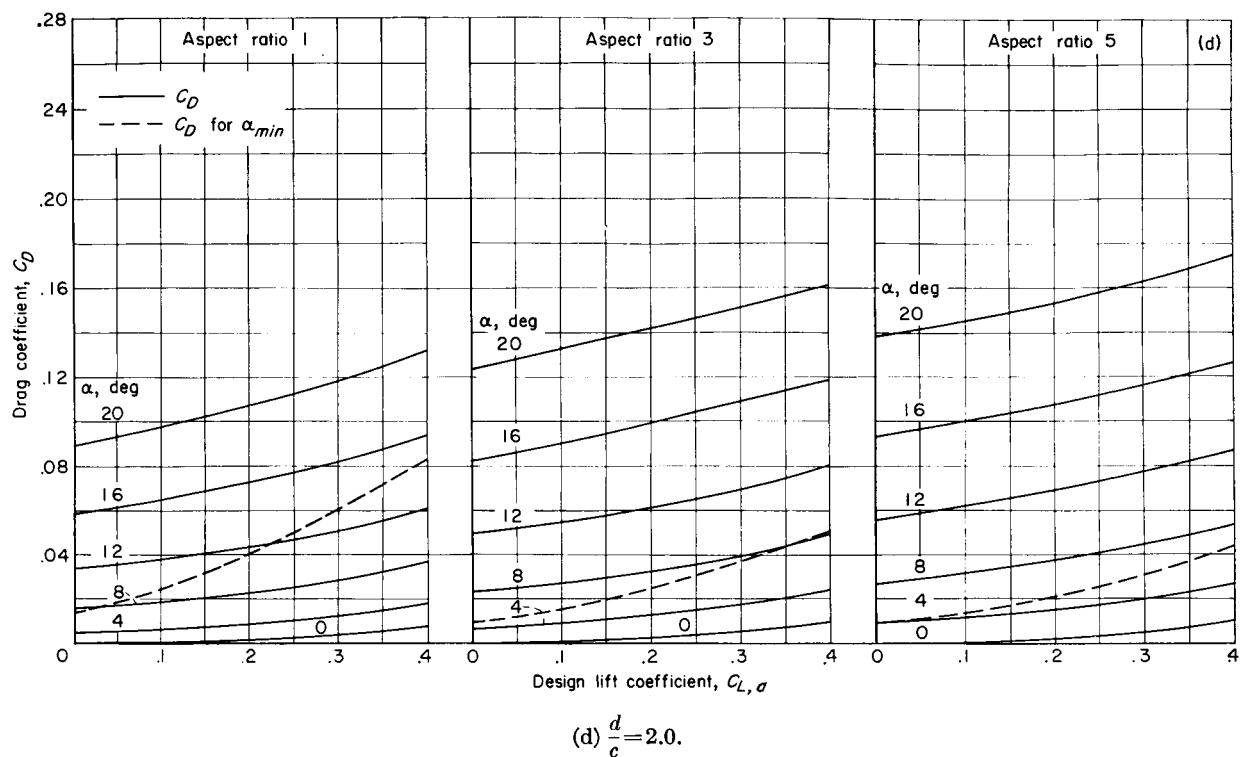


FIGURE 23.—Continued.

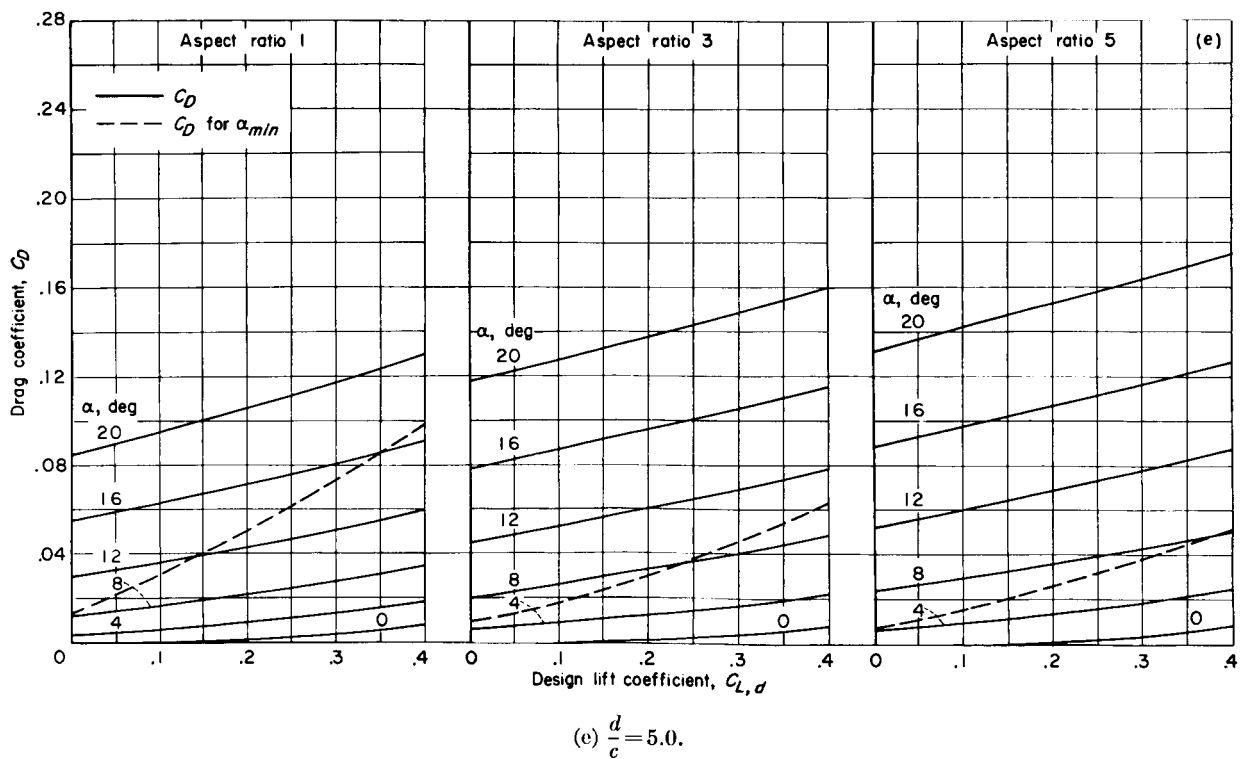


FIGURE 23.—Concluded.

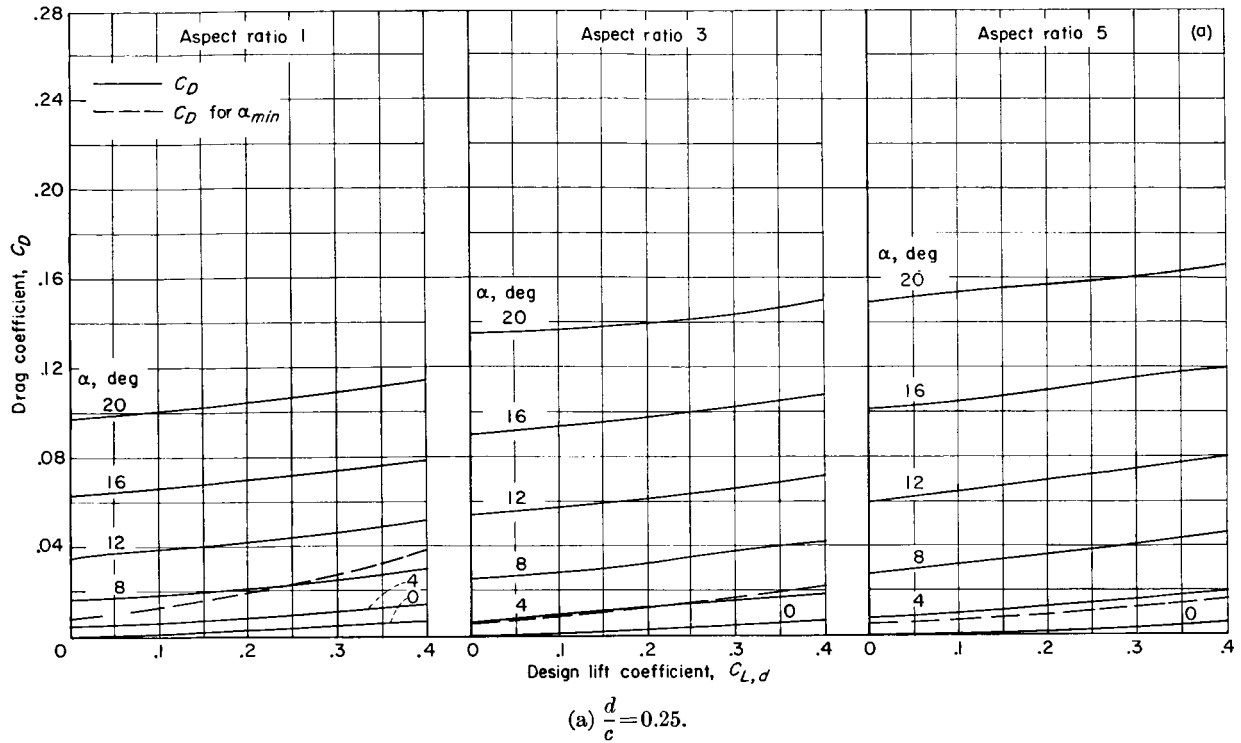


FIGURE 24.—Calculated drag coefficient for five-term section including the minimum angle of attack for maximum L/D for $t/c=0.03$ at $x/c=0.2$.

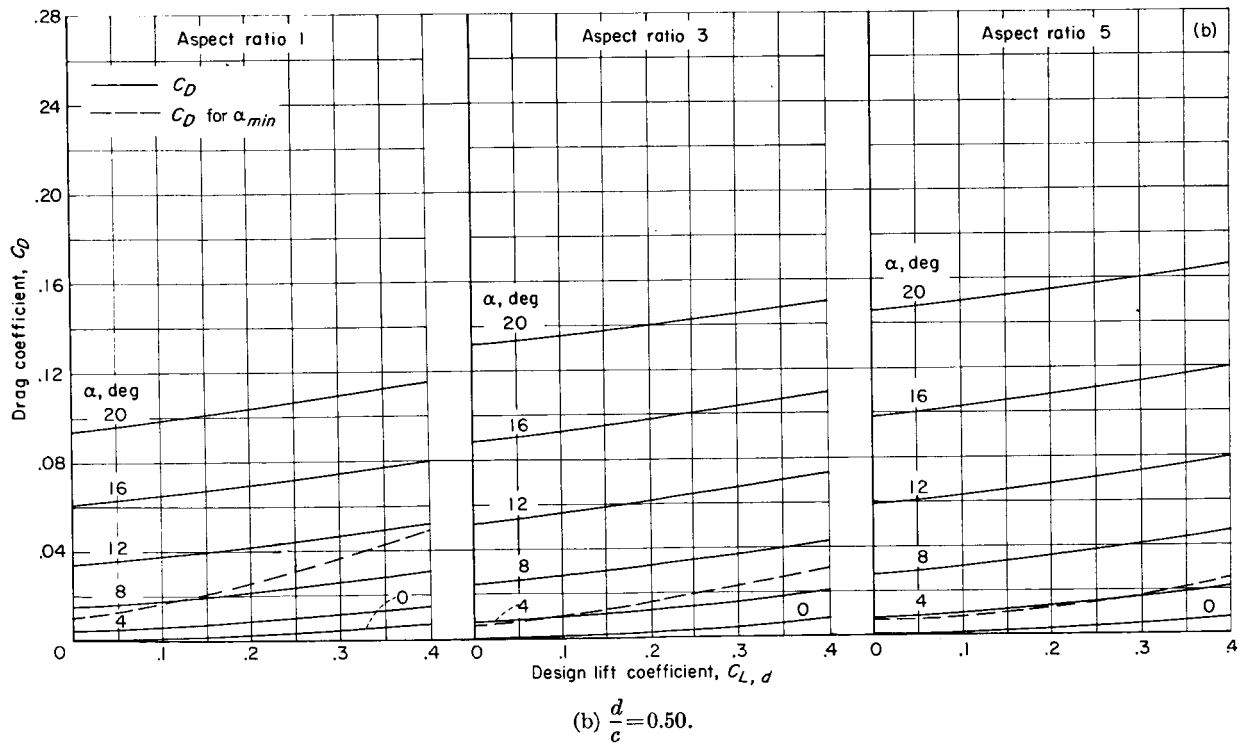


FIGURE 24.—Continued.

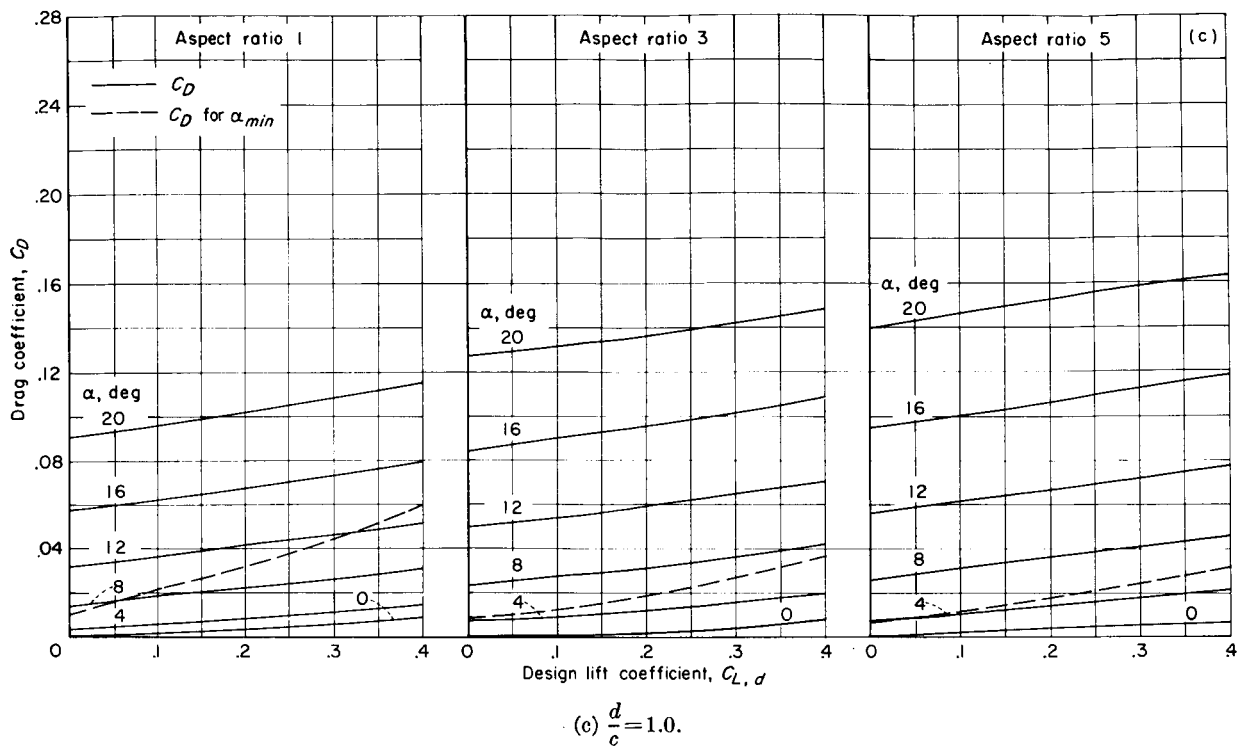


FIGURE 24.—Continued.

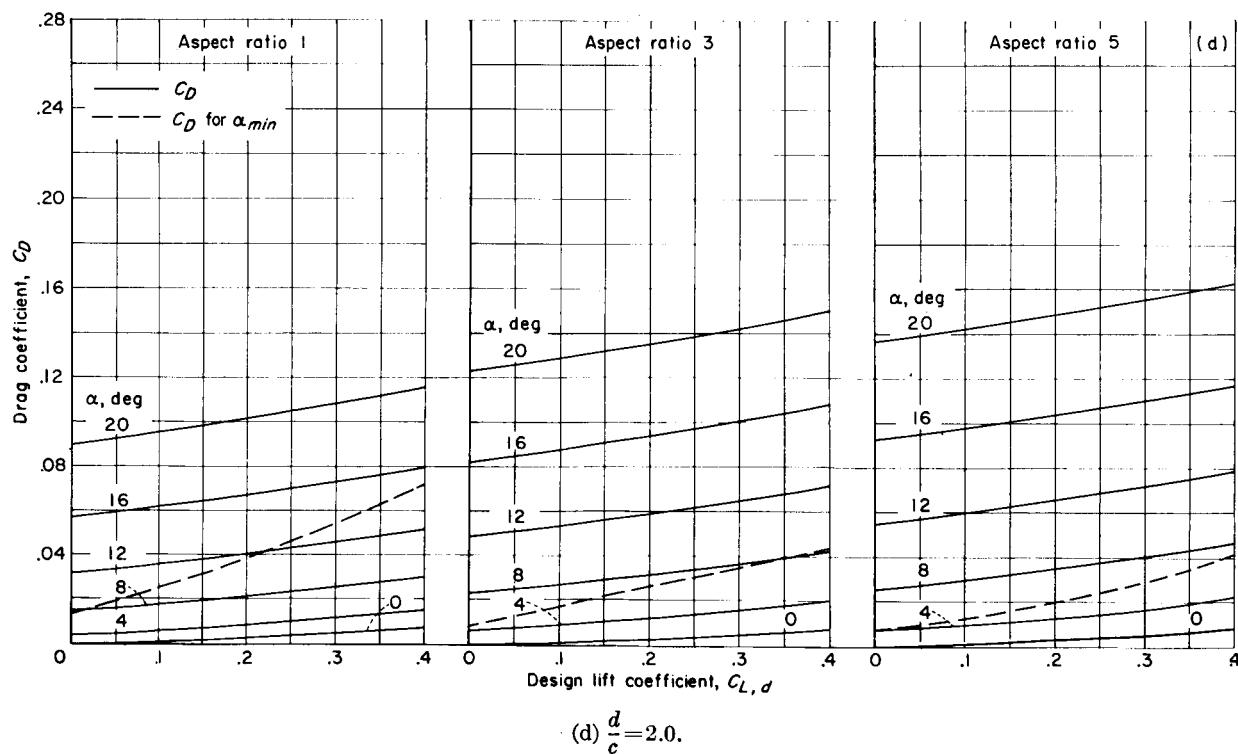


FIGURE 24.—Continued.

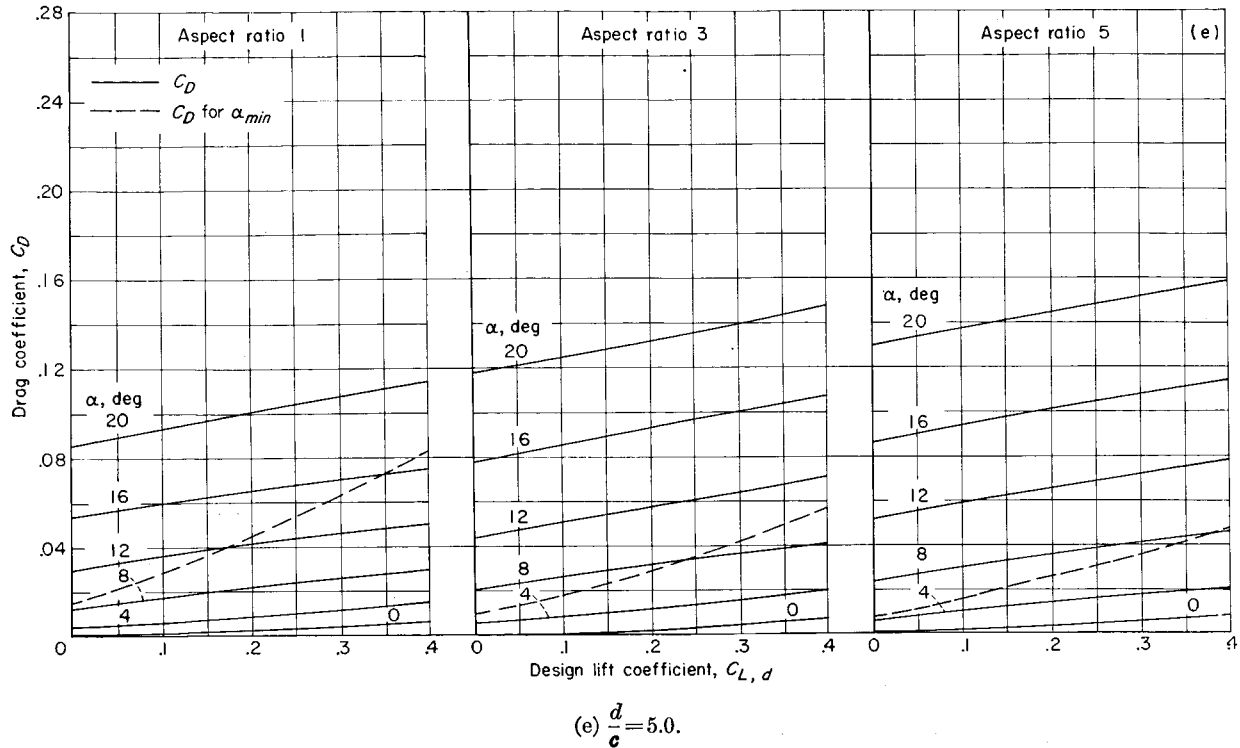


FIGURE 24.—Concluded.

LOCATION OF UPPER CAVITY STREAMLINE

The desirability of operating as near the design lift coefficient as possible is obvious from figure 5. Therefore, information on the minimum angle at which a hydrofoil with a finite thickness can operate with a cavity from the leading edge is needed. This angle can be determined by calculating the location of the upper cavity streamline. The minimum angle at which this upper cavity streamline clears the upper surface of a hydrofoil of finite thickness is the angle desired. An approximate solution for the location of the cavity streamline is derived in the following analysis.

TWO-DIMENSIONAL-THEORY ARBITRARY DEPTH

Green's exact solution for flat plate.—The equation of the upper cavity streamline for a two-dimensional flat plate may be obtained from the solution of Green (ref. 2) as

$$\frac{x}{\delta} = \frac{1}{\pi(b - \cos \alpha)} \left[\cos \alpha (t - 1) - (1 - b \cos \alpha) \log_e \frac{t - b}{b - 1} \right] \quad (114)$$

$$\frac{l}{\delta} = \frac{\sin \alpha}{(b - \cos \alpha)} \left[\sqrt{t^2 - 1} + b \log_e (t + \sqrt{t^2 - 1}) - \sqrt{b^2 - 1} \log_e \frac{bt - 1 + \sqrt{b^2 - 1} \sqrt{t^2 - 1}}{t - b} \right] \quad (115)$$

where x is distance from the leading edge along the plate, l is the perpendicular distance from the lower surface of the plate to the cavity streamline, δ is the spray thickness, and t is an arbitrary parameter. For a selected value of δ/c , b is known from equation (2b). Thus, l/c for a given x/c may be obtained by assigning appropriate values to t and using the equations

$$\left. \begin{aligned} \frac{x}{c} &= \frac{x}{\delta} \frac{\delta}{c} \\ \frac{l}{c} &= \frac{l}{\delta} \frac{\delta}{c} \end{aligned} \right\} \quad (116)$$

and equation (115). The cavity streamline computed in this manner for several angles of attack and spray thickness to chord ratios are presented in figure 25. The subscript A_0 on $(l/c)_{A_0}$ is to indicate cavity ordinate due to angle of attack.

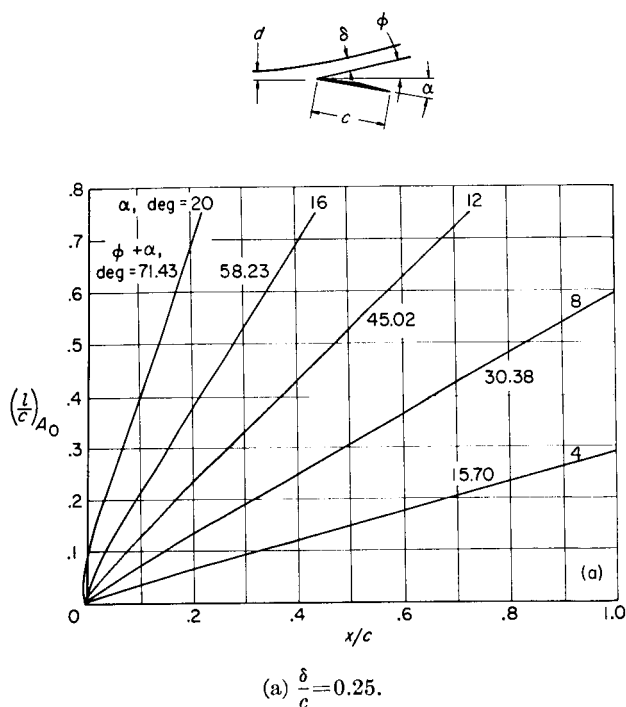


FIGURE 25.—Green's solution for the cavity upper streamline of a flat plate.

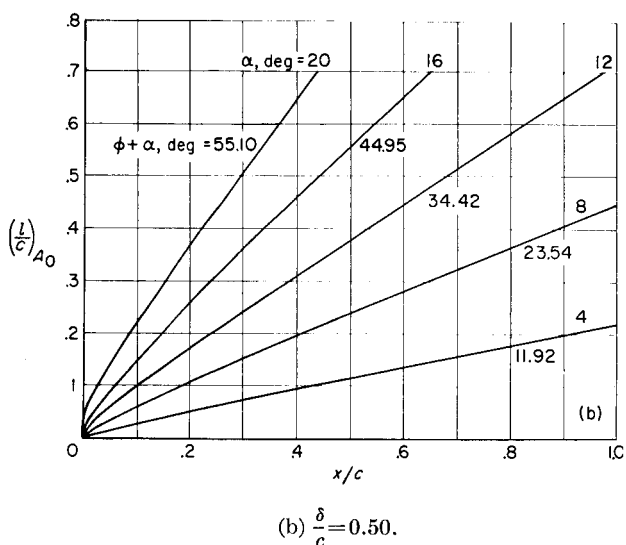


FIGURE 25.—Continued.

It can be seen in figure 25 that for finite depths the cavity streamline rapidly approaches a straight line. The angle between this asymptotic line and the plate is denoted as $\phi + \alpha$ and is given in

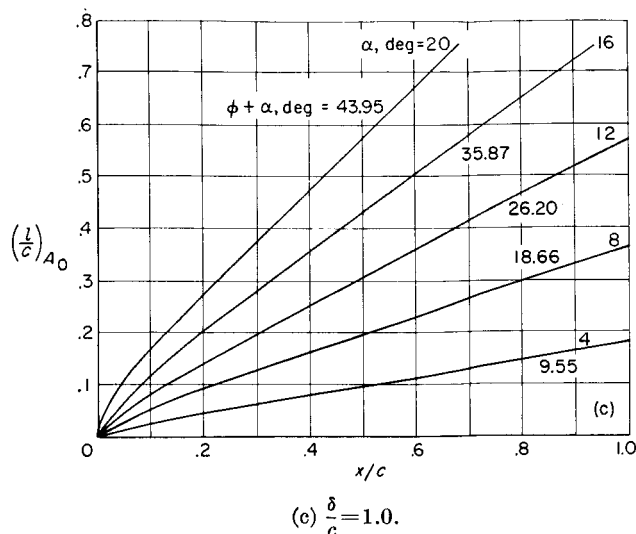


FIGURE 25.—Continued.

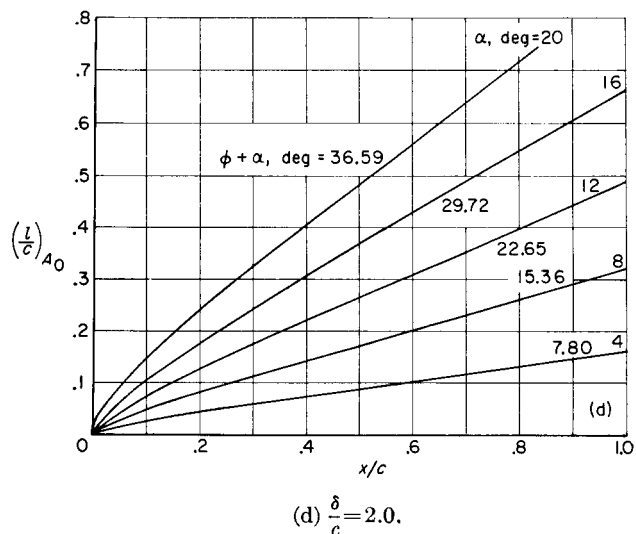


FIGURE 25.—Continued.

reference 2 as

$$\phi + \alpha = \frac{b \cos \alpha - 1}{b - \cos \alpha} \quad (117)$$

The magnitude of $\phi + \alpha$ is shown for each streamline in figure 25 and in figure 26 ϕ is plotted against δ/c for various angles of attack. In figure 25 it may be seen that the cavity ordinate varies almost linearly with angle of attack for angles less than about 8° . The value of $(l/c)_{A_0}/\alpha$ or more generally $(l/c)_{A_0}/A_0$ can be readily obtained and is given in figure 27. The value of $(l/c)_{A_0}/A_0$ for infinite depth is the same as the linearized

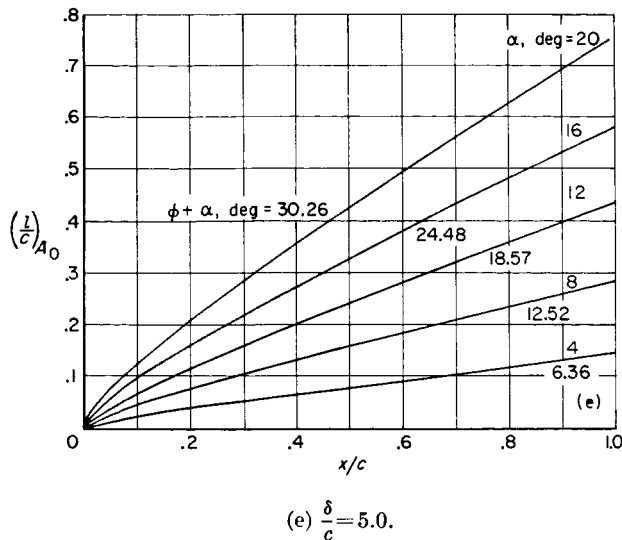


FIGURE 25.—Concluded.

result obtained in reference 1. Figure 27 shows that the cavity ordinates at a depth of about 0.5 chord are nearly twice as great as those obtained at infinite depth.

The linearized solution for cambered sections.— In order to determine the cavity ordinates for a cambered section, it is necessary to use the exact linearized solution previously discussed in the section entitled "Forces and Moments." The problem of obtaining the hydrofoil cavity ordinates is simple in principle. All that is required is to find the vertical-velocity perturbations $\bar{v}(-\bar{x}/c)$ ahead of the equivalent airfoil shown in figure 7. The value of \bar{v} is needed because from it the value of v on the hydrofoil-cavity streamline can be found. Since the linearized slope of the cavity streamline dy/dx is v/V , the shape of the cavity is determined.

The procedure for determining the vorticity distribution Ω on the airfoil is exactly the same as the first three steps given in the procedure for determining the linearized solution for the forces and moments. The value of $\bar{v}(\bar{x}/c)$ can be determined by integrating the increments of \bar{v} induced at a point $-\bar{x}/c$ due to the distributed vorticity Ω given by equations (10) and (11). Obviously, this integration becomes very complicated, particularly if there are many terms in $\sum A_n \sin n\theta$. The

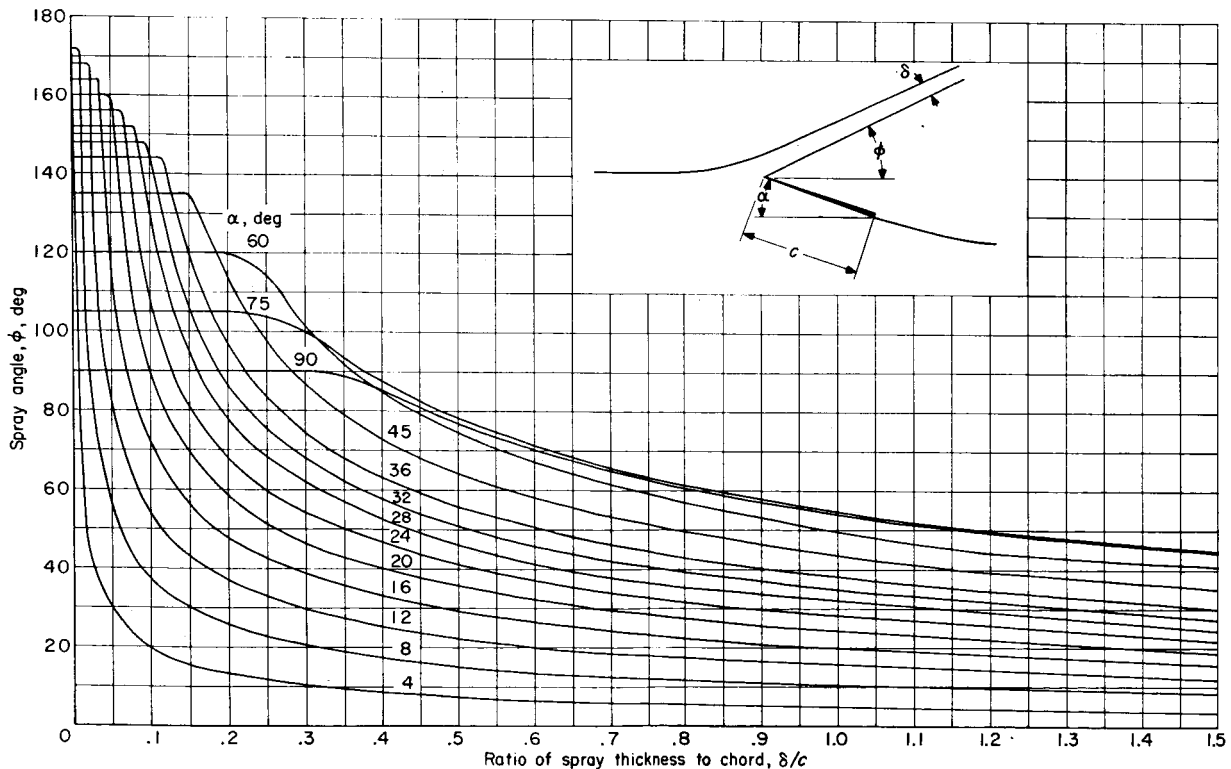


FIGURE 26.—Green's solution for the effect of spray thickness on the spray angle of a two-dimensional flat plate.

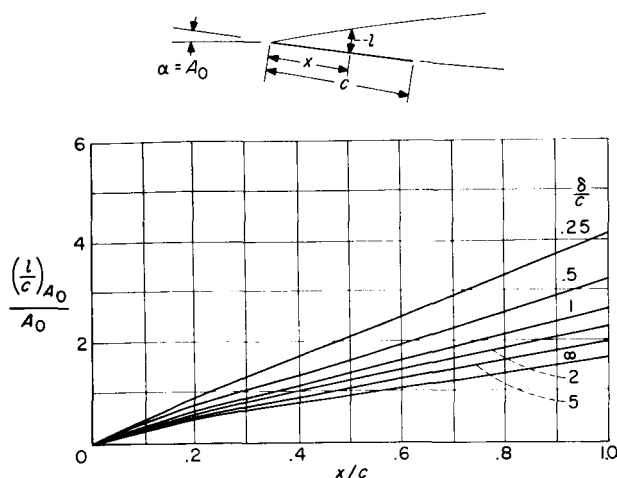


FIGURE 27.—The linearized solution for cavity ordinates due to angle of attack.

problem can be simplified, however, by dividing the velocity \bar{v} into two parts \bar{v}_{A_0} and \bar{v}_c , where \bar{v}_{A_0} is the component contributed by the first term $A_0 \cot \frac{\theta}{2}$, and \bar{v}_c , the component contributed by the camber terms $\sum A_n \sin n\theta$. Thus the final nondimensional cavity ordinates l/c will be broken down into two components $(l/c)_{A_0}$ and $(l/c)_c$ such that

$$(l/c)_{total} = (l/c)_{A_0} + (l/c)_c \quad (118)$$

The distance l is measured from the reference line of the section along a line normal to the reference line. There are two advantages to dividing the vorticity into its angle of attack and camber components. First, the value of $(l/c)_{A_0}$ is known from Green's solution and has been given in figure 25. The linearized version is shown in figure 27. Thus, half the work is completed if A_0 is known or can be determined.

It is now important to review the meaning of the coefficient A_0 . The angle of attack is measured from the orientation which makes $A_0 = 0$ when the depth is infinite. At this orientation and infinite depth

$$A_0' = -\frac{1}{\pi} \int_0^\pi \frac{d\bar{y}}{d\bar{x}} d\theta = 0 \quad (119)$$

and for angles of attack measured from this reference orientation $A_0 = \alpha$. However, if the angle of attack is measured from this reference line at finite depths, it is found that the value of $A_0' \neq 0$.

This result means that at finite depths there is an induced angle of attack A_0' due to the camber. The magnitude of A_0' is directly proportional to the slope of the hydrofoil and thus to $C_{L,a}$. The calculated value of $\frac{A_0'}{C_{L,a}}$ is given in figure 28 for the

four sections of interest for a range of depth-chord ratios. In order to obtain the value of $(l/c)_{A_0}$, one obtains A_0' from figure 28 and A_0 is obtained by adding α ; that is, $A_0 = \alpha + A_0'$. The value of $(l/c)_{A_0}$ is then obtained from figure 25 or 27.

The second advantage obtained by dividing the vorticity distribution into the A_0 and camber contributions is that the $\sum A_n \sin n\theta$ contribution usually has only small strength near the leading edge and, as an approximation, can be concentrated at one point. In fact, for low drag sections, it is desirable to distribute the vorticity as near the trailing edge as possible. Thus the velocity induced at points ahead of the airfoil due to the $\sum A_n \sin n\theta$ or camber contribution may be approximated by concentrating the entire camber vorticity at the center of pressure a as shown in figure 29. Figure 29 also illustrates the system used for computing the induced velocities forward of the airfoil. The value of the distance to the center of pressure in chords is given by \bar{C}_m/\bar{C}_L or

$$a = \frac{A_0 + A_1 - \frac{A_2}{2}}{A_0 + \frac{A_1}{2}} \quad (120)$$

The strength of the singular vortex can be obtained

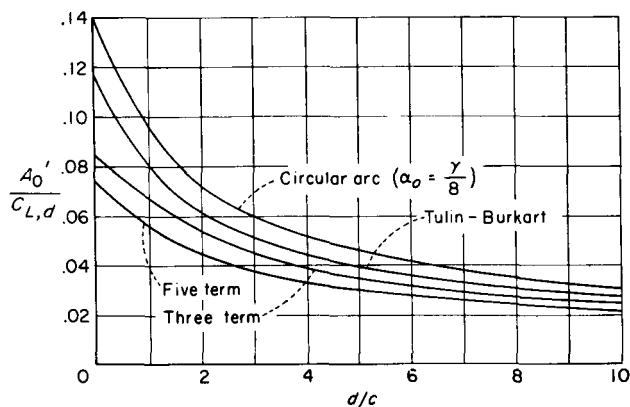
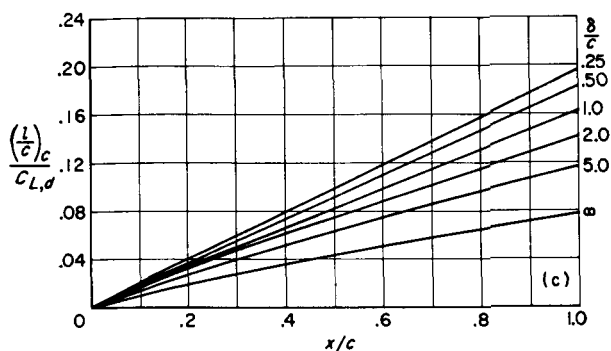
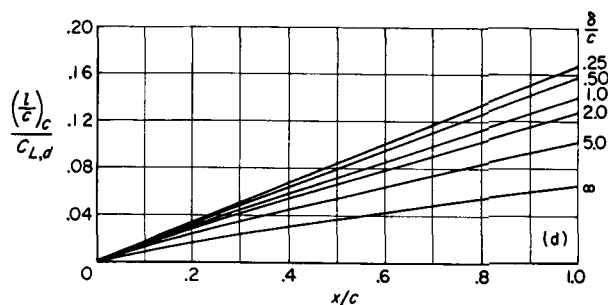


FIGURE 28.—The influence of depth of submersion on the angle of attack induced by camber.



(c) Three-term hydrofoil.

FIGURE 30.—Continued.

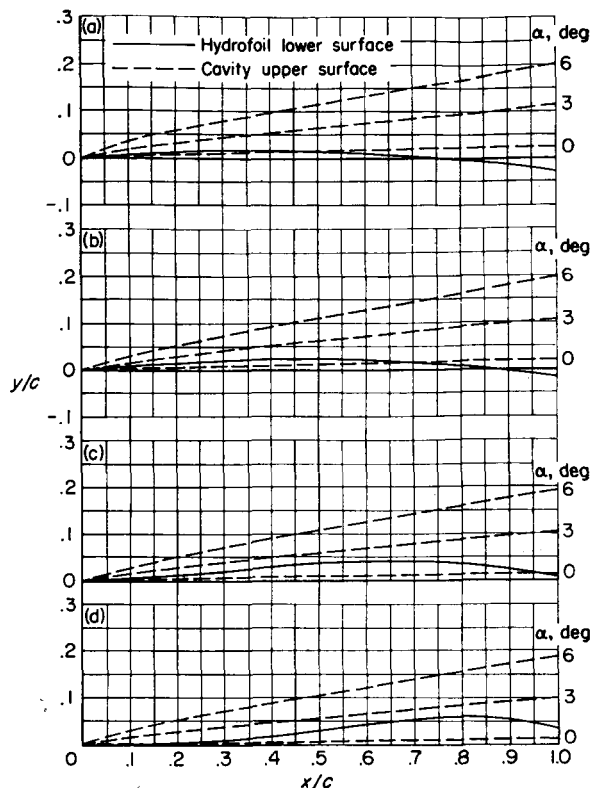


(d) Five-term hydrofoil.

FIGURE 30.—Concluded.

tabulated coordinates of reference 16 were computed for the Tulin-Burkart section by considering the vorticity to be distributed as given by $\Sigma A_n \sin n\theta$ and performing the necessary complicated integration.

In figure 31 the theoretical two-dimensional cavity shape for the low-drag hydrofoils operating at infinite depth is shown for the particular value of $C_{L,d}=0.2$. Also shown in figure 31 is the lower surface of each design for the value of $C_{L,d}=0.2$. An interesting point (first noted in ref. 16) is revealed in figure 31. The calculated cavity shape at the design angle of attack falls beneath the lower surface of the configuration. This result was not expected for these low-drag hydrofoils because the camber was selected to have positive pressure everywhere on the lower surface. It is believed that the disagreement is due to the inability of the linear theory to predict accurately the pressure distribution when the airfoil vorticity is not in reality distributed along the \bar{X} -axis. However, the shape of the cavity as determined from the



(a) Circular-arc section.
 (b) Tulin-Burkart section.
 (c) Three-term section.
 (d) Five-term section.

FIGURE 31.—Location of cavity upper surface for low drag supercavitating hydrofoils. $C_{L,d}=0.2$; $d/c = \infty$.

linear theory is much less sensitive to the deviation of the true location of the vorticity from the \bar{X} -axis. That is, the distance from a point on the hydrofoil to a point on the negative \bar{X} -axis is approximated very well by only the \bar{x} -component of the distance. Thus, it is seen that the pressure distribution predicted by the linear theory will be more nearly correct when the hydrofoil is at an angle of attack and more symmetrically located about the \bar{X} -axis. It appears, then, that low-drag hydrofoils such as those derived in the present paper and reference 1 can never be operated at the design angle of attack for two reasons: (1) An upper surface cavity will not form even on an infinitely thin configuration and (2) some thickness must be provided for strength.

CORRECTION FOR FINITE ASPECT RATIO

Equations (122) and (123) show that the cavity ordinates are directly proportional to the circulation on the equivalent airfoil and thus the circulation of the hydrofoil. Therefore, if the hydrofoil circulation is reduced from its two-dimensional value by finite span, the cavity ordinates must also reduce. Another argument for this decrease in cavity ordinates is that, if the two-dimensional drag coefficient is reduced because of finite aspect ratio, the maximum cavity thickness must also decrease as pointed out in reference 17. It is now assumed that for finite aspect ratios the cavity ordinates will be reduced from the two-dimensional value in proportion to the reduction in $C_{L,1}$. This reduction occurs for two reasons, first because of the reduced angle α_i and because of the reduced lift-curve slope, $\frac{A}{A+1}m$. More specifically, if the cosine terms are assumed to be about equal to unity, the first term of equation (99) can be written as

$$C_{L,1} \approx \frac{A}{A+1} m_{\alpha+\alpha_c-\alpha_i}(\alpha-\alpha_i) + \frac{A}{A+1} m_{\alpha+\alpha_c-\alpha_i}\alpha_c \quad (125)$$

where the subscripts on m indicate the angle at which m is determined on figure 2. If α_c is broken into two components A_0' and α_c' , that is, $\alpha_c = A_0' + \alpha_c'$, equation (125) can be written as

$$C_{L,1} = \frac{A}{A+1} m_{\alpha+\alpha_c-\alpha_i}(\alpha+A_0'-\alpha_i) + \frac{A}{A+1} m_{\alpha+\alpha_c-\alpha_i}\alpha_c' \quad (126)$$

If $\alpha+A_0' = A_0$ the value of the cavity ordinates at infinite aspect ratio and angle $\alpha+A_0'-\alpha_i$ is

$$\left(\frac{l}{c}\right)_{total} = \left(\frac{l}{c}\right)_{A_0-\alpha_i} + \left(\frac{l}{c}\right)_c \quad (127)$$

where $\left(\frac{l}{c}\right)_{A_0-\alpha_i}$ is determined from the nonlinear solution of Green and $(l/c)_c$ from the linearized theory. Therefore, the effective lift-curve slope at infinite aspect ratio and angle $A_0-\alpha_i$ is $m_{A_0-\alpha_i}$ for the first term in equation (127) and $m_{\alpha=0}$ for the second term. Thus at finite aspect ratio the

corrected cavity ordinates are

$$\left(\frac{l}{c}\right)_{total} = \frac{\frac{A}{A+1} m_{\alpha+\alpha_c-\alpha_i}}{m_{A_0-\alpha_i}} \left(\frac{l}{c}\right)_{A_0-\alpha_i} + \frac{\frac{A}{A+1} m_{\alpha+\alpha_c-\alpha_i}}{m_{\alpha=0}} \left(\frac{l}{c}\right)_c \quad (128)$$

or

$$\left(\frac{l}{c}\right)_{total} = R_{A_0} \left(\frac{l}{c}\right)_{A_0-\alpha_i} + R_c \left(\frac{l}{c}\right)_c \quad (129)$$

where

$$R_{A_0} = \frac{A}{A+1} \frac{m_{\alpha+\alpha_c-\alpha_i}}{m_{A_0-\alpha_i}}$$

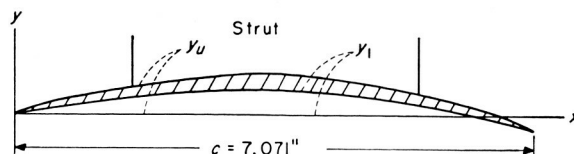
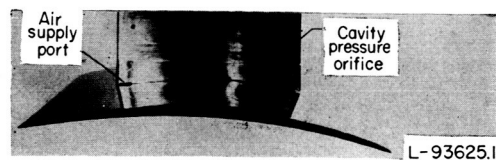
$$R_c = \frac{A}{A+1} \frac{m_{\alpha+\alpha_c-\alpha_i}}{m_{\alpha=0}}$$

The preceding analysis assumes that the induced angle α_i is constant over the span. Since α_i actually varies over the span, except for the case of elliptic loading, the cavity ordinates will also vary over the span. This effect can be included by using the appropriate spanwise distribution of α_i determined from finite-span airfoil theory. (See ref. 11.) Also the influence of the crossflow component of flow on the cavity ordinates has been assumed to be negligible. However, near the tips the cavity shape is largely determined by the crossflow. For example, at zero aspect ratio the cavity is entirely determined by crossflow. Thus, it seems that the true cavity shape is determined at the tips by the crossflow and at the center by the main flow; the cavity shape between is some transition between the two extremes.

EXPERIMENTAL INVESTIGATION

MODELS

Concurrent with the preceding theoretical investigation an experimental investigation was conducted. Two models of 7.071-inch chord were used in this experimental investigation. As shown in figure 32(a), the first had a lower surface conforming to the Tulin-Burkart low-drag configuration given by equation (14). A two-dimensional design lift coefficient of 0.392 corresponding to a value of 0.2 for the coefficient A_1 was selected. Since the foil is designed to



$$\frac{y_l}{c} = \frac{A_1}{2} \left[\frac{x}{c} + \frac{8}{3} \left(\frac{x}{c} \right)^{3/2} - 4 \left(\frac{x}{c} \right)^2 \right]$$

$$(a) \quad A_1 = 0.2$$

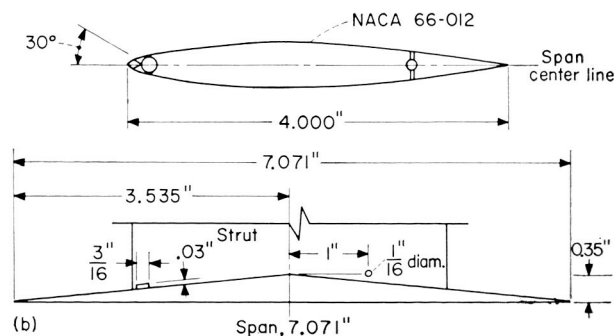
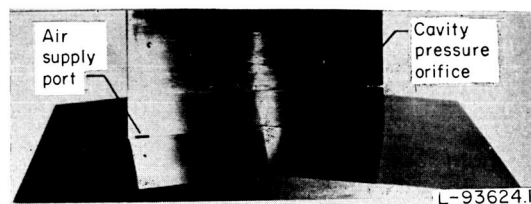
Coordinates, in.															
x	0	0.250	0.500	0.750	1.000	1.250	1.500	1.750	2.000	2.250	2.500	2.750	3.000	3.250	3.500
y_u	0	.092	.155	.207	.253	.292	.327	.363	.396	.426	.456	.483	.511	.536	.550
y_l	0	.037	.071	.108	.144	.177	.207	.234	.257	.277	.293	.305	.312	.315	.314
x	3.750	4.000	4.250	4.500	4.750	5.000	5.250	5.500	5.750	6.000	6.250	6.500	6.750	7.000	7.071
y_u	.536	.502	.467	.430	.390	.349	.302	.254	.206	.150	.084	.010	-.079	-.189	-.236
y_l	.308	.297	.282	.262	.237	.207	.172	.132	.088	.038	-.018	-.078	-.144	-.215	-.236

(a) Cambered model; Tulin-Burkart; $C_{L,a}=0.392$.

FIGURE 32.—Model configurations.

operate in a cavity, the shape of the upper surface is arbitrary as long as it does not interfere with the formation of the cavity from the leading edge. However, since the greatest advantage is to be obtained at small angles of attack and thus thin cavities, the thickness of the foil must be small. For the present cambered model the upper surface profile from the leading edge to midchord was arbitrarily chosen to conform with the theoretically determined free streamline for a two-dimensional flat plate at 5° incidence. The thickness of the portion aft of the midchord was made the image of the forward portion so that a symmetrical thickness distribution with a maximum thickness-chord ratio of 3.3 percent is obtained. Since the center of pressure of the Tulin-Burkart hydrofoil is located near the midchord, this symmetrical section minimizes the torsional moment on the foil and results in less twist than would be experienced by a non-symmetrical section.

The second model was of triangular cross section with a flat bottom as shown in figure 32(b).



(b) Flat-plate model.

FIGURE 32.—Concluded.

The maximum thickness was 5 percent of the chord.

Such thin sections lead to structural limitations on the aspect ratio when supported by a single strut at midspan. Since an aspect ratio of 1 is about the most desirable from the structural standpoint and also represents the accepted dividing line between hydrofoils and hydro-skis, both models were made with a square plan form.

The strut, which can also be seen in figure 32(b), had a NACA 66₁-012 airfoil section. The strut was mounted perpendicular to the bottom of the flat plate and perpendicular to the X -axis of the cambered surface. The intersection of the strut and upper surface was without fillets. Both the hydrofoils and the strut were made of stainless steel and were polished to a smooth finish.

APPARATUS AND PROCEDURE

Tests were made with the Langley tank no. 2 carriage and existing strain-gage balances which independently measure the lift, drag, and pitching moment. Figure 33 shows a view of the test setup with the cambered hydrofoil and the balance attached to the carriage. The positive directions of forces, angles, and moments used in presenting

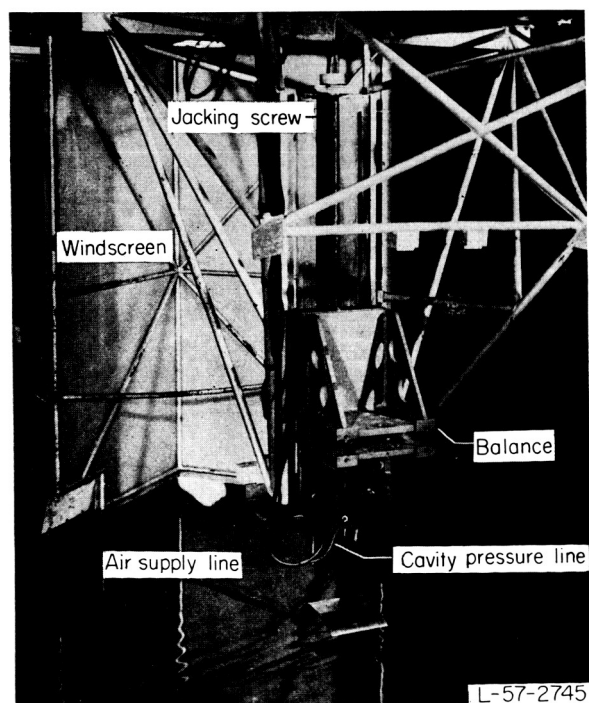


FIGURE 33.—Test set-up showing cambered hydrofoil and balance attached to towing carriage. Aspect ratio, 1.0.

the force data are shown in figure 34.

The force and moment measurements were made at constant speeds for fixed angles of attack and depths of submersion. The depth of submersion is defined as the distance from the undisturbed water surface to the leading edge of the model.

Ventilated or zero-cavitation-number tests were made with both models at a depth of submersion of 0.5 inch over a range of angle of attack from 6° to 20° for the flat plate and 8° to 20° for the cambered foil. Two methods of obtaining ventilated flow at this 0.5-inch depth were used: normal ventilation through the trailing vortices as described in reference 5, and injection of air through the port near the strut leading edge. (See fig. 30.) This air was supplied at a rate of 0.012 pound per second and was cut off after ventilation was established. Both models were also investigated at a depth of submersion of 0 inches at $\alpha=4^\circ$ for the flat plate, and $\alpha=6^\circ$, 8° , and 10° for the cambered surface. At angles of attack of 16° and 20° for the flat surface, forces were also measured over a range of depth of submersion for which ventilation could be obtained ($d=0$ to 2 inches).

The thickness and location of the jet or spray leaving the leading edge of the flat plate were also measured at 16° and 20° for a range of d from 0 to 2 inches. A schematic drawing of the instrument used for measuring the spray thickness and direction is shown in figure 35. The stagnation tube was lowered through the spray during a test and the pressure and location of the tube center line was recorded on an oscillograph. Almost instantaneous response of the stagnation-tube—pressure-cell combination was obtained by completely filling the tube and connecting line with water. The point of entering and leaving the spray was obtained by comparing the location of the tube with the rise and fall of pressure as the tube passed through the spray. The vertical location of the tube was obtained from the output of the slide-wire circuit also shown in figure 35.

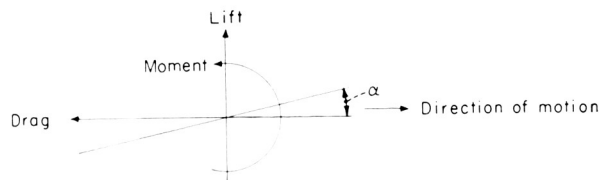


FIGURE 34.—System of axes.

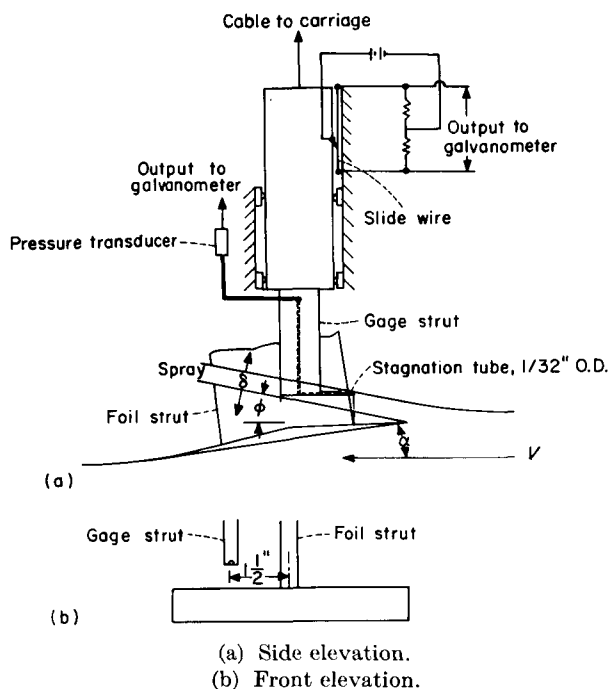


FIGURE 35.—Schematic drawing of spray thickness gage.

During a test the tube was passed through the spray several times and an average of the results was taken.

Tests of the finite-cavitation-number case were made at a depth of submersion of 6 inches (where vortex ventilation did not occur). Measurements of lift, drag, and moment were obtained for a range of velocities from 20 to 80 feet per second at angles of 18° and 20° (for which long trailing air or vapor cavities could be obtained). Data for air-filled cavities were obtained by introducing air from an external metered supply to the upper surface through the ports on the strut leading edge shown in figure 32. During these tests the pressure in the cavity formed was measured by a pressure cell connected to a $\frac{1}{16}$ -inch-diameter orifice located near the bottom of the strut so as to be within the cavity. (See fig. 32.) This measured pressure was used in computing the cavitation number for the cavity formed. The airflow rate was measured by an orifice-type flow meter. Airflow rates up to 0.012 pound per second were obtained with the test arrangement.

ACCURACY

The change in angle of attack due to structural deflection caused by the forces on the model was

obtained during the calibration of the balances and the test data were adjusted accordingly. The maximum correction necessary was only 0.1° . The estimated accuracy of the measurements is as follows:

Angle of attack, deg	± 0.1
Depth of submersion, in.	± 0.1
Speed, fps	± 0.2
Lift, lb	± 15
Drag, lb	± 7
Moment, ft-lb	± 6
Cavity pressure, lb/sq ft	± 10
Spray thickness, in.	± 0.05
Spray angle, deg	± 1.5

The forces and moments were converted to the usual aerodynamic coefficient form by using a measured value of the water density of 1.93 slugs per cubic foot. The kinematic viscosity measured during the tests was 1.70×10^{-5} pounds-second per square foot. Thus, for the range of velocities investigated, the Reynolds number based on chord ranged from 0.7×10^6 to 2.8×10^6 .

EXPERIMENTAL RESULTS AND DISCUSSION

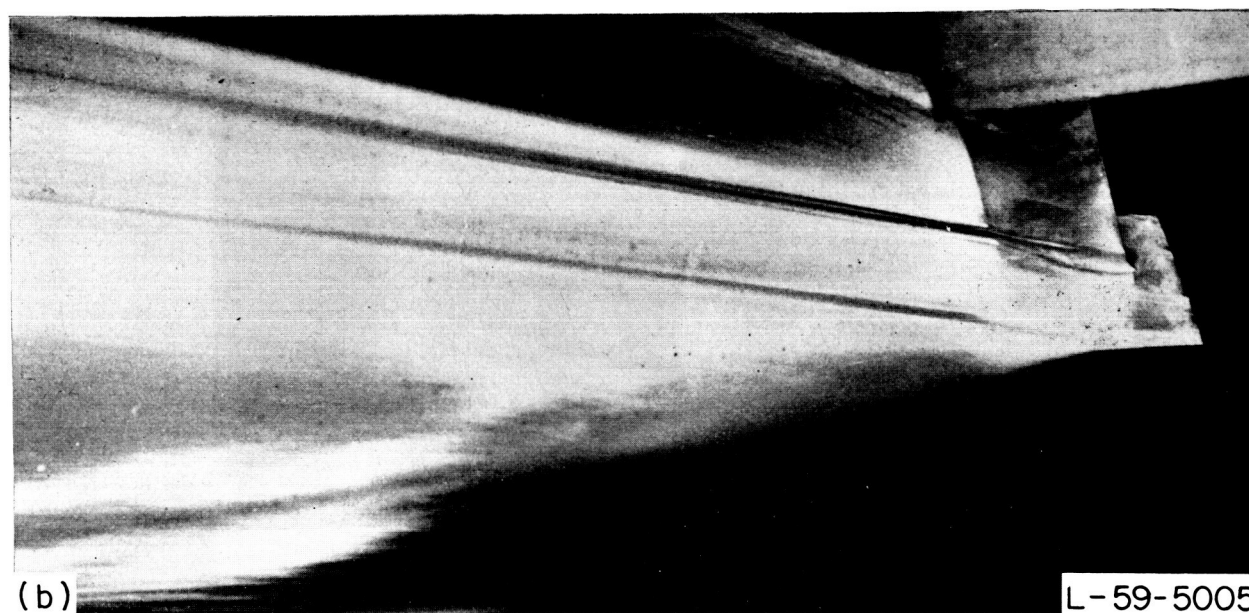
ZERO CAVITATION NUMBER

A typical photograph of the flat and cambered models operating in a ventilated condition near the free surface is shown in figure 36. Since only the zero cavitation number or fully ventilated flow condition was of interest, data are presented only for those conditions where ventilated flow could be obtained.

Basic force and moment results.—The basic data from the tests of the hydrofoils operating in a ventilated condition at a depth of submersion of 0.5 inch are presented in figures 37 and 38 as curves of lift, drag, and moment about the leading edge against speed for various angles of attack. Ventilated-flow data obtained at zero depth of submersion at 4° incidence for the flat plate and 6° , 8° , and 10° for the cambered surface are also included.

The basic ventilated-flow data obtained for the flat plate at depths of 0, 1.0, 1.5, and 2.0 inches for incidences of 16° and 20° are presented in figure 39.

Spray thickness and spray angle.—In the section on theory the need for determining the relationship between the leading-edge depth of submersion and the spray thickness for a flat plate was pointed out. These variables were measured for the flat plate at 16° and 20° over the range of



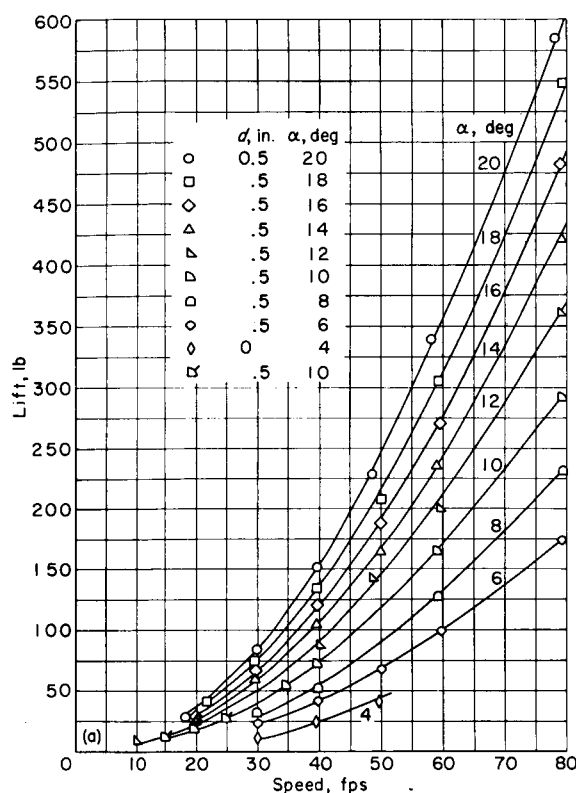
(a) Flat plate; $\alpha = 8^\circ$; $V = 40$ fps.

(b) Cambered model; Tulin-Burkart; $C_{L,d} = 0.392$; $\alpha = 12^\circ$; $V = 80$ fps.

FIGURE 36.—View of flat and cambered models operating in a ventilated-flow condition at a depth-chord ratio of 0.071.

depth of submersion from 0 to 2 inches. The data are shown in figure 40. The spray-thickness measurements presented were obtained approximately 20 percent of the chord rearward of the leading edge. On one test, measurement of the spray thickness was also obtained at about the

midchord and the results were in agreement with those obtained at the 20-percent location. Therefore, for the range of depths investigated, the spray thickness measured is comparable to the theoretical value infinitely rearward of the foil. It may be noted in figure 40 that the spray thickness is

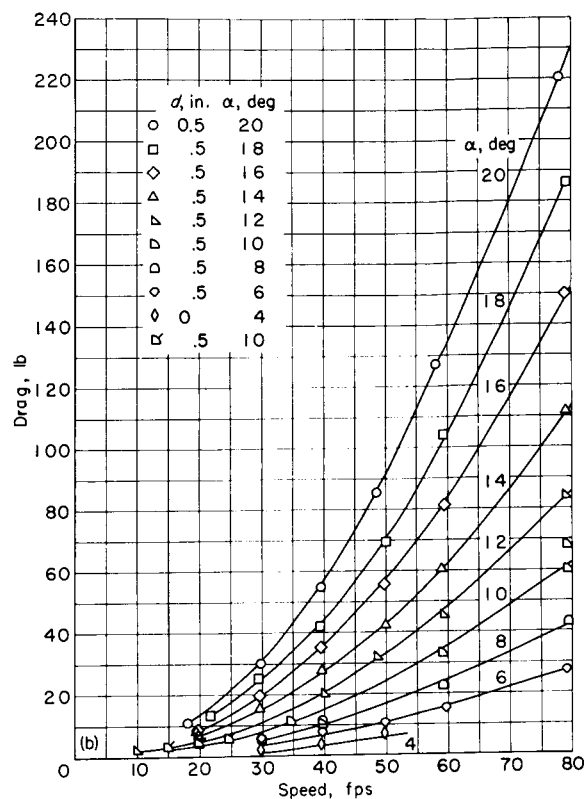


(a) Lift.

FIGURE 37.—Characteristics of the flat lifting surface operating in a ventilated condition.

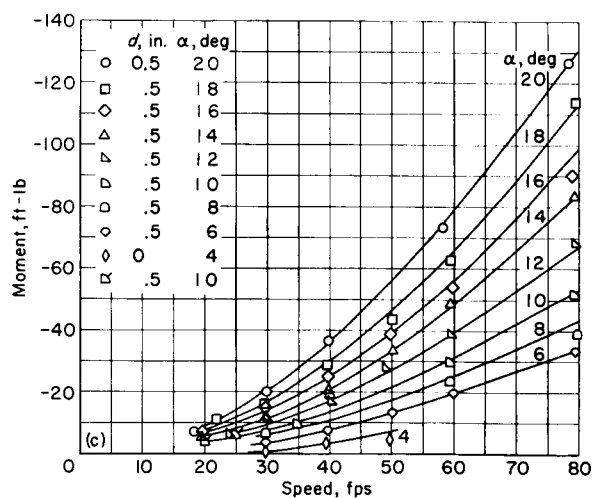
greater than the leading-edge depth of submersion, and the magnitude of the ratio increases with either increase in angle of attack or decrease in depth of submersion. Also shown in figure 40 are the theoretical relationships between δ/c and d/c for the two-dimensional 0° and 90° cases previously discussed. It may be noted that the trends of the experimental and theoretical curves are parallel.

In foregoing sections it has been pointed out that the relationship between leading-edge depth of submersion and spray thickness is influenced by the force of gravity and thus cannot be obtained from Green's analysis. Also the influence of aspect ratio has been shown to be important. The relationship for $\alpha=0^\circ$ and 90° has been determined but the manner in which intermediate angles of attack affect the result is not understood. The data shown in figure 40 combined with the end-point results previously established for $\alpha=0^\circ$ and 90° permit lines of constant d/c , at least for the aspect-ratio-1 condition, to be drawn on figure 2. The experimental data shown in figure 40 were



(b) Drag.

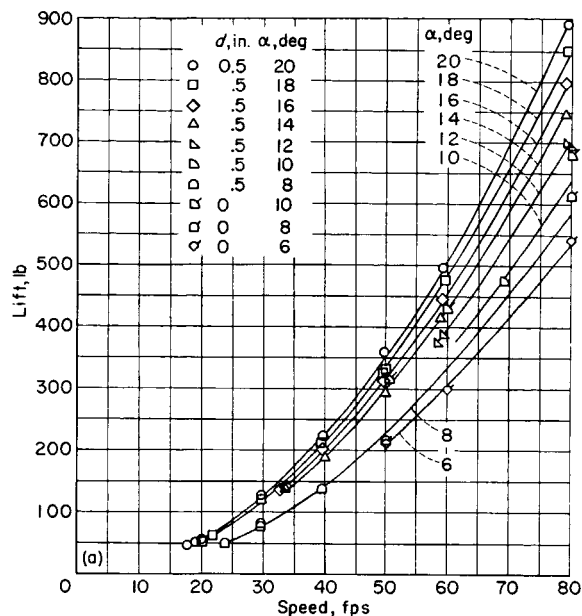
FIGURE 37.—Continued.



(c) Pitching moment about leading edge.

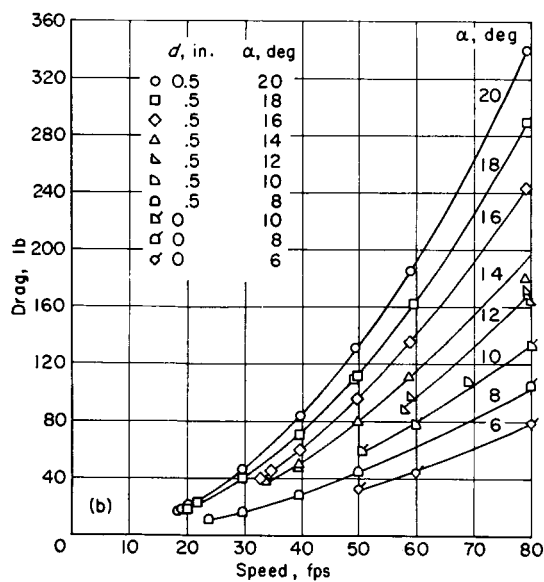
FIGURE 37.—Concluded.

plotted on figure 2 at their equivalent angle of attack $\alpha - \alpha_i$. This corresponds to equivalent angles of attack of approximately 12.3° for the 16° case and 15.9° for the 20° case for the range of d/c presented. For values of d/c greater than



(a) Lift.

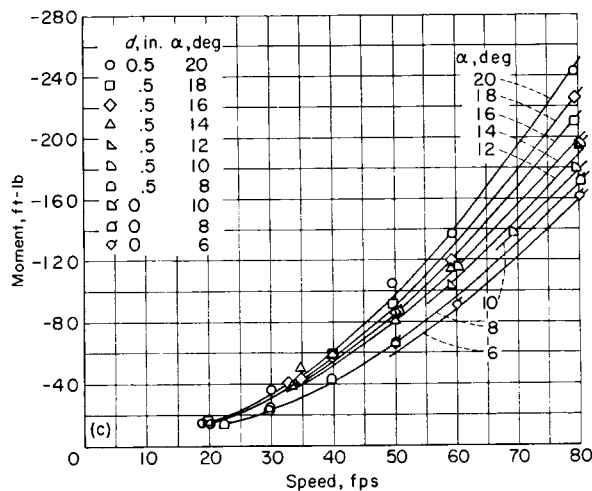
FIGURE 38.—Characteristics of the cambered lifting surface operating in a ventilated-flow condition.



(b) Drag.

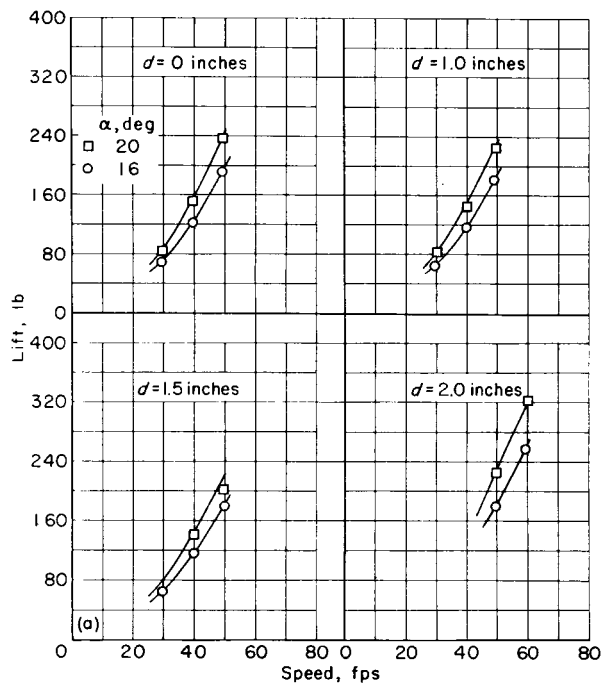
FIGURE 38.—Continued.

0.285, only the theoretical end points were available and parallel lines were faired in. Although these lines are accurate only for the aspect-ratio-1 condition, they are considered to be good approximations even for aspect ratios as high as 6. Such an approximation is reasonable because the asymptotic value of the stagnation line infinitely forward



(c) Pitching moment about leading edge.

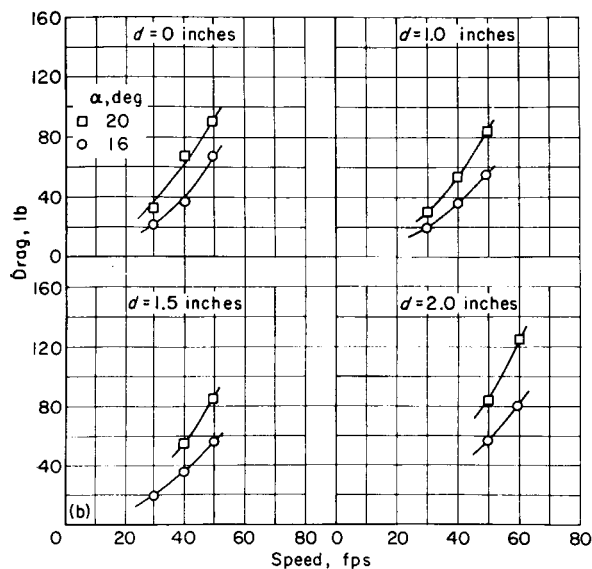
FIGURE 38.—Concluded.



(a) Lift.

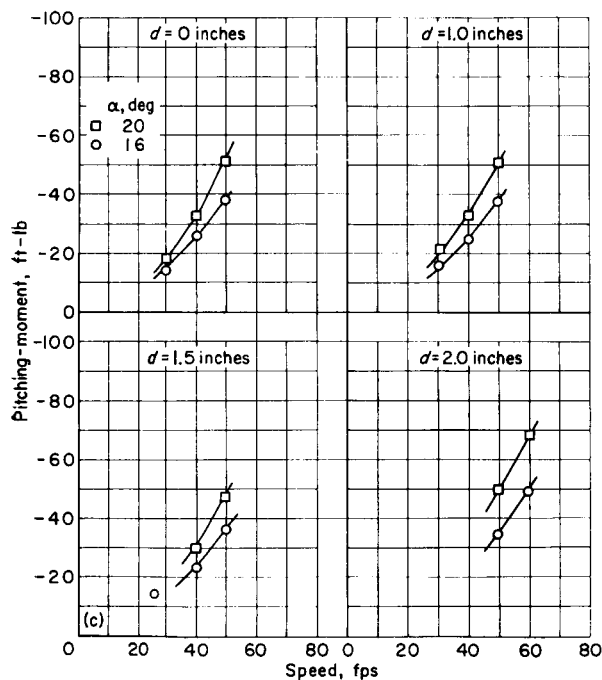
 FIGURE 39.—Characteristics of the flat plate operating in a ventilated-flow condition at $\alpha = 16^\circ$ and 20° for depths of submersion of 0, 1.0, 1.5, and 2.0 inches.

of a flat plate is only of the order of about 0.1 chord below the stagnation point for aspect ratios less than 6 and lift coefficients less than 0.5. It is obvious from figure 2 that for depths greater than 1 chord, the end points may be connected by any reasonable line (for example, a straight



(b) Drag.

FIGURE 39.—Continued.



(c) Pitching moment about leading edge.

FIGURE 39.—Concluded.

line) with very little loss in accuracy.

Figure 41 shows the effect of depth of submersion on the spray angle ϕ for the flat plate at 16° and 20°.

FINITE CAVITATION NUMBER

The finite-cavitation-number characteristics of

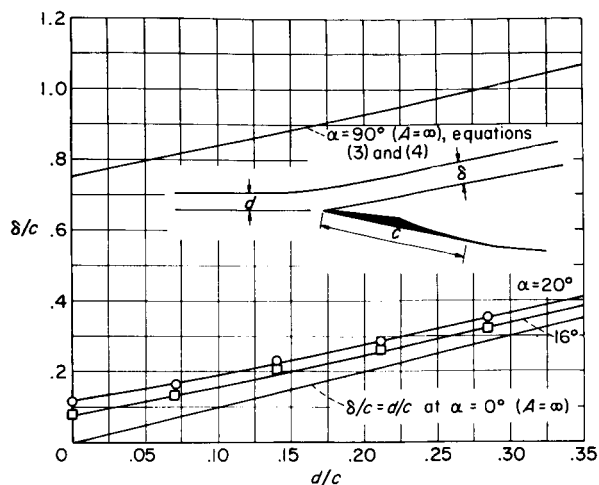


FIGURE 40.—Effect of depth of submersion on the flat lifting surface spray thickness. Aspect ratio, 1.0.

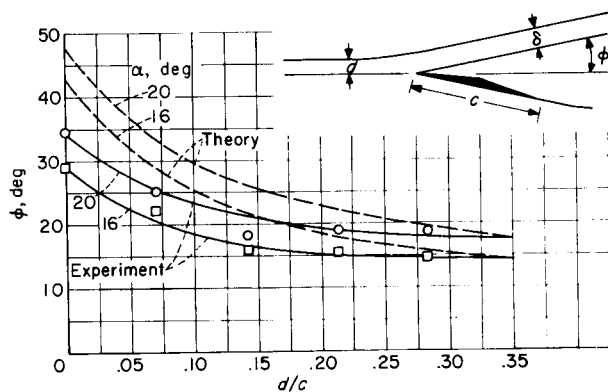


FIGURE 41.—Effect of depth of submersion on the flat lifting surface spray angle. Aspect ratio, 1.0.

the two models obtained at a 6-inch depth of submersion are shown in figure 42 for angles of attack of 18° and 20°. The solid data points are the lift coefficients obtained for vapor cavitation. The cavitation number corresponding to the condition tested was computed by using the water vapor pressure (at the test temperature) for the pressure within the cavity (that is $\sigma = \frac{p_o - p_v}{q}$). For cavitation numbers less than about 0.7, the vapor pressure was actually slightly lower than the measured cavity pressure. At cavitation numbers greater than 0.7, the measured pressure was usually considerably higher than the vapor pressure. However, since at the high cavitation numbers it could not be determined with certainty whether the cavity pressure orifice was within the cavity,

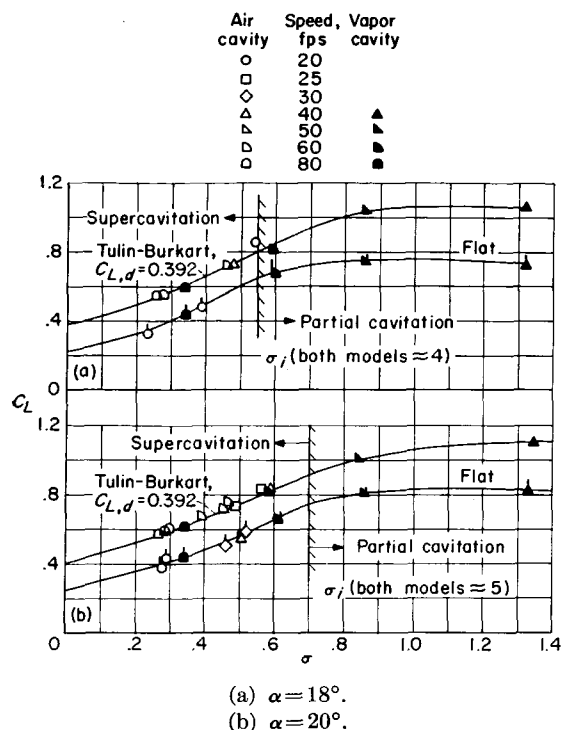


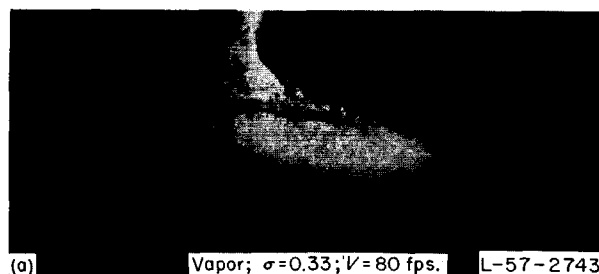
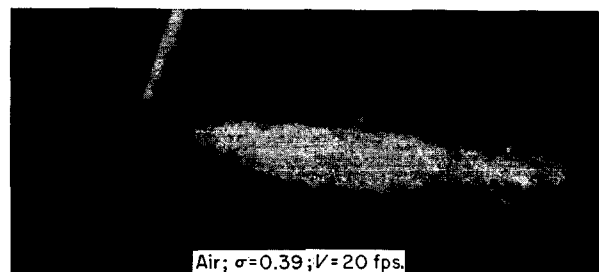
FIGURE 42.—Effect of cavitation number on lift coefficients of flat and cambered lifting surfaces. Depth of submersion, 6 inches; aspect ratio, 1.0. Symbols for flat-plate data are flagged.

the vapor pressure was used to compute all cavitation numbers. These high-cavitation-number points are denoted by the solid symbols. Also denoted in figure 42 are the approximate values of σ at inception σ_i and the point at which the cavity length exceeded the chord (supercavitation). These values are only estimates, since no effort was made to find the exact velocity at which these incidents occurred. Although the estimated values of σ_i are the same for both models, there may actually be some difference in the true points.

The open data points in figure 42 represent data obtained by introducing air to the upper surface of the model and establishing a cavity. The cavitation number for this condition was computed by using the measured value of the pressure within the cavity. In this case the cavity pressure orifice was always well within the cavity formed. In figure 42 the curves are extended to the computed value of C_L for $\sigma=0$ as obtained from equation (99).

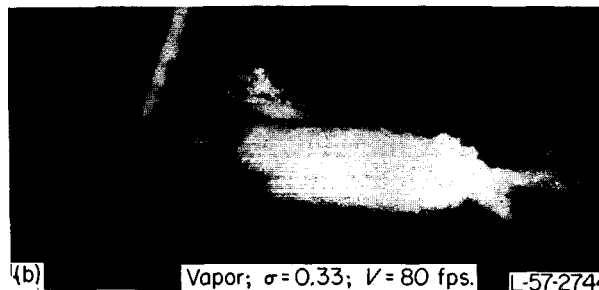
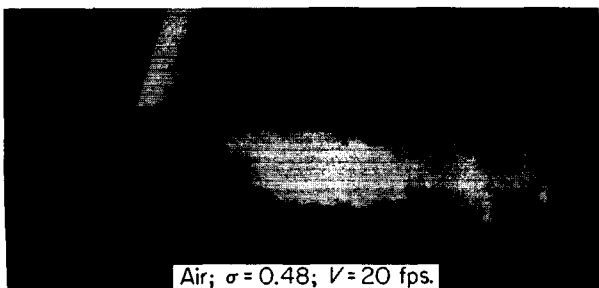
The agreement between the vapor- and air-cavity data confirms the use of the cavitation

number as the significant parameter for correlating the characteristics of cavity flow. The similarity of the air and vapor cavities at nearly equal cavitation number is shown in figure 43. This dependence on the cavitation number is to be



(a) Flat lifting surface.

FIGURE 43.—Comparison of air- and vapor-filled cavities for depth of submersion of 6 inches. $\alpha = 20^\circ$.



(b) Tulin-Burkart lifting surface; $C_{L,d} = 0.392$.

FIGURE 43.—Concluded.

expected because the forces on the body are influenced only by the streamline curvatures and thus the pressure within the cavity; the type of gas present should have only a secondary influence.

Satisfactory air cavities could not be established at angles less than about 18° . At low model speeds where the air could reach the separated region near the leading edge the cavity upper surface was greatly disturbed by the force of the air jets. At higher model velocities either the air could not reach far enough upstream to form a cavity or when a cavity was formed it did not cover the whole span. If a greater quantity of air is supplied it is believed that satisfactory results can be obtained at angles less than 18° .

The use of a dynamic model of a high-speed aircraft equipped with supercavitating hydrofoils will require simultaneous reproduction of both the full-scale cavitation and Froude numbers. Such an investigation is possible if an air-filled cavity with the proper cavitation number can be established on the model.

COMPARISON BETWEEN THEORY AND EXPERIMENT

FORCES AND MOMENTS

LIFT COEFFICIENT

The experimental data presented in the previous section revealed that all ventilated force and moment data in coefficient form were independent of speed in the range tested. (This independence was true in the present case because of the shallow depth of submersion and therefore $\sigma \approx 0$. At very large depths, σ will be greater than zero because p_o is greater than p_c even if the cavity is fully vented to the atmosphere. Therefore, at large depths, changes in velocity will affect the lift coefficient because these changes affect σ .) The data shown in figures 37(a) and 38(a) are plotted in figure 44 as lift coefficient against angle of attack for each of the models tested. A comparison of the lift coefficients of the two models shows an effective increase in angle of attack of the cambered model as predicted by the Tulin-Burkart theory. Also shown in figure 44 are the theoretical lift-coefficient curves obtained from equation (99). The theory is about 3 percent lower than the measured values.

The variation of lift coefficient with depth of

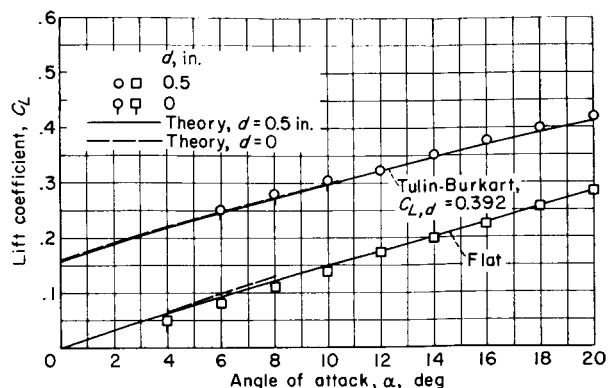


FIGURE 44.—Comparison of theoretical and experimental lift coefficients for the aspect-ratio-1 flat and Tulin-Burkart sections. $\sigma \approx 0$.

submersion of the flat-plate model at 16° and 20° incidence is shown in figure 45. Note the slight increase in lift coefficient as the hydrofoil nears the surface. Also shown in figure 45 is the theoretical variation of the lift with depth of submersion obtained from equation (99). The theory is in excellent agreement with the data and accurately predicts the increase in lift with a decrease in depth of submersion.

In reference 18 data obtained on the same two models used in the present experimental investigation are presented. These data were obtained with the model in a ventilated condition at speeds up to 185 fps. The measured lift coefficient is plotted against the depth-chord ratio for various

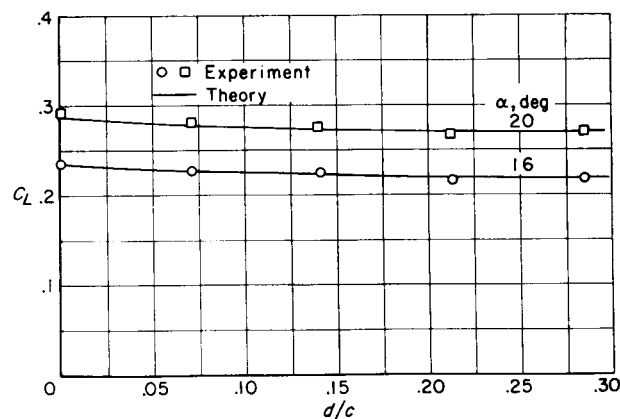


FIGURE 45.—Comparison of theoretical and experimental lift coefficients for the aspect-ratio-1 flat lifting surface as affected by depth of submersion. $\alpha = 16^\circ$ and 20° ; $\sigma \approx 0$.

angles of attack for the flat plate and Tulin-Burkart sections in figure 46. The solid lines in figure 46 are the theoretical values of the lift coefficient obtained from equation (99). Those points in the range $\sigma \approx 0.03$ denoted as partially vented are for cavitation numbers slightly greater than 0. The agreement between theory and experiment is generally good.

Two five-term supercavitating sections, one of aspect ratio 1 and one of aspect ratio 3, have also been tested in the ventilated condition near the free water surface in Langley tank no. 2. The aspect-ratio-1 hydrofoil had a design lift coefficient $C_{L,d}$ of 0.392. The value of $C_{L,d}$ for the aspect-ratio-3 hydrofoil was 0.196. The data obtained on these hydrofoils are presented in reference 19. In figure 47 the measured lift coefficients taken

from reference 19 are plotted against the depth-chord ratio for various angles of attack for the two five-term sections investigated. The solid lines in figure 47 are the theoretical values of the lift coefficient given by equation (99). The agreement between theory and experiment is again excellent except for the very shallow depths where the assumptions made in the derivation of the theory are invalid.

DRAG COEFFICIENT

In figure 48 the data of figures 37(b) and 38(b)

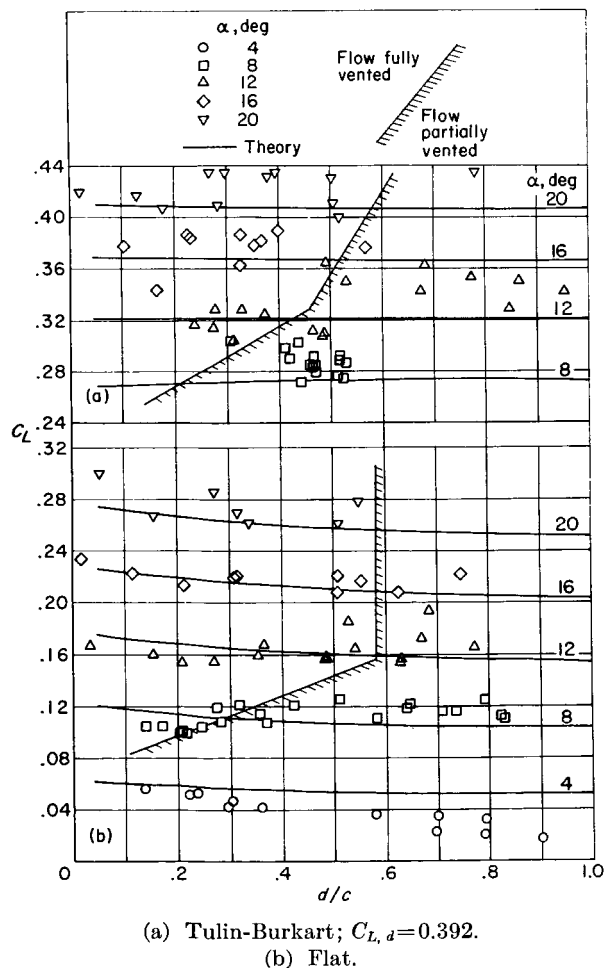
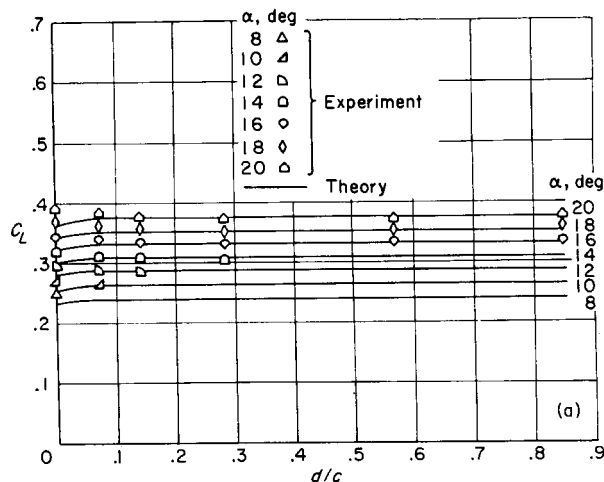
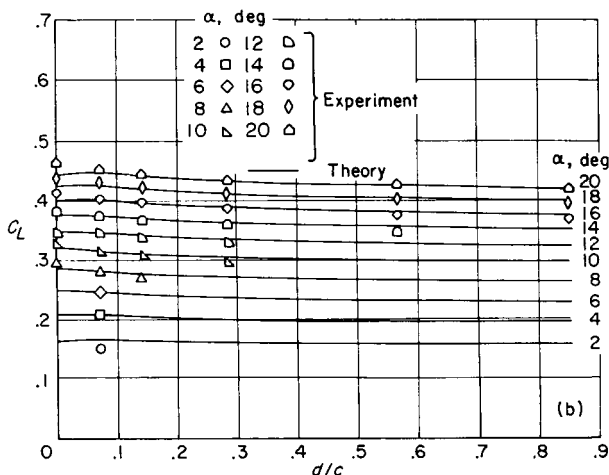


FIGURE 46.—Comparison of theoretical lift coefficients with experimental data reported in reference 19 on aspect-ratio-1 flat and Tulin-Burkart sections. $\sigma \approx 0$.



(a) Aspect-ratio-1 five-term hydrofoil; $C_{L,d} = 0.392$.

FIGURE 47.—Comparison of theoretical lift coefficients with experimental data reported in reference 19 on aspect-ratio-1 and -3 five-term sections. $\sigma \approx 0$.



(b) Aspect-ratio-3 five-term hydrofoil; $C_{L,d} = 0.196$.

FIGURE 47.—Concluded.

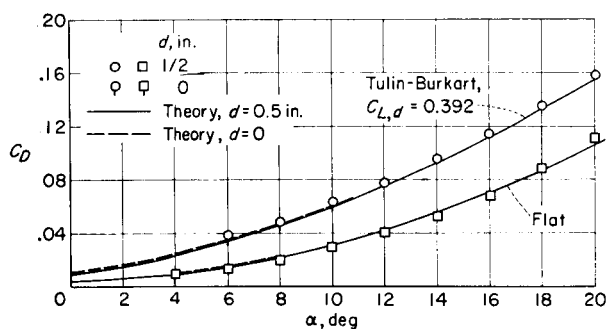


FIGURE 48.—Comparison of theoretical drag coefficients with experimental data obtained on aspect-ratio-1 flat and Tulin-Burkart sections. $\sigma \approx 0$.

in coefficient form are compared with theoretical values obtained from equation (100). The friction drag coefficient of one side of either of the models was calculated to be about 0.003. With the strut drag included, the total friction drag coefficient C_f based on the hydrofoil area was taken as 0.004. When this value of C_f is used in equation (100), the agreement between theory and experiment is good for both models.

In figure 49 the experimental lift-drag ratios obtained from the data of figures 37 and 38 are compared with theory. Again both experiment and theory include the skin-friction drag coefficient ($C_f = 0.004$). The agreement between theory and experiment is good for both models. The superiority of the cambered hydrofoil is clearly revealed in this figure. At a lift coefficient of 0.25 the L/D of the cambered foil is more than twice that of the flat plate.

Also included in figure 49 are data taken from reference 5 on a ventilated modified flat plate of aspect ratio 1. This modified plate had an elliptical leading edge and a tapered trailing edge. The importance of providing a sharp leading edge on hydrofoils designed for use in cavity flow is shown by comparing the L/D of this modified flat plate with the L/D of the sharp-leading-edge flat plate of the present investigation. The rounded leading edge of the modified plate is subjected to a net positive pressure which is not balanced by similar pressures on the afterportion of the plate. In addition, the lower surface of this plate presents an effective negative camber to the flow and thus does not develop as much lift as a truly flat surface. At small angles the form drag of the rounded leading edge is of the same order of magnitude as

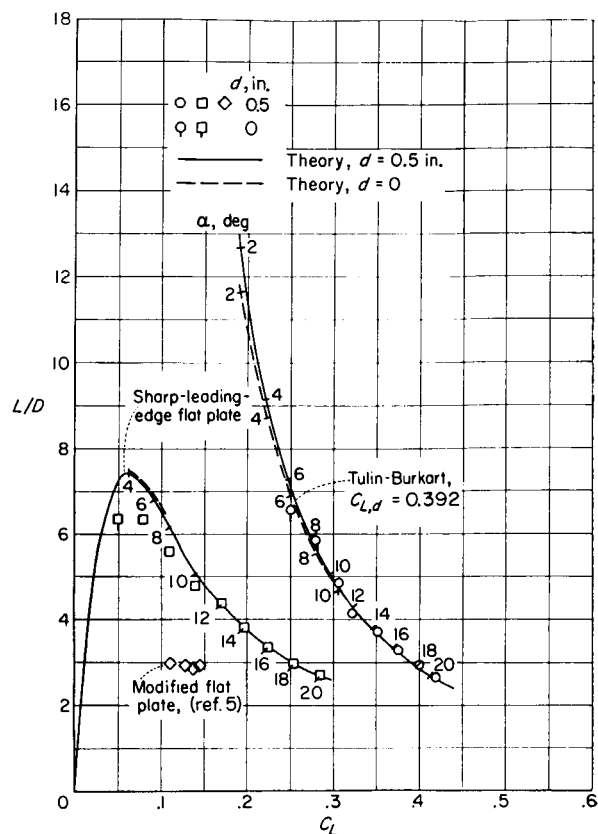
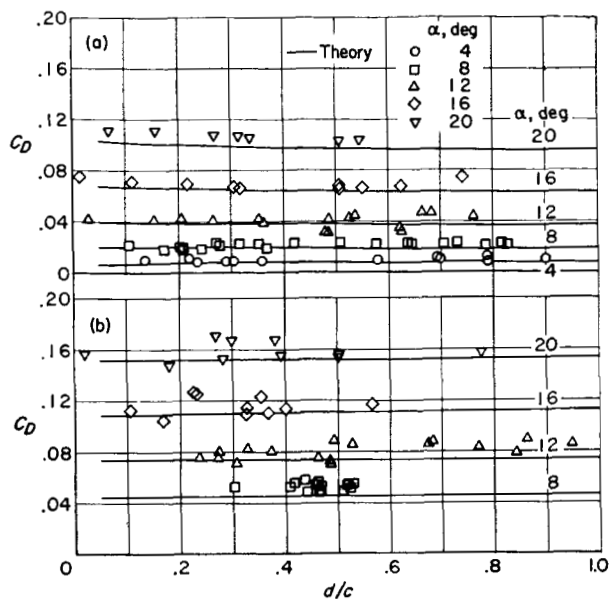


FIGURE 49.—Comparison of theoretical lift-drag ratios with experimental data obtained on the aspect-ratio-1 sharp-leading-edge flat surface and the Tulin-Burkart cambered section. Experiment and theory include skin friction, ($C_f = 0.004$). $\sigma \approx 0$.

the induced drag and skin friction; thus, it greatly influences the maximum lift-drag ratio of the section. Several other recent investigations have noted the importance of a sharp leading edge on hydrofoils designed for operation in the supercavitating regime. (See refs. 20 and 21.)

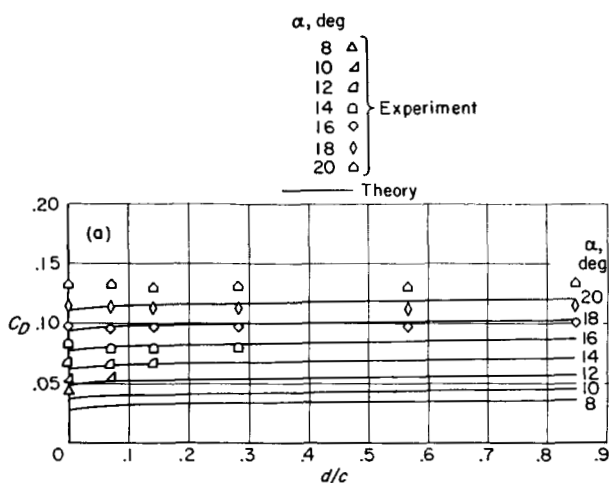
The experimental values of the drag coefficient obtained in reference 18 on the aspect-ratio-1 flat and Tulin-Burkart models are presented for comparison with theory in figures 50(a) and 50(b), respectively. The agreement between theory and experiment is very good over the range of depths and angles of attack tested.

The experimental drag-coefficient data presented in reference 19 on the aspect-ratio-1 and -3, five term sections are compared with theory in figure 51. As shown in figure 51(b) the aspect-ratio-3 data are in excellent agreement with the



(a) Flat.
(b) Tulin-Burkart; $C_{L,a}=0.392$.

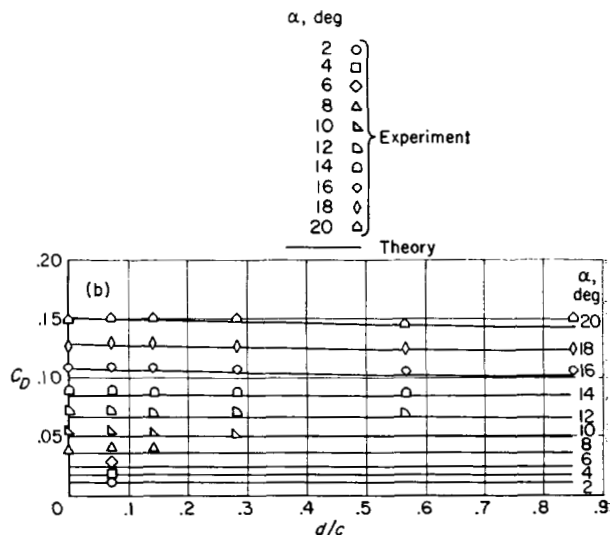
FIGURE 50.—Comparison of theoretical drag coefficients with the experimental data reported in reference 18 on aspect-ratio-1 flat and Tulin-Burkart sections. $\sigma \approx 0$.



(a) Aspect-ratio-1 five-term hydrofoil; $C_{L,a}=0.392$.

FIGURE 51.—Comparison of theoretical drag coefficients with experimental data of reference 19. $\sigma \approx 0$.

theoretical values obtained from equation (100). However, as may be seen in figure 51(a) the experimental drag coefficient for the highly cambered aspect-ratio-1 model ($C_{L,a}=0.392$) are considerably higher than the calculated values. The reason for this disagreement is probably due to the inability of a theory, which assumes small



(b) Aspect-ratio-3 five-term hydrofoil; $C_{L,a}=0.196$.

FIGURE 51.—Concluded.

camber, to predict accurately the pressure distribution when the camber is large. The linearized theory assumes that terms such as $(u/V)^2$, $(v/V)^2$ and uv/V^2 and higher order terms are small compared with unity and therefore may be neglected. It may be calculated from the linearized results given in figures 3 and 4(a) that the maximum values of $(u/V)^2$ and $(v/V)^2$ for the two-dimensional case are about 0.068 and 0.09 for the Tulin-Burkart section with $C_{L,a}=0.392$ and about 0.08 and 0.09 for the five-term section with $C_{L,a}=0.196$. On the other hand, the maximum values of $(u/V)^2$ and $(v/V)^2$ are 0.32 and 0.36 for the five-term section with $C_{L,a}=0.392$. Since the values of 0.32 and 0.36 are not small compared with unity, the assumption that these second-order terms may be neglected is not justified for the five-term section with $C_{L,a}=0.392$.

The available data are not sufficient to determine accurately the limits on the applicability of the theory. However, it is clear that the theory is applicable for all cambers for which the two-dimensional linearized theory predicts $(u/V)^2$ and $(v/V)^2$ to be less than about 0.1. On the other hand, the theory is definitely lacking in accuracy, particularly for calculating the drag coefficient, when the linearized result gives values of $(u/V)^2$ and $(v/V)^2$ greater than about 0.3.

CENTER OF PRESSURE

The center of pressure of the flat plate and the

Tulin-Burkart section as calculated from the data of figures 37 and 38 are compared with theory in figure 52. The theory from equation (113) is in good agreement with the experimental data for both models. Since the experimental accuracy of the forces and moments on the flat plate is poor at small angles of attack (small total loads) the accuracy of the center of pressure from the data obtained on the flat plate at 4° and 6° incidence is doubtful.

Center-of-pressure data as taken from reference 18 for the flat-plate and Tulin-Burkart sections are compared with theory in figures 53(a) and 53(b), respectively. The agreement between the-

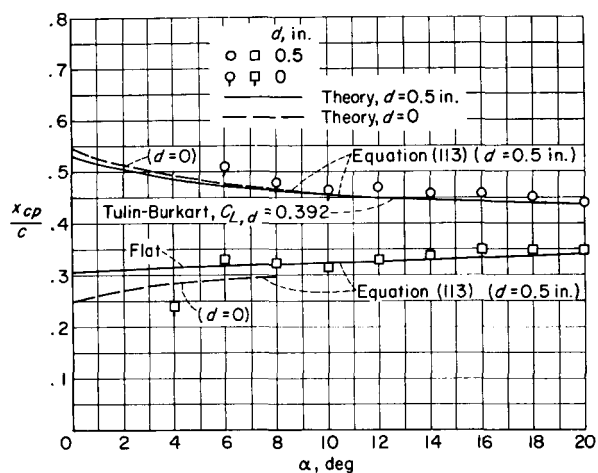


FIGURE 52.—Location of the center of pressure of aspect-ratio-1 flat and Tulin-Burkart sections. $\sigma \approx 0$.

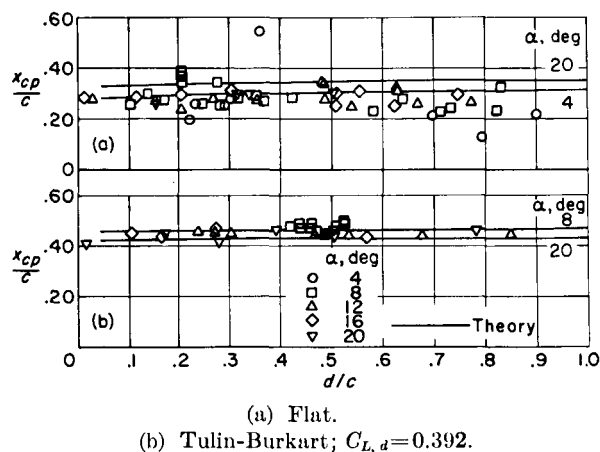
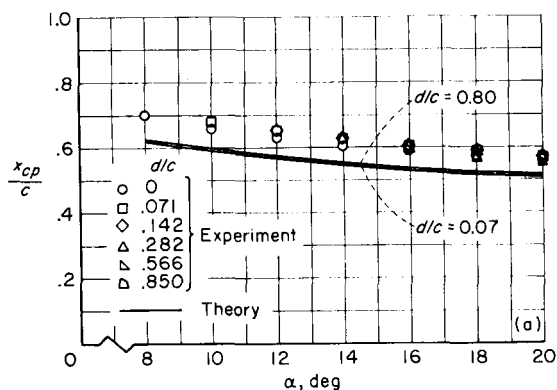


FIGURE 53.—Comparison of the theoretical location of the center of pressure with the experimental data reported in reference 18 on aspect-ratio-1 flat and Tulin-Burkart sections. $\sigma \approx 0$.

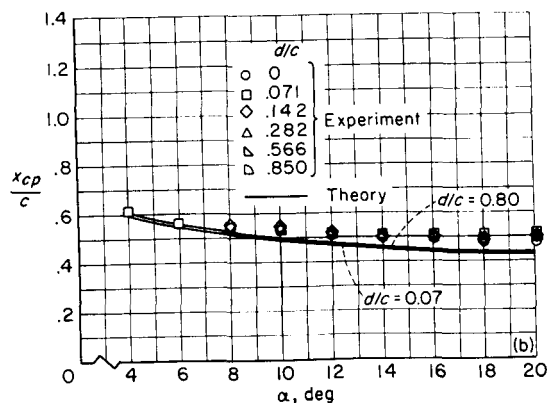
ory and experiment is good for those conditions where the upper surface of the hydrofoils was not wetted.

Experimental measurements of the center of pressure of the two five-term sections as presented in reference 19 are compared with theoretical computations in figure 54(a) for the aspect-ratio-1, $C_{L,d}=0.392$ section and in 54(b) for the aspect-ratio-3, $C_{L,d}=0.196$ section. These experimental data are higher than the theoretical predictions by about 5 percent to 15 percent. This discrepancy is probably due to the application of the crossflow lift at the midchord in equation (113). For the five-term section the crossflow is obviously concentrated on the rearward portion of the section. For cambers of the magnitude involved for these two sections, the data indicate



(a) Aspect-ratio-1 five-term hydrofoil; $C_{L,d}=0.392$.

FIGURE 54.—Comparison of theoretical ratio of center of pressure to chord $\frac{x_{cp}}{c}$ with experimental data of reference 19. $\sigma \approx 0$.



(b) Aspect-ratio-3 five-term hydrofoil; $C_{L,d}=0.196$.

FIGURE 54.—Concluded.

that application of the crossflow at, for example, 0.8 chord would be better than the midchord location assumed. However, no general expression for the center of pressure of the crossflow component of lift has been determined and, if better accuracy than that given by the midchord location is desired, the designer may make some improvement by devising some empirical relationship for the location.

CAVITY SHAPE

The slope of the upper cavity streamline has been shown in the section on theory to be directly proportional to the equivalent airfoil circulation and thus to the hydrofoil circulation. Thus the effect of aspect ratio on the slope of the upper cavity streamline of a flat plate may be given by an equation similar to equation (128); that is,

$$\tan \phi_A = \frac{A}{A+1} \tan \phi_{A=\infty} (\alpha - \alpha_i) \quad (130)$$

Thus for a given ratio of spray thickness to chord the theoretical value of the $\tan \phi_A$ at some arbitrary aspect ratio and angle of attack is obtained by finding the two-dimensional value of ϕ from figure 26 for the angle $\alpha - \alpha_i$ and then reducing the tangent of this angle by $\frac{A}{A+1}$. The theoretical spray angles for the flat-plate model operating at angles of attack of 16° and 20° which were computed by using the measured values of δ/c obtained from figure 40 are shown in figure 41 for comparison with experiment. The theoretical values are too high at very shallow depths but the agreement becomes much better as the depth becomes greater than about 0.25 chord.

Reference 18 presents further experimental data on the cavity shapes of the aspect-ratio-1 flat and Tulin-Burkart sections. Figure 55 shows the aspect-ratio-1 flat plate operating at a depth of 0.5 chord and an angle of attack of 16° . The plate had 3 pins located along the span so that the upper ends of the pins were 0.34 chord rearward of the leading edge and 0.17 chord from the lower surface of the plate. These pins were spaced 0.021, 0.198, and 0.375 chord from the right tip of the plate. From the photograph the cross section of the cavity may be estimated as shown by the solid line in figure 55(b). The horizontal short-dashed line is the calculated location of the cavity upper surface based on a uniform distribution of

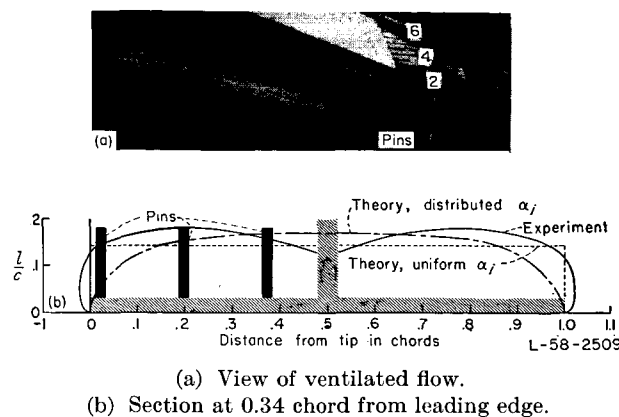


FIGURE 55.—Cavity cross section for flat plate. Aspect ratio, 1.0; $\frac{d}{c} = 0.5$; $\alpha = 16^\circ$.

α_i . The other dashed curve is the cavity cross section calculated by assuming the airfoil induced angle distribution for a rectangular plan form. (See ref. 10.) It may be noted that near the tips the cavity shape is primarily due to crossflow, whereas near the center the calculated value based on the actual distribution of induced angle of attack is more nearly correct if the cavity curvature due to the strut is neglected. The cavity shape based on uniform induced-angle distribution is about 20 percent lower than the maximum measured value.

In figure 56 the calculated cavity shapes based

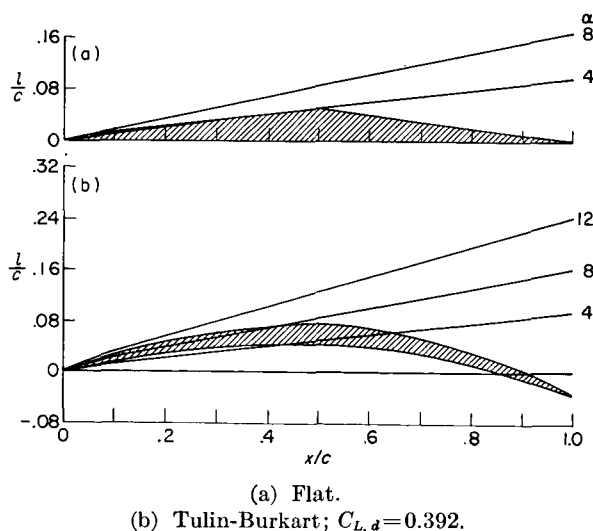


FIGURE 56.—Calculated cavity upper surface streamlines for flat and cambered models. Aspect ratio, 1.0; $\frac{d}{c} = 0.5$.

on uniform α_i are presented for the two aspect-ratio-1 hydrofoils operating at $d/c=0.5$. It may be seen in figure 56(a) that for the flat plate the calculated streamline at an angle of attack of 4° just touches the upper surface of the model. If the speed is sufficiently high, no significant negative pressure coefficient can exist in the flow field; therefore, if the forward portion of the upper surface is wetted and positive pressures occur, the lift will decrease. Thus it may be concluded from the calculations that the maximum value of the lift-drag ratio for this flat-plate hydrofoil occurs at an angle of attack of 4° . Experimental data obtained in reference 18 at speeds up to about 185 feet per second reveal that the forward portion of this flat-plate hydrofoil does become wetted at an angle of attack of about 4° . The maximum lift-drag ratio also occurred at an angle of attack of about 4° .

The hydrofoil section shown in figure 56(b) is the Tulin-Burkart model with $C_{L,d}=0.392$. The calculated location of the cavity streamline is shown for angles of attack of 4° , 8° , and 12° . It may be noted that the calculated streamlines are almost identical with those shown in figure 56(a) for the flat plate. The reason that both hydrofoils have about the same theoretical cavity streamline location is peculiar to an aspect ratio of 1. There are two compensating effects due to camber which cause this similarity in streamlines. The cambered hydrofoil cavity ordinates are increased because of the hydrofoil curvature but simultaneously the camber causes increased lift at a given angle and produces a greater induced angle of attack. The greater induced angle of attack results in a decrease in cavity ordinates and thus effectively cancels the increased ordinates contributed by the hydrofoil curvature.

Figure 56(b) indicates that ventilation from the leading edge of the cambered model will not be possible at angles less than about 10° . Experiments conducted in ventilated flow up to speeds of 180 feet per second and reported in reference 18 are in excellent agreement with this prediction; that is, at angles less than 10° the forward portion of the upper surface was wetted. However, the experimental data of reference 18 show that the maximum lift-drag ratio of the cambered model occurred at an angle of attack of about 7° to 8° . The fact that the lift-drag ratio continued to increase even with the upper surface wetted is

attributed to the curvature of the upper surface and finite speed. At a speed of 175 feet per second it is possible to support a pressure coefficient as low as -0.07 . Thus, it is possible at finite speeds for the upper surface to add to the lift and possibly decrease the drag. Theoretically, at higher speeds the maximum lift-drag ratio will occur closer to the predicted angle of attack of 10° .

THEORETICAL COMPARISON OF PRACTICAL LOW DRAG SECTIONS

The experimental data given in the preceding section indicate that a reliable approximation to the cavity streamline location on high-speed, moderate-aspect-ratio surfaces can be obtained theoretically. By using the theory developed, it is now possible to determine the best of the four section shapes when operating under practical conditions: (1) circular arc, (2) Tulin-Burkart, (3) three term, and (4) five term. The operating condition chosen for comparison was a depth of submersion of 1 chord and an aspect ratio of 3. The structural characteristics of the section were arbitrarily chosen as (1) thickness ratio $t/c=0.03$ at 0.2 chord from the leading edge and (2) $t/c=0.04$ at the chordwise location of the maximum lower surface ordinate. The leading edge and these control points were assumed to be connected by straight lines and the upper surface rearward of the latter control point was taken as parallel to the reference line of the section. Because of the almost uniform gradation of the various characteristics of the four sections, only the extremes, the circular-arc and five-term section, were compared.

Over the range of cambers from $C_{L,d}=0$ to $C_{L,d}=0.3$, the calculated cavity streamlines first touched the upper surface of the assumed hydrofoil sections at the 0.2-chord control point. Thus, the second point at the maximum lower surface ordinate did not influence the maximum lift-drag ratio of the sections. By using equations (99) and (100), the lift and drag coefficients of the sections were calculated. The friction drag coefficient was estimated to be 0.004. A plot of the variation of the lift-drag ratio with lift coefficient is presented in figure 57. Also shown in figure 57 is the line denoting the minimum angle at which the control point at 0.2 chord just clears the calculated cavity streamline. The area above this line is shaded to indicate that these regions

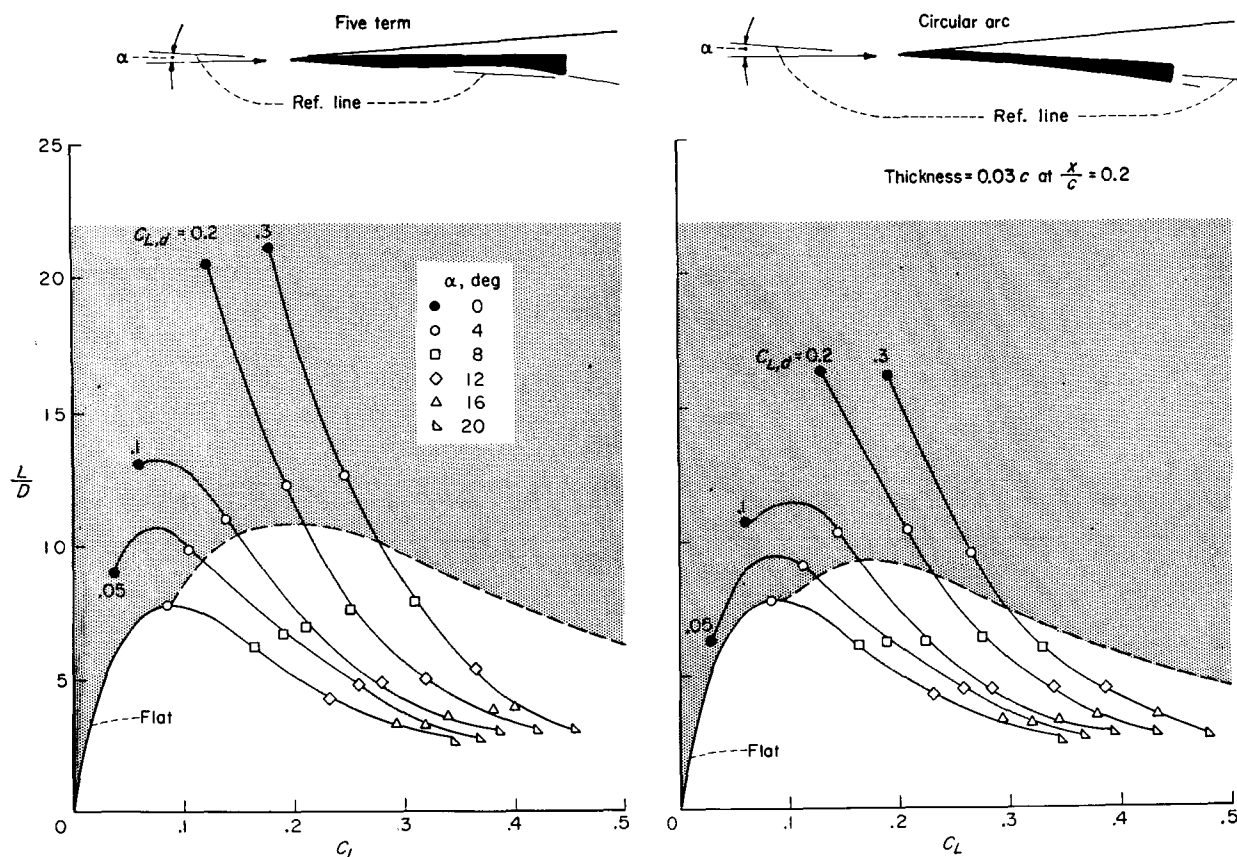


FIGURE 57.—Theoretical lift-drag ratios of five-term and circular-arc hydrofoils. Aspect ratio, 3.0; $\frac{d}{c} = 1.0$.

are not attainable under the design conditions. This line of minimum angle of attack for the structure specified is also indicated in figures 17 to 24 as the angle of attack for maximum L/D .

The regions above the dashed lines are zones where the hydrofoil cannot operate with a full cavity from the leading edge. The dashed lines should, of course, be modified when control points other than $t/c = 0.03$ at $x/c = 0.2$ are used.

The significant result shown in figure 57 is that either type of camber can give higher maximum lift-drag ratios than the flat plate. The optimum amount of camber for both hydrofoils correspond to a value of $C_{L,d}$ of about 0.1. The optimum lift coefficient is about 0.175 for both sections. The hydrofoil cross sections shown in the top of figure 57 are for $C_{L,d} = 0.1$ oriented at the minimum angle of attack revealed by the analysis. The analysis as presented in figure 57 also shows that the five-term section is superior to the circular arc. The maximum values of the lift-drag ratios are 10.5 and 9.5 for the five-term and circular-arc

sections, respectively. Although the lift-drag ratio of the five-term section is slightly higher than that of the circular arc, it is not twice as high as that predicted from the two-dimensional theory.

For an aspect-ratio-3 hydrofoil, supported by a single strut and operating at speeds of 80 knots or greater, the thickness distribution chosen for the analysis is not conservative. Therefore, the calculated maximum lift-drag ratio of about 10 at a lift coefficient of 0.175 is very near the optimum that can be obtained on a single supercavitating hydrofoil supported on one strut and operating at zero cavitation number at speeds of 80 knots or greater. More severe structural requirements than those imposed in the present analysis will reduce the maximum attainable lift-drag ratio.

CONCLUSIONS

Two supercavitating hydrofoil sections with low drag have been derived by optimizing the shape when three and five terms are assigned to the

series expansion for the vorticity distribution. The two-dimensional lift-drag ratios of the two sections operating at their design lift coefficient are theoretically about 45 and 80 percent greater than the Tulin-Burkart configuration.

The concept of combining the linearized effects of camber with nonlinear flat-plate theory has proven to be satisfactory. The results of a comparison of this theory, corrected for aspect ratio, with experimental data obtained on four low-aspect-ratio sections at zero cavitation number may be summarized as follows:

1. The theoretical lift coefficient was in excellent agreement with those obtained experimentally.

2. The theoretical drag coefficient was in excellent agreement with experimental data on all models except a highly cambered five-term section with a design lift coefficient of 0.392. The disagreement is attributed to the inability of linearized theory to predict accurately the pressure distribution when the curvature is very great.

3. The theory for the five-term section predicts centers of pressures slightly nearer the leading edge than experiment; however, the agreement may be improved by taking the center of pressure of the crossflow component rearward of the mid-chord.

4. Low-drag hydrofoils developed from the linear theory cannot operate at the orientation for which the stagnation point is at the leading edge because an upper surface cavity will not form from the leading edge even for sections with zero thickness. The theoretical cavity shapes are in sufficient agreement with experimental data to warrant their use in making calculations of the minimum angle of attack for which a cavity will form from the leading edge.

5. The theory developed is used to compare various low drag sections which are considered to be structurally adequate for zero cavitation number operation at speeds of about 80 knots when the hydrofoil has an aspect ratio of 3 and is supported by a single strut at a depth of one chord. This theoretical comparison shows that under the specified conditions the maximum lift-drag ratio obtainable is about 10. The best section for optimum lift-drag ratio is the five-term design; however, the camber profile may range from the five term to the circular arc with only about a 10 percent change in the maximum lift-drag ratio.

LANGLEY RESEARCH CENTER,
NATIONAL AERONAUTICS AND SPACE ADMINISTRATION,
LANGLEY FIELD, VA., *July 8, 1959.*

APPENDIX

SAMPLE CALCULATION OF LIFT, DRAG, AND CENTER OF PRESSURE OF A CAMBERED LIFTING SURFACE OPERATING AT FINITE DEPTH AND ZERO CAVITATION NUMBER

A sample calculation of the lift, drag, and center of pressure is presented for a Tulin-Burkart section with $A_1=0.2$ ($C_{L,a}=0.392$), having an aspect ratio of 1 and operating at an angle of attack of 12° and depth of submersion of 0.071 chord.

LIFT COEFFICIENT

STEP 1

For the Tulin-Burkart hydrofoil section ($A_2=-\frac{A_1}{2}$), from equation (7),

$$\alpha_{c,\infty} = A_1 - \frac{A_2}{2} = \frac{5A_1}{4} = 0.25$$

STEP 2

From figure 15 at $d/c=0.071$,

$$\frac{\alpha_c}{\alpha_{c,\infty}} = 0.718$$

Therefore,

$$\alpha_c = (0.718)(0.25) = 0.18$$

STEP 3

By assuming that $C_{L,1}=0.25$ and $\tau=0.12$ and by using equation (95),

$$\alpha_i = 1.12 \frac{0.25}{\pi} = 0.088$$

and

$$\alpha + \alpha_c - \alpha_i = \frac{12}{57.3} + 0.18 - 0.088 = 0.301 \text{ radian} = 17.2^\circ$$

From figure 2 for $d/c=0.071$ and $\alpha=17.2^\circ$, it is found that $m=1.63$; therefore, from reference 11, $\tau=0.12$ as assumed. By using the first term in equation (99),

$$C_{L,1} = \frac{1}{2} (1.63) (0.301) \frac{\cos 12^\circ}{\cos 17.2^\circ} = 0.251$$

This value should check with the original assumption; if not, repeat step 3 with a better approximation for C_L and τ .

STEP 4

For the Tulin-Burkart section given by equation (14) with $A_1=0.2$,

$$\frac{y}{c} (1) = -\frac{A_1}{6}$$

Therefore,

$$\alpha_o = \tan^{-1} 0.033 = 1.92^\circ$$

and

$$\alpha' = 12^\circ + 1.92^\circ = 13.92^\circ$$

$$\alpha_c = 0.18 \text{ radian} = 10.3^\circ$$

or

$$\alpha' + \alpha_c = 24.22^\circ$$

By using equation (97),

$$C_{L,c} = \frac{1}{2} 0.88 \sin^2 (24.22) \cos 13.92^\circ = 0.072$$

Thus, the required lift coefficient is

$$C_L = C_{L,1} + C_{L,c} = 0.251 + 0.072 = 0.323$$

DRAG COEFFICIENT

STEP 1

From step 3 in the lift-coefficient calculation,

$$\alpha + \alpha_c - \alpha_i = 17.2^\circ$$

For $d/c=0.071$, $m=1.63$; and for $d/c=\infty$, $m=1.2$. Therefore, from equation (110)

$$m_e = \frac{1.63}{1.2} \frac{\pi}{2} = 2.13$$

From figure 2 by using the $\alpha=0$ line with $m=2.13$,

it can be found that

$$(d/c)_e = 0.66$$

STEP 2

If a (the distance to airfoil center of pressure) is assumed to be 0.37, then from figure 13 for $a=0.37$ and $d/c=0.66$, the following values are found:

$$B_0 = 0.56$$

$$B_1 = 0.15$$

$$B_2 \approx 0$$

From equation (86) for $A_0 = \alpha - \alpha_i = 0.121$, $A_1 = 0.2$ and $A_2 = -0.1$. The values of C_0 , C_1 , and C_2 may be determined as

$$C_0 = 0.212$$

$$C_1 = 0.181$$

$$C_2 = -0.1$$

and from equation (80), $a = 0.367$, which checks with the assumed value. If the resulting value of a differs enough from the assumed value to affect the values of the B coefficients, step 2 should be repeated.

STEP 3

From equation (109) the value of ϵ is determined

as

$$\epsilon = 0.0013 \text{ radian} = 0.065^\circ$$

STEP 4

Substituting the following values

$$C_{L,1} = 0.251 \quad C_{L,e} = 0.072 \quad C_f = 0.004$$

into equation (100) yields

$$C_D = 0.251 \tan(12.065^\circ) + 0.072 \tan(13.92^\circ) + 0.004 = 0.075$$

CENTER OF PRESSURE

STEP 1

From step 2 of the drag-coefficient calculation,

$$C_0 = 0.212 \quad C_1 = 0.181 \quad C_2 = -0.1$$

Thus, from equation (111),

$$x_{cp,1} = 0.43c$$

STEP 2

From equation (113) and by using

$$C_{L,1} = 0.251$$

and

$$C_{L,e} = 0.072$$

it is found that

$$x_{cp} = 0.45c$$

REFERENCES

1. Tulin, M. P., and Burkart, M. P.: Linearized Theory for Flows About Lifting Foils at Zero Cavitation Number. Rep. C-638, David W. Taylor Model Basin, Navy Dept., Feb. 1955.
2. Green, A. E.: Note on the Gliding of a Plate on the Surface of a Stream. Proc. Cambridge Phil. Soc., vol. XXXII, pt. 2, May 1936, pp. 248-252.
3. Perry, Bryne: Experiments on Struts Piercing the Water Surface. Rep. No. E-55.1 (Contract N123s-91875), C.I.T., Hydrod. Lab., Dec. 1954. (Available from ASTIA as AD No. 56179.)
4. Eisenberg, Phillip: On the Mechanism and Prevention of Cavitation. Rep. 712, David W. Taylor Model Basin, Navy Dept., July 1950.
5. Wadlin, Kenneth L., Ramsen, John A., and Vaughan, Victor L., Jr.: The Hydrodynamic Characteristics of Modified Rectangular Flat Plates Having Aspect Ratios of 1.00, 0.25, 0.125 and Operating Near a Free Water Surface. NACA Rep. 1246, 1955. (Supersedes NACA TN's 3079 by Wadlin, Ramsen, and Vaughan and 3249 by Ramsen and Vaughan.)
6. Lamb, Horace: Hydrodynamics. Sixth ed., Dover Publications, 1945.
7. Milne-Thomson, L. M.: Theoretical Hydrodynamics. Second ed., Macmillan and Co., Ltd., 1949.
8. Rosenhead, L.: Resistance to a Barrier in the Shape of an Arc of a Circle. Proc. Roy. Soc. (London), ser. A, vol. 117, no. 777, Jan. 2, 1928, pp. 417-433.
9. Wu, T. Yao-tsu: A Free Streamline Theory for Two-Dimensional Fully Cavitated Hydrofoils. Rep. No. 21-17 (Contract N6onr-24420), C.I.T., Hydrod. Lab., July 1955.
10. Glauert, H.: The Elements of Airfoil and Airscrew Theory. Second ed., Cambridge Univ. Press, 1947. (Reprinted 1948.)
11. Wagner, Herbert: Planing of Watercraft. NACA TM 1139, 1948.
12. Wieghardt, Karl: Chordwise Load Distribution of a Simple Rectangular Wing. NACA TM 963, 1940.
13. Jones, Robert T.: Correction of the Lifting-Line Theory for the Effect of the Chord. NACA TN 817, 1941.
14. Shuford, Charles L., Jr.: A Theoretical and Experimental Study of Planing Surfaces Including Effects of Cross Section and Plan Form. NACA Rep. 1355, 1958. (Supersedes NACA TN 3939.)
15. Flax, A. H., and Lawrence, H. R.: The Aerodynamics of Low-Aspect-Ratio Wings and Wing-Body Combinations. Rep. No. CAL-37, Cornell Aero. Lab., Inc., Sept. 1951.
16. Tachmindji, A. J., Morgan, W. B., Miller, M. L., and Hecker, R.: The Design and Performance of Supercavitating Propellers. Rep. C-807, David Taylor Model Basin, Navy Dept., Feb. 1957.
17. Tulin, M. P.: Supercavitating Flow Past Foils and Struts. Cavitation in Hydrodynamics, NPL (Teddington, England), 1956, 16 p. 1-16 p. 19.
18. Christopher, Kenneth W., and Johnson, Virgil E., Jr.: Experimental Investigation of Aspect-Ratio-1 Supercavitating Hydrofoils at Speeds up to 185 Feet Per Second. NASA TN D-187, 1960.
19. McGehee, John R., and Johnson, Virgil E., Jr.: Hydrodynamic Characteristics of Two Low-Drag Supercavitating Hydrofoils. NASA MEMO 5-9-59L, 1959.
20. Parkin, Blaine R.: Experiments on Circular Arc and Flat Plate Hydrofoils in Noncavitating and Full Cavity Flows. Rep. No. 47-6 (Contract Nonr-220(12)), C.I.T., Hydrod. Lab., Feb. 1956.
21. Newman, J. N.: Supercavitating Flow Past Bodies with Finite Leading Edge Thickness. Rep. 1081, David W. Taylor Model Basin, Navy Dept., Sept. 1956.

TABLE II
CALCULATED CHARACTERISTICS OF A CIRCULAR ARC LIFTING SURFACE AT ZERO CAVITATION NUMBER

(a) $\gamma = 0.222$; $C_{L,d} = 0.196$

d/c	α , deg	Aspect ratio 1						Aspect ratio 3						Aspect ratio 5					
		α_{ti} , radi- ans	m	$C_{L,u}$	$C_{L,e}$	C_L	ϵ , radi- ans	C_D	$\frac{x_{cp}}{c}$	$\frac{x_{cp}}{c}$	ϵ , radi- ans	C_L	$C_{L,e}$	$C_{L,u}$	$C_{L,e}$	C_L	ϵ , radi- ans	C_D	$\frac{x_{cp}}{c}$
0.25	20	0.099	0.091	1.43	0.256	0.088	0.344	0.1256	0.391	0.365	0.453	0.043	0.410	0.462	0.029	0.491	-0.32	0.1746	0.358
	16		0.083	1.55	0.232	0.065	0.297	0.0865	0.392	0.368	0.409	0.032	0.377	0.426	0.022	0.448	-0.23	0.1267	0.362
	12		0.072	1.69	0.202	0.047	0.249	0.0540	0.396	0.377	0.363	0.024	0.328	0.376	0.016	0.392	-0.10	0.0829	0.371
	8		0.059	1.83	0.165	0.031	0.195	0.0290	0.408	0.389	0.293	0.016	0.274	0.314	0.010	0.324	0.06	0.0460	0.382
.5	20		0.044	1.97	0.123	0.017	0.140	0.0115	0.433	0.416	0.217	0.009	0.208	0.240	0.006	0.246	0.42	0.0192	0.410
	16			1.37	0.251	0.088	0.339	0.1238	0.394	0.368	0.446	0.044	0.402	0.452	0.029	0.481	-0.28	0.1700	0.361
	12		0.088	1.49	0.226	0.067	0.293	0.0849	0.395	0.371	0.397	0.033	0.364	0.417	0.022	0.439	-0.18	0.1226	0.365
	8		0.071	1.63	0.190	0.048	0.247	0.0530	0.399	0.379	0.347	0.024	0.323	0.366	0.016	0.382	0.06	0.0800	0.375
1.0	20		0.058	1.74	0.163	0.031	0.194	0.0281	0.411	0.392	0.283	0.016	0.267	0.307	0.010	0.317	0.11	0.0450	0.386
	16		0.043	1.86	0.122	0.018	0.140	0.0111	0.437	0.420	0.212	0.009	0.203	0.235	0.006	0.241	0.48	0.0190	0.414
	12		0.027	1.99	0.077	0.008	0.085	0.0017	0.455	0.438	0.133	0.004	0.129	0.149	0.002	0.151	---	---	---
	8		0.080	1.31	0.243	0.089	0.332	0.1201	0.397	0.371	0.434	0.044	0.390	0.444	0.030	0.474	-0.24	0.1648	0.364
2.0	20		0.080	1.43	0.222	0.068	0.290	0.0821	0.399	0.374	0.389	0.034	0.315	0.358	0.023	0.426	-0.15	0.1176	0.369
	16		0.069	1.54	0.193	0.049	0.242	0.0517	0.404	0.381	0.339	0.024	0.276	0.314	0.016	0.374	-0.01	0.0770	0.379
	12		0.057	1.65	0.159	0.032	0.191	0.0278	0.416	0.397	0.276	0.016	0.200	0.239	0.011	0.310	0.16	0.0436	0.390
	8		0.043	1.76	0.120	0.018	0.138	0.0116	0.443	0.426	0.208	0.009	0.199	0.227	0.006	0.233	0.57	0.0188	0.419
5.0	20		0.027	1.87	0.076	0.008	0.084	0.0026	0.455	0.438	0.132	0.004	0.128	0.147	0.003	0.150	1.48	0.0034	---
	16		0.087	1.27	0.238	0.089	0.327	0.1195	0.398	0.372	0.422	0.044	0.378	0.432	0.030	0.462	-0.23	0.163	0.366
	12		0.078	1.37	0.214	0.069	0.283	0.0820	0.401	0.375	0.378	0.034	0.344	0.393	0.023	0.416	-0.16	0.1170	0.370
	8		0.068	1.46	0.187	0.049	0.236	0.0519	0.406	0.383	0.327	0.024	0.303	0.347	0.016	0.363	0	0.0744	0.379
5.0	20		0.042	1.57	0.156	0.032	0.188	0.0277	0.410	0.389	0.268	0.016	0.252	0.293	0.011	0.304	0.16	0.0428	0.392
	16		0.042	1.66	0.117	0.019	0.136	0.0115	0.446	0.427	0.202	0.009	0.193	0.222	0.006	0.228	0.56	0.0183	0.421
	12		0.042	1.75	0.089	0.011	0.104	0.0026	0.455	0.438	0.132	0.004	0.128	0.147	0.003	0.150	1.48	0.0034	---
	8		0.086	1.22	0.234	0.091	0.325	0.1204	0.402	0.375	0.415	0.046	0.369	0.418	0.030	0.448	-0.22	0.1621	0.368
5.0	20		0.066	1.31	0.211	0.071	0.282	0.0824	0.405	0.380	0.374	0.035	0.324	0.366	0.024	0.410	-0.14	0.1173	0.374
	16		0.077	1.40	0.183	0.051	0.234	0.0515	0.411	0.383	0.320	0.026	0.294	0.337	0.017	0.354	-0.01	0.0733	0.383
	12		0.064	1.49	0.151	0.034	0.185	0.0278	0.424	0.386	0.262	0.017	0.245	0.281	0.011	0.292	0.15	0.0411	0.392
	8		0.041	1.58	0.115	0.020	0.135	0.0116	0.455	0.434	0.198	0.010	0.198	0.216	0.006	0.222	0.59	0.0180	0.427
5.0	20		0.026	1.67	0.074	0.009	0.083	0.0026	0.455	0.438	0.127	0.004	0.123	0.143	0.003	0.146	1.48	0.0038	---
	16			1.37	0.238	0.089	0.327	0.1195	0.398	0.372	0.422	0.044	0.378	0.432	0.030	0.462	-0.23	0.163	0.366
	12		0.078	1.37	0.214	0.069	0.283	0.0820	0.401	0.375	0.378	0.034	0.344	0.393	0.023	0.416	-0.16	0.1170	0.370
	8		0.068	1.46	0.187	0.049	0.236	0.0519	0.406	0.383	0.327	0.024	0.303	0.347	0.016	0.363	0	0.0744	0.379

TABLE II.—Concluded
CALCULATED CHARACTERISTICS OF A CIRCULAR ARC LIFTING SURFACE AT ZERO CAVITATION NUMBER

(b) $\gamma = 0.444$; $C_{L,d} = 0.392$

d/c	α , deg	α_a , radi- ans	Aspect ratio 1					Aspect ratio 3					Aspect ratio 5													
			α_a , radi- ans	m	$C_{L,1}$	$C_{L,e}$	C_L	ϵ , radi- ans	C_D	x_p , c	α_a , radi- ans	m	$C_{L,1}$	$C_{L,e}$	C_L	ϵ , radi- ans	C_D	x_p , c	α_a , radi- ans	m	$C_{L,1}$	$C_{L,e}$	C_L	ϵ , radi- ans	C_D	x_p , c
0.25	20	0.198	0.106	1.28	0.293	0.130	0.423	0.18	0.1625	0.418	0.063	1.21	0.462	0.065	0.527	0.10	0.1969	0.394	0.046	1.16	0.522	0.044	0.566	0.06	0.2085	0.386
	16		0.099	1.40	0.273	0.107	0.380	.52	.1181	.425	.059	1.33	.435	.053	.488	.34	.1461	.401	.043	1.29	.492	.036	.528	.30	.1564	.394
	12		0.089	1.52	0.249	0.085	0.334	.90	.0798	.431	.053	1.46	.401	.042	.443	.64	.1015	.410	.039	1.42	.456	.028	.484	.60	.1101	.404
	8		0.078	1.65	0.218	0.063	0.281	1.40	0.0490	.446	.047	1.59	.358	.031	.389	1.01	.0669	.421	.035	1.55	.401	.021	.431	.98	.0882	.416
.5	4		0.065	1.80	0.185	0.044	0.229	2.14	0.0262	.468	.040	1.73	.303	.022	.325	1.72	.0331	.447	.029	1.70	.346	.015	.361	1.62	0.0359	.440
	20	.20800	0.105	1.22	.288	.134	.422	.28	.1631	.421	.063	1.15	.455	.067	.522	.14	.1956	.396	.046	1.12	.514	.045	.559	.13	.2071	.389
	16		0.088	1.33	.269	.111	.380	.61	.1182	.427	.059	1.26	.428	.055	.483	.40	.1451	.403	.043	1.23	.485	.037	.522	.68	.1551	.396
	12		0.088	1.44	.245	.088	.333	1.00	.0800	.434	.053	1.38	.394	.044	.438	.70	.1007	.413	.039	1.35	.448	.029	.477	.68	.1091	.406
1.0	8		0.078	1.57	.218	.066	.284	1.51	.0494	.449	.047	1.50	.350	.033	.383	1.10	.0656	.425	.035	1.48	.402	.022	.424	1.08	.0681	.420
	4		0.065	1.68	.182	.047	.229	2.26	.0267	.470	.040	1.63	.299	.023	.322	1.81	.0333	.451	.029	1.61	.343	.016	.359	1.74	.0360	.443
	0		0.051	1.80	.143	.030	.173	---	---	---	.031	1.75	.236	.015	.251	---	---	---	.023	1.74	.273	.010	.283	---	---	---
	16	.21650	0.104	1.16	.281	.137	.418	.43	.1635	.426	.062	1.10	.446	.068	.514	.21	.1934	.399	.046	1.07	.502	.048	.548	.20	.2043	.391
2.0	16		0.096	1.26	.263	.114	.377	.70	.1185	.430	.058	1.20	.418	.057	.475	.47	.1436	.406	.042	1.17	.473	.036	.541	.47	.1530	.398
	12		0.087	1.37	.241	.091	.332	1.08	.0806	.437	.052	1.30	.383	.046	.429	.81	.0994	.417	.038	1.28	.437	.030	.467	.79	.1074	.409
	8		0.077	1.49	.214	.069	.283	1.60	.0499	.452	.046	1.43	.345	.035	.380	1.23	.0630	.430	.034	1.40	.392	.023	.415	1.20	.0881	.424
	4		0.065	1.59	.180	.049	.229	2.38	.0264	.473	.039	1.53	.292	.024	.316	1.93	.0334	.455	.029	1.64	.338	.016	.354	1.85	.0367	.447
5.0	0		0.051	1.70	.143	.032	.175	3.65	.0109	---	.031	1.65	.234	.016	.250	3.02	.0132	---	.023	1.64	.270	.011	.281	2.92	.0143	---
	20	.222	0.103	1.12	.276	.139	.415	.40	.1635	.427	.062	1.05	.438	.069	.507	.22	.1920	.400	.046	1.01	.494	.046	.540	.20	.2037	.392
	16		0.095	1.20	.257	.116	.373	.70	.1181	.430	.057	1.13	.408	.058	.466	.50	.1428	.407	.042	1.11	.463	.038	.501	.47	.1518	.399
	12		0.086	1.31	.234	.093	.327	1.06	.0805	.439	.052	1.23	.373	.047	.420	.84	.0990	.418	.038	1.21	.428	.031	.459	.79	.1069	.411
5.0	8		0.076	1.42	.208	.071	.279	1.60	.0500	.453	.045	1.35	.334	.036	.373	1.28	.0607	.432	.034	1.32	.382	.023	.405	1.20	.0674	.425
	4		0.064	1.53	.175	.051	.226	2.33	.0270	.475	.039	1.47	.287	.025	.312	1.97	.0338	.456	.028	1.44	.330	.016	.346	1.84	.0362	.448
	20	.23075	0.101	1.07	.272	.142	.414	.41	.1620	.430	.060	1.02	.430	.071	.501	.31	.1896	.403	.045	1.00	.487	.048	.535	19	.1995	.395
	16		0.093	1.16	.254	.119	.373	.70	.1177	.436	.056	1.11	.404	.060	.464	.59	.1411	.411	.041	1.09	.458	.040	.498	.47	.1494	.404
5.0	12		0.085	1.25	.232	.096	.328	1.05	.0798	.444	.051	1.20	.370	.048	.418	.95	.0962	.422	.038	1.18	.421	.032	.453	.77	.1042	.415
	8		0.073	1.34	.207	.074	.281	1.57	.0494	.458	.045	1.30	.331	.037	.368	1.41	.0622	.438	.033	1.28	.377	.025	.402	1.20	.0660	.430
	4		0.063	1.43	.174	.053	.227	2.35	.0261	.477	.038	1.40	.284	.026	.310	2.06	.0335	.460	.028	1.37	.322	.018	.340	1.83	.0351	.455
	0		0.050	1.52	.140	.035	.175	3.62	.0108	---	.030	1.49	.228	.018	.246	3.18	.0136	---	.023	1.48	.262	.012	.274	2.92	.0140	---

TABLE III
CALCULATED CHARACTERISTICS OF A TULIN-BURKART LIFTING SURFACE AT ZERO CAVITATION NUMBER

(a) $A_1=0.1$; $C_{L,d}=0.196$

d/c	α , deg	α_{ti} radi- ans	Aspect ratio 1						Aspect ratio 3						Aspect ratio 5										
			m	$C_{L,1}$	$C_{L,c}$	C_L	ϵ radi- ans	C_D	$\frac{x_{cp}}{c}$	α_{ti} radi- ans	m	$C_{L,1}$	$C_{L,c}$	C_L	ϵ radi- ans	C_D	$\frac{x_{cp}}{c}$	α_{ti} radi- ans	m	$C_{L,1}$	$C_{L,c}$	C_L	ϵ radi- ans	C_D	$\frac{x_{cp}}{c}$
0.25	20	0.094	0.093	0.256	0.081	0.337	-0.80	0.1205	0.397	0.066	1.38	0.407	0.041	0.447	-0.86	0.1570	0.372	0.040	1.35	0.462	0.027	0.489	-0.89	0.1697	0.363
	16		0.158	0.230	0.061	0.291	-70	0.0815	0.399	0.051	1.51	0.373	0.030	0.403	-79	0.1105	0.377	0.036	1.48	0.424	0.023	0.444	-79	0.1227	0.372
	12		0.171	0.204	0.042	0.242	-52	0.0602	0.406	0.043	1.65	0.326	0.021	0.347	-62	0.0709	0.387	0.032	1.62	0.373	0.014	0.388	-63	0.0785	0.383
	8		0.184	0.164	0.027	0.191	-23	0.0298	0.424	0.036	1.79	0.271	0.013	0.285	-37	0.0380	0.404	0.026	1.77	0.309	0.009	0.318	-41	0.0428	0.401
.5	4		0.042	0.122	0.014	0.136	32	0.0104	0.461	0.027	1.94	0.201	0.007	0.209	10	0.0155	0.440	0.023	1.92	0.235	0.004	0.239	10	0.0176	0.440
	20	.10038	0.091	0.309	0.083	0.333	-78	0.1190	0.399	0.054	1.32	0.398	0.042	0.440	-82	0.1544	0.374	0.040	1.29	0.451	0.028	0.479	-87	0.1688	0.366
	16		0.081	0.225	0.063	0.288	-66	0.0811	0.402	0.049	1.44	0.363	0.031	0.394	-74	0.0986	0.380	0.036	1.41	0.412	0.021	0.433	-75	0.1189	0.375
	12		0.071	0.197	0.044	0.241	-45	0.0497	0.409	0.042	1.57	0.319	0.022	0.344	-56	0.0700	0.390	0.031	1.54	0.364	0.015	0.379	-60	0.0772	0.387
1.0	8		0.067	0.174	0.028	0.188	-35	0.0264	0.428	0.035	1.70	0.265	0.014	0.279	-32	0.0376	0.408	0.026	1.67	0.302	0.009	0.311	-38	0.0423	0.404
	4		0.045	0.129	0.015	0.135	36	0.0104	0.462	0.026	1.83	0.199	0.008	0.207	17	0.0152	0.444	0.019	1.82	0.231	0.005	0.246	13	0.0174	0.441
	0		0.026	0.074	0.006	0.080	---	---	---	---	0.16	1.97	0.003	0.128	---	---	---	0.012	1.95	0.144	0.002	0.146	---	---	---
	20	.10475	0.080	0.233	0.064	0.298	-75	0.1177	0.404	0.053	1.26	0.387	0.042	0.429	-79	0.1508	0.370	0.039	1.24	0.440	0.028	0.468	-84	0.1637	0.372
2.0	16		0.079	0.220	0.044	0.284	-59	0.0801	0.407	0.048	1.37	0.352	0.032	0.384	-67	0.1062	0.385	0.035	1.35	0.402	0.021	0.423	-70	0.1163	0.370
	12		0.068	0.191	0.029	0.236	-47	0.0496	0.417	0.042	1.50	0.311	0.023	0.334	-51	0.0885	0.366	0.031	1.48	0.356	0.015	0.371	-55	0.0758	0.392
	8		0.056	0.157	0.016	0.186	-22	0.0260	0.434	0.034	1.63	0.256	0.014	0.270	-23	0.0372	0.416	0.025	1.59	0.295	0.010	0.305	-30	0.0414	0.410
	4		0.042	0.118	0.010	0.134	41	0.0105	0.466	0.026	1.73	0.195	0.008	0.203	22	0.0151	0.450	0.019	1.72	0.225	0.005	0.230	15	0.0188	0.445
5.0	0		0.026	0.074	0.006	0.080	1.55	0.0021	0.488	0.016	1.86	0.124	0.003	0.127	1.29	0.0028	0.450	0.012	1.85	0.144	0.002	0.146	1.15	0.0029	0.445
	20	.110	0.087	0.236	0.085	0.321	-75	0.1177	0.405	0.052	1.22	0.376	0.042	0.418	-78	0.1495	0.380	0.039	1.19	0.429	0.028	0.457	-83	0.1622	0.373
	16		0.077	0.214	0.065	0.279	-59	0.0800	0.407	0.047	1.32	0.342	0.032	0.374	-66	0.1082	0.385	0.034	1.29	0.392	0.021	0.413	-73	0.1155	0.380
	12		0.067	0.196	0.046	0.232	-47	0.0490	0.417	0.041	1.42	0.302	0.023	0.325	-49	0.0677	0.419	0.030	1.40	0.346	0.015	0.361	-59	0.0752	0.392
5.0	8		0.055	0.158	0.029	0.181	-20	0.0269	0.434	0.034	1.53	0.250	0.014	0.264	-20	0.0370	0.419	0.024	1.51	0.288	0.010	0.298	-31	0.0415	0.411
	4		0.041	0.118	0.016	0.134	40	0.0103	0.468	0.026	1.64	0.190	0.008	0.198	23	0.0150	0.455	0.019	1.62	0.220	0.005	0.225	14	0.0170	0.447
	20	.11400	0.085	0.233	0.088	0.321	-77	0.1148	0.410	0.051	1.16	0.368	0.044	0.412	-72	0.1454	0.384	0.037	1.14	0.417	0.029	0.446	-82	0.1563	0.379
	16		0.076	0.210	0.067	0.277	-60	0.0782	0.413	0.046	1.26	0.336	0.033	0.369	-61	0.1025	0.386	0.034	1.25	0.384	0.022	0.406	-70	0.1119	0.385
5.0	12		0.064	0.182	0.048	0.230	-42	0.0553	0.422	0.040	1.35	0.293	0.024	0.317	-43	0.0694	0.403	0.030	1.35	0.358	0.016	0.354	-55	0.0722	0.397
	8		0.054	0.150	0.031	0.181	-18	0.0255	0.443	0.033	1.45	0.244	0.016	0.260	-15	0.0390	0.424	0.024	1.44	0.280	0.010	0.290	-30	0.0395	0.418
	4		0.041	0.138	0.017	0.131	18	0.0103	0.477	0.025	1.56	0.188	0.009	0.197	13	0.0150	0.461	0.018	1.55	0.216	0.006	0.222	15	0.0162	0.454
	0		0.026	0.074	0.008	0.082	1.55	0.0021	0.488	0.016	1.66	0.122	0.004	0.126	1.40	0.0031	0.461	0.012	1.65	0.141	0.002	0.143	1.15	0.0029	0.445

TABLE III.—Concluded

CALCULATED CHARACTERISTICS OF A TULIN-BURKART LIFTING SURFACE AT ZERO CAVITATION NUMBER

(b) $A_1=0.2$; $C_{L,d}=0.392$

d/c	α_i , deg	α_i , radi-ans	Aspect ratio 1						Aspect ratio 3						Aspect ratio 5											
			m	$C_{L,1}$	$C_{L,e}$	C_L	ϵ_i , radi-ans	C_D	$\frac{x_{cp}}{c}$	α_i , radi-ans	m	$C_{L,1}$	$C_{L,e}$	C_L	ϵ_i , radi-ans	C_D	$\frac{x_{cp}}{c}$	α_i , radi-ans	m	$C_{L,1}$	$C_{L,e}$	C_L	ϵ_i , radi-ans	C_D	$\frac{x_{cp}}{c}$	
0.25	20	0.191	0.105	1.28	0.288	0.120	0.408	-0.67	0.1495	0.430	0.062	1.21	0.456	0.059	0.515	-0.89	0.1818	0.407	0.046	1.18	0.518	0.040	0.558	-0.94	0.1945	0.400
	16		0.097	1.41	0.269	0.097	0.366	-0.35	0.1098	0.437	0.059	1.33	0.432	0.047	0.479	-0.59	0.1345	0.414	0.042	1.30	0.493	0.032	0.520	-0.66	0.1438	0.408
	12		0.087	1.53	0.246	0.075	0.321	-0.02	0.0708	0.446	0.053	1.47	0.395	0.036	0.431	-0.25	0.0913	0.427	0.039	1.43	0.460	0.023	0.475	-0.30	0.0985	0.421
	8		0.076	1.67	0.216	0.055	0.271	0.62	0.0422	0.463	0.047	1.61	0.352	0.026	0.378	0.25	0.0538	0.446	0.034	1.57	0.389	0.018	0.417	0.16	0.0608	0.439
.5	4		0.063	1.81	0.180	0.037	0.217	1.52	0.0210	0.493	0.039	1.75	0.296	0.018	0.314	1.02	0.0283	0.474	0.029	1.72	0.340	0.011	0.351	0.97	0.0307	0.466
	20	0.20075	0.104	1.23	0.285	0.124	0.369	-0.61	0.1501	0.434	0.062	1.16	0.451	0.060	0.513	-0.85	0.1807	0.409	0.046	1.14	0.513	0.041	0.554	-0.88	0.1930	0.402
	16		0.097	1.34	0.266	0.101	0.367	-0.27	0.1076	0.442	0.058	1.27	0.424	0.049	0.474	-0.48	0.1345	0.416	0.042	1.24	0.480	0.034	0.514	-0.56	0.1427	0.411
	12		0.087	1.45	0.242	0.079	0.321	-0.11	0.0713	0.451	0.053	1.39	0.389	0.039	0.428	-0.17	0.0910	0.430	0.039	1.36	0.442	0.026	0.468	-0.18	0.0978	0.424
1.0	8		0.076	1.58	0.214	0.058	0.272	0.69	0.0428	0.467	0.046	1.52	0.347	0.029	0.376	0.32	0.0555	0.449	0.034	1.48	0.393	0.019	0.412	0.29	0.0905	0.442
	4		0.064	1.70	0.179	0.039	0.218	1.38	0.0216	0.497	0.039	1.64	0.292	0.020	0.312	1.13	0.0284	0.477	0.029	1.63	0.338	0.013	0.351	1.10	0.0309	0.470
	0		0.049	1.81	0.139	0.024	0.163	3.11	0.0083	0.500	0.030	1.77	0.230	0.012	0.242	0.242	0.0000	0.500	0.022	1.75	0.264	0.008	0.272	0.242	0.0000	0.470
	20	0.20950	0.103	1.17	0.279	0.127	0.406	-0.51	0.1498	0.438	0.062	1.11	0.442	0.064	0.506	-0.76	0.1799	0.412	0.045	1.08	0.498	0.042	0.541	-0.78	0.1908	0.405
2.0	16		0.095	1.27	0.260	0.104	0.364	-0.20	0.1073	0.445	0.057	1.22	0.418	0.052	0.470	-0.44	0.1331	0.421	0.042	1.18	0.468	0.035	0.503	-0.48	0.1413	0.416
	12		0.086	1.38	0.238	0.082	0.320	-0.21	0.0717	0.455	0.052	1.32	0.381	0.041	0.422	-0.04	0.0908	0.435	0.038	1.20	0.432	0.027	0.459	-0.11	0.0976	0.429
	8		0.076	1.51	0.212	0.060	0.272	0.76	0.0432	0.471	0.046	1.44	0.340	0.030	0.370	0.46	0.0559	0.454	0.034	1.42	0.389	0.020	0.409	0.37	0.0607	0.447
	4		0.063	1.60	0.177	0.041	0.218	1.67	0.0218	0.500	0.038	1.55	0.288	0.021	0.309	1.24	0.0285	0.484	0.028	1.53	0.330	0.014	0.344	1.18	0.0313	0.477
5.0	0		0.049	1.70	0.138	0.025	0.163	3.13	0.0084	0.500	0.030	1.66	0.227	0.013	0.240	2.57	0.0106	0.500	0.022	1.65	0.262	0.008	0.270	2.49	0.0117	0.477
	20	0.219	0.102	1.12	0.274	0.131	0.405	-0.44	0.1495	0.440	0.061	1.07	0.435	0.067	0.502	-0.73	0.1790	0.413	0.045	1.04	0.490	0.043	0.533	-0.78	0.1900	0.406
	16		0.094	1.22	0.255	0.107	0.362	-0.16	0.1075	0.446	0.057	1.17	0.408	0.053	0.461	-0.40	0.1320	0.422	0.041	1.13	0.460	0.035	0.495	-0.48	0.1411	0.417
	12		0.085	1.31	0.233	0.085	0.318	-0.30	0.0720	0.456	0.052	1.26	0.373	0.041	0.414	-0.01	0.0903	0.436	0.037	1.23	0.424	0.028	0.452	-0.12	0.0971	0.430
0	8		0.075	1.42	0.210	0.064	0.274	1.87	0.0434	0.473	0.046	1.37	0.332	0.031	0.363	0.49	0.0557	0.455	0.033	1.35	0.382	0.021	0.403	0.36	0.0600	0.449
	4		0.063	1.51	0.176	0.044	0.220	1.77	0.0220	0.502	0.038	1.46	0.283	0.021	0.304	1.24	0.0290	0.485	0.028	1.45	0.325	0.015	0.340	1.18	0.0312	0.478
	20	0.22800	0.100	1.07	0.270	0.134	0.404	-0.45	0.1497	0.441	0.060	1.03	0.431	0.067	0.498	-0.65	0.1783	0.417	0.044	1.00	0.484	0.045	0.529	-0.80	0.1866	0.409
	16		0.093	1.16	0.252	0.111	0.363	-0.05	0.1079	0.451	0.055	1.10	0.398	0.055	0.453	-0.28	0.1300	0.428	0.041	1.09	0.456	0.037	0.493	-0.48	0.1384	0.422
0	12		0.084	1.25	0.230	0.088	0.318	-0.38	0.0723	0.461	0.051	1.20	0.368	0.044	0.412	-0.12	0.0897	0.442	0.037	1.18	0.418	0.029	0.447	-0.13	0.0951	0.436
	8		0.074	1.35	0.205	0.066	0.271	0.98	0.0440	0.477	0.045	1.30	0.329	0.033	0.362	0.61	0.0555	0.459	0.033	1.28	0.374	0.022	0.396	0.37	0.0589	0.454
	4		0.063	1.44	0.174	0.046	0.220	1.88	0.0227	0.506	0.038	1.39	0.280	0.023	0.303	1.49	0.0293	0.492	0.028	1.38	0.321	0.015	0.336	1.18	0.0307	0.485
	0		0.049	1.52	0.138	0.029	0.167	3.38	0.0091	0.500	0.030	1.49	0.225	0.015	0.240	2.81	0.0115	0.500	0.022	1.48	0.259	0.010	0.269	2.49	0.0116	0.485

TABLE IV
CALCULATED CHARACTERISTICS OF A THREE-TERM LIFTING SURFACE AT ZERO CAVITATION NUMBER

(a) $A_1=0.0833$; $C_{L,d}=0.196$

d/c	α , deg	α_i , radians	Aspect ratio 1						Aspect ratio 3						Aspect ratio 5											
			α_i radi- ans	m	$CL_{L,1}$	$CL_{L,c}$	CL_L	ϵ_i radi- ans	C_D	$\frac{x_{cp}}{c}$	α_i radi- ans	m	$CL_{L,1}$	$CL_{L,c}$	CL_L	ϵ_i radi- ans	C_D	$\frac{x_{cp}}{c}$	α_i radi- ans	m	$CL_{L,1}$	$CL_{L,c}$	CL_L	ϵ_i radi- ans	C_D	$\frac{x_{cp}}{c}$
			Aspect ratio 1							Aspect ratio 3							Aspect ratio 5									
0.25	20	0.094	0.092	1.46	0.254	0.074	0.328	-1.56	0.1108	0.420	1.38	0.407	0.037	0.444	-1.58	0.1481	0.401	0.041	1.34	0.458	0.024	0.482	-1.67	0.1613	0.394	
	16		0.082	1.59	0.230	0.054	0.284	-1.42	0.0749	0.428	1.52	0.372	0.027	0.399	-1.48	0.1084	0.412	0.037	1.48	0.421	0.018	0.439	-1.53	0.1129	0.404	
	12		0.071	1.73	0.201	0.037	0.238	-1.21	0.0453	0.445	1.66	0.327	0.018	0.345	-1.32	0.0652	0.427	0.032	1.62	0.373	0.012	0.385	-1.38	0.0728	0.421	
	8		0.057	1.86	0.164	0.022	0.186	-0.81	0.0238	0.478	1.80	0.269	0.011	0.280	-0.92	0.0340	0.457	0.026	1.77	0.310	0.008	0.318	-1.04	0.0880	0.449	
	4		0.042	1.98	0.120	0.010	0.130	-0.13	0.0080	0.542	1.95	0.203	0.006	0.209	-0.42	0.0128	0.517	0.020	1.93	0.233	0.004	0.237	-0.46	0.0142	0.509	
.5	20	0.099	0.080	1.39	0.249	0.075	0.324	-1.54	0.1098	0.424	1.32	0.397	0.038	0.435	-1.58	0.1452	0.404	0.040	1.29	0.449	0.025	0.474	-1.67	0.1588	0.397	
	16		0.081	1.51	0.228	0.055	0.281	-1.36	0.0740	0.432	1.44	0.362	0.028	0.390	-1.44	0.1015	0.415	0.036	1.41	0.411	0.018	0.429	-1.52	0.1119	0.408	
	12		0.070	1.63	0.196	0.038	0.234	-1.14	0.0450	0.449	1.57	0.318	0.019	0.337	-1.28	0.0638	0.431	0.026	1.55	0.364	0.012	0.376	-1.32	0.0716	0.425	
	8		0.056	1.74	0.159	0.023	0.182	-0.76	0.0230	0.462	1.83	0.263	0.011	0.274	-0.96	0.0351	0.463	0.025	1.68	0.302	0.008	0.310	-1.00	0.0881	0.455	
	4		0.041	1.83	0.117	0.011	0.128	-0.04	0.0091	0.544	1.97	0.198	0.006	0.204	-0.36	0.0128	0.522	0.019	1.82	0.229	0.004	0.233	-0.40	0.0143	0.514	
1.0	20	0.104	0.088	1.33	0.244	0.077	0.321	-1.52	0.1086	0.428	1.27	0.388	0.038	0.426	-1.58	0.1429	0.406	0.039	1.25	0.442	0.026	0.468	-1.67	0.1555	0.400	
	16		0.080	1.45	0.221	0.057	0.278	-1.32	0.0737	0.436	1.38	0.353	0.028	0.381	-1.40	0.0908	0.419	0.035	1.36	0.403	0.019	0.422	-1.50	0.1094	0.413	
	12		0.068	1.54	0.190	0.039	0.229	-1.10	0.0445	0.453	1.50	0.300	0.019	0.329	-1.24	0.0629	0.436	0.031	1.48	0.355	0.013	0.368	-1.25	0.0700	0.430	
	8		0.056	1.65	0.156	0.024	0.180	-0.70	0.0237	0.468	1.61	0.256	0.012	0.268	-0.91	0.0324	0.468	0.025	1.59	0.293	0.008	0.301	-0.95	0.0873	0.461	
	4		0.042	1.77	0.117	0.012	0.129	-0.04	0.0090	0.533	1.73	0.194	0.006	0.200	-0.31	0.0128	0.528	0.019	1.72	0.224	0.004	0.228	-0.35	0.0145	0.520	
2.0	20	0.108	0.087	1.27	0.238	0.078	0.316	-1.52	0.1079	0.430	1.24	0.378	0.038	0.416	-1.56	0.1412	0.408	0.038	1.21	0.432	0.026	0.458	-1.64	0.1530	0.402	
	16		0.078	1.38	0.216	0.058	0.274	-1.33	0.0730	0.438	1.34	0.344	0.028	0.372	-1.40	0.0889	0.420	0.034	1.32	0.393	0.019	0.412	-1.50	0.1078	0.415	
	12		0.068	1.48	0.188	0.039	0.227	-1.10	0.0440	0.455	1.43	0.302	0.019	0.321	-1.22	0.0620	0.438	0.030	1.44	0.347	0.013	0.360	-1.25	0.0692	0.432	
	8		0.054	1.57	0.151	0.024	0.175	-0.71	0.0235	0.491	1.64	0.248	0.012	0.260	-0.88	0.0320	0.470	0.025	1.54	0.287	0.008	0.295	-0.96	0.0876	0.464	
	4		0.042	1.68	0.114	0.012	0.126	-0.04	0.0091	0.551	1.66	0.190	0.006	0.196	-0.28	0.0127	0.531	0.019	1.66	0.218	0.004	0.222	-0.36	0.0146	0.524	
5.0	20	0.113	0.085	1.21	0.231	0.080	0.311	-1.52	0.1054	0.437	1.17	0.370	0.040	0.410	-1.51	0.1377	0.414	0.037	1.13	0.413	0.026	0.439	-1.70	0.1459	0.406	
	16		0.076	1.31	0.209	0.059	0.268	-1.35	0.0712	0.444	1.27	0.337	0.030	0.367	-1.40	0.0960	0.425	0.034	1.24	0.380	0.020	0.400	-1.50	0.1089	0.420	
	12		0.065	1.39	0.181	0.041	0.222	-1.10	0.0432	0.464	1.36	0.294	0.021	0.315	-1.14	0.0605	0.447	0.029	1.34	0.334	0.014	0.348	-1.27	0.0662	0.441	
	8		0.054	1.49	0.150	0.026	0.176	-0.72	0.0225	0.499	1.58	0.243	0.013	0.256	-0.80	0.0324	0.479	0.024	1.44	0.279	0.008	0.287	-0.95	0.0856	0.474	
	4		0.040	1.58	0.113	0.013	0.126	0	0.0087	0.561	1.66	0.187	0.007	0.194	-0.19	0.0128	0.541	0.018	1.55	0.215	0.004	0.219	-0.35	0.0140	0.537	
	0		0.026	1.68	0.073	0.005	0.078	1.25	0.0016	0.601	1.66	0.121	0.002	0.123	1.14	0.0024	0.612	0.012	1.67	0.141	0.002	0.143	0.92	0.0023	0.597	

TABLE IV.—Concluded

CALCULATED CHARACTERISTICS OF A THREE-TERM LIFTING SURFACE AT ZERO CAVITATION NUMBER

(b) $A_1 = 0.1667; C_{L,d} = 0.392$

d/c	α , deg	α_i , radi- ans	Aspect ratio 1						Aspect ratio 3						Aspect ratio 5											
			α_i , radi- ans	m	$C_{L,1}$	$C_{L,e}$	C_L	ϵ_i , radi- ans	C_D	$\frac{x_p}{c}$	α_i , radi- ans	m	$C_{L,1}$	$C_{L,e}$	C_L	ϵ_i , radi- ans	C_D	$\frac{x_p}{c}$	α_i , radi- ans	m	$C_{L,1}$	$C_{L,e}$	C_L	ϵ_i , radi- ans	C_D	$\frac{x_p}{c}$
			Aspect ratio 1								Aspect ratio 3								Aspect ratio 5							
0.25	20	0.187	0.105	1.29	0.287	0.102	0.389	-2.00	0.1286	0.464	0.063	1.22	0.454	0.051	0.505	-2.26	0.1630	0.449	0.046	1.18	0.515	0.034	0.549	-2.31	0.1760	0.443
	16		0.086	1.42	0.269	0.080	0.349	-1.62	0.0903	0.480	0.058	1.34	0.429	0.040	0.469	-1.91	0.1181	0.465	0.043	1.31	0.486	0.027	0.513	-1.97	0.1279	0.400
	12		0.088	1.55	0.245	0.059	0.304	-1.06	0.0590	0.504	0.052	1.47	0.393	0.029	0.422	-1.45	0.0790	0.488	0.039	1.44	0.447	0.020	0.467	-1.53	0.0867	0.480
	8		0.076	1.67	0.214	0.041	0.255	-0.26	0.0342	0.540	0.046	1.61	0.360	0.020	0.380	-0.81	0.0467	0.520	0.034	1.58	0.395	0.014	0.409	-0.90	0.0510	0.512
.5	4		0.063	1.80	0.178	0.025	0.203	0.89	0.0164	0.593	0.038	1.75	0.292	0.012	0.304	0.13	0.0220	0.572	0.028	1.73	0.336	0.008	0.344	0.07	0.0245	0.561
	20	0.198	0.104	1.23	0.284	0.106	0.390	-1.95	0.1292	0.471	0.062	1.17	0.452	0.053	0.505	-2.19	0.1620	0.452	0.045	1.13	0.506	0.036	0.542	-2.21	0.1750	0.446
	16		0.096	1.35	0.266	0.084	0.350	-1.52	0.0908	0.484	0.058	1.28	0.423	0.042	0.465	-1.83	0.1180	0.469	0.043	1.25	0.480	0.028	0.508	-1.89	0.1275	0.463
	12		0.087	1.46	0.241	0.063	0.304	-0.97	0.0590	0.506	0.052	1.39	0.386	0.031	0.417	-1.37	0.0791	0.492	0.038	1.36	0.438	0.021	0.459	-1.42	0.0862	0.484
1.0	8		0.076	1.58	0.212	0.043	0.255	-0.17	0.0344	0.541	0.046	1.52	0.344	0.022	0.366	-0.70	0.0468	0.524	0.034	1.49	0.391	0.014	0.406	-0.76	0.0510	0.517
	4		0.063	1.70	0.177	0.027	0.204	1.03	0.0170	0.596	0.038	1.65	0.290	0.014	0.304	0.29	0.0222	0.575	0.028	1.63	0.334	0.009	0.343	0.20	0.0250	0.566
	0		0.048	1.82	0.137	0.014	0.151	0.00	0.0000	0.600	0.030	1.77	0.226	0.007	0.233	0.00	0.0000	0.575	0.022	1.76	0.262	0.005	0.267	0.00	0.0250	0.566
	20	0.207	0.103	1.18	0.280	0.110	0.380	-1.83	0.1298	0.473	0.061	1.11	0.440	0.055	0.495	-2.13	0.1609	0.456	0.045	1.09	0.500	0.037	0.537	-2.10	0.1742	0.450
2.0	16		0.094	1.27	0.259	0.087	0.346	-1.42	0.0908	0.488	0.057	1.22	0.416	0.044	0.460	-1.76	0.1172	0.473	0.042	1.19	0.470	0.029	0.509	-1.80	0.1267	0.468
	12		0.085	1.37	0.235	0.066	0.301	-0.88	0.0590	0.510	0.052	1.33	0.393	0.033	0.414	-1.29	0.0785	0.496	0.038	1.30	0.432	0.022	0.454	-1.31	0.0857	0.488
	8		0.072	1.50	0.210	0.046	0.256	-0.08	0.0349	0.543	0.045	1.45	0.340	0.023	0.363	-0.60	0.0470	0.529	0.033	1.42	0.386	0.015	0.401	-0.67	0.0516	0.524
	0		0.062	1.60	0.175	0.029	0.204	1.20	0.0175	0.600	0.038	1.55	0.285	0.015	0.300	0.38	0.0226	0.579	0.028	1.54	0.329	0.010	0.339	0.30	0.0252	0.571
5.0	4		0.048	1.70	0.137	0.016	0.153	2.85	0.0071	0.600	0.030	1.67	0.225	0.008	0.233	2.01	0.0081	0.581	0.022	1.66	0.261	0.005	0.266	1.84	0.0085	0.571
	20	0.217	0.104	1.13	0.274	0.114	0.388	-1.82	0.1295	0.475	0.060	1.08	0.436	0.056	0.492	-2.10	0.1606	0.458	0.045	1.05	0.494	0.037	0.531	-2.12	0.1728	0.451
	16		0.094	1.23	0.256	0.089	0.345	-1.43	0.0909	0.490	0.056	1.18	0.412	0.044	0.456	-1.72	0.1171	0.475	0.041	1.15	0.464	0.030	0.494	-1.81	0.1256	0.470
	12		0.084	1.32	0.232	0.068	0.300	-0.89	0.0590	0.512	0.051	1.28	0.376	0.034	0.410	-1.24	0.0782	0.498	0.038	1.27	0.427	0.022	0.449	-1.32	0.0855	0.491
0	8		0.072	1.43	0.206	0.048	0.254	-0.08	0.0349	0.545	0.045	1.38	0.335	0.024	0.359	-0.55	0.0470	0.531	0.033	1.37	0.382	0.016	0.398	-0.68	0.0513	0.526
	4		0.062	1.52	0.175	0.030	0.205	1.20	0.0173	0.601	0.038	1.50	0.284	0.016	0.300	0.04	0.0225	0.582	0.028	1.47	0.327	0.011	0.338	0.29	0.0250	0.574
	0		0.052	1.62	0.144	0.021	0.166	0.00	0.0073	0.600	0.030	1.67	0.225	0.008	0.233	2.01	0.0081	0.581	0.022	1.66	0.261	0.005	0.264	1.85	0.0085	0.574
	20	0.226	0.100	1.08	0.271	0.117	0.388	-1.85	0.1292	0.479	0.060	1.03	0.429	0.058	0.487	-2.10	0.1600	0.462	0.044	1.00	0.482	0.039	0.521	-2.12	0.1689	0.455
0	16		0.092	1.16	0.251	0.094	0.345	-1.45	0.0910	0.496	0.056	1.12	0.403	0.047	0.450	-1.96	0.1161	0.481	0.041	1.09	0.453	0.031	0.484	-1.80	0.1231	0.476
	12		0.084	1.25	0.229	0.071	0.300	-0.89	0.0590	0.518	0.051	1.21	0.369	0.036	0.405	-1.07	0.0780	0.506	0.037	1.19	0.419	0.024	0.443	-1.32	0.0837	0.501
	8		0.074	1.35	0.204	0.051	0.255	-0.10	0.0346	0.549	0.045	1.31	0.329	0.026	0.357	-0.41	0.0470	0.539	0.033	1.29	0.375	0.017	0.392	-0.68	0.0503	0.533
	0		0.062	1.44	0.172	0.033	0.205	1.20	0.0175	0.604	0.038	1.40	0.280	0.017	0.297	0.62	0.0235	0.591	0.028	1.38	0.319	0.011	0.330	0.30	0.0246	0.580
0	4		0.049	1.52	0.137	0.019	0.156	0.00	0.0073	0.600	0.030	1.49	0.224	0.010	0.234	2.28	0.0091	0.581	0.022	1.49	0.258	0.006	0.264	1.85	0.0084	0.584

TABLE V
CALCULATED CHARACTERISTICS OF A FIVE-TERM LIFTING SURFACE AT ZERO CAVITATION NUMBER

(a) $A_1=0.075$; $C_{L,d}=0.196$

d/c	α_i , deg	α_i , radi-ans	Aspect ratio 1										Aspect ratio 3										Aspect ratio 5									
			α_i , radi-ans	m	$C_{L,1}$	$C_{L,e}$	C_L	ϵ , radi-ans	C_D	$\frac{x_p}{c}$	α_i , radi-ans	m	$C_{L,1}$	$C_{L,e}$	C_L	ϵ , radi-ans	C_D	$\frac{x_p}{c}$	α_i , radi-ans	m	$C_{L,1}$	$C_{L,e}$	C_L	ϵ , radi-ans	C_D	$\frac{x_p}{c}$						
0.25	20	0.092	0.092	1.46	0.255	0.066	0.321	-1.93	0.1049	0.446	-1.93	0.1049	0.446	-1.93	1.39	0.407	0.032	0.439	-2.02	0.1425	0.430	-2.02	0.1425	0.430	-2.02	0.1425	0.430					
	16	0.083	0.083	1.59	0.229	0.047	0.276	-1.76	0.0705	0.462	-1.76	0.0705	0.462	-1.91	1.52	0.369	0.023	0.392	-1.91	0.0990	0.445	-1.91	0.0990	0.445	-1.93	0.1102	0.437					
	12	0.071	0.071	1.72	0.200	0.031	0.211	-1.50	0.0425	0.490	-1.50	0.0425	0.490	-1.67	1.65	0.324	0.015	0.359	-1.67	0.0616	0.457	-1.67	0.0616	0.457	-1.69	0.0892	0.465					
	8	0.057	0.057	1.86	0.165	0.017	0.152	-1.12	0.0215	0.539	-1.12	0.0215	0.539	-1.32	1.81	0.268	0.008	0.276	-1.32	0.0320	0.517	-1.32	0.0320	0.517	-1.38	0.0861	0.509					
.5	20	0.097	0.097	1.39	0.248	0.068	0.316	-1.89	0.1038	0.449	-1.89	0.1038	0.449	-1.99	1.33	0.398	0.034	0.432	-1.99	0.1400	0.434	-1.99	0.1400	0.434	-1.93	0.1544	0.429					
	16	0.081	0.081	1.52	0.225	0.048	0.273	-1.71	0.0699	0.466	-1.71	0.0699	0.466	-1.87	1.45	0.362	0.024	0.386	-1.87	0.0976	0.449	-1.87	0.0976	0.449	-1.86	0.1077	0.442					
	12	0.069	0.069	1.63	0.194	0.032	0.226	-1.42	0.0422	0.495	-1.42	0.0422	0.495	-1.63	1.57	0.316	0.016	0.332	-1.63	0.0606	0.477	-1.63	0.0606	0.477	-1.61	0.0831	0.471					
	8	0.056	0.056	1.75	0.159	0.018	0.177	-1.07	0.0215	0.544	-1.07	0.0215	0.544	-1.28	1.70	0.261	0.009	0.270	-1.28	0.0316	0.522	-1.28	0.0316	0.522	-1.25	0.0858	0.516					
1.0	20	0.102	0.102	1.27	0.242	0.072	0.312	-1.85	0.1018	0.454	-1.85	0.1018	0.454	-1.96	1.33	0.394	0.034	0.418	-1.96	0.1364	0.438	-1.96	0.1364	0.438	-1.90	0.1514	0.432					
	16	0.088	0.088	1.40	0.220	0.050	0.270	-1.63	0.0690	0.472	-1.63	0.0690	0.472	-1.82	1.38	0.352	0.025	0.377	-1.82	0.0951	0.454	-1.82	0.0951	0.454	-1.80	0.1057	0.448					
	12	0.068	0.068	1.55	0.190	0.033	0.223	-1.32	0.0417	0.502	-1.32	0.0417	0.502	-1.59	1.50	0.309	0.016	0.325	-1.59	0.0636	0.482	-1.59	0.0636	0.482	-1.51	0.0973	0.476					
	8	0.055	0.055	1.66	0.156	0.019	0.175	-1.05	0.0210	0.549	-1.05	0.0210	0.549	-1.21	1.61	0.254	0.009	0.263	-1.21	0.0310	0.529	-1.21	0.0310	0.529	-1.20	0.0954	0.523					
2.0	20	0.105	0.105	1.29	0.239	0.070	0.309	-1.85	0.1009	0.456	-1.85	0.1009	0.456	-1.94	1.22	0.376	0.034	0.410	-1.94	0.1356	0.440	-1.94	0.1356	0.440	-1.90	0.1491	0.434					
	16	0.087	0.087	1.40	0.216	0.050	0.266	-1.64	0.0681	0.473	-1.64	0.0681	0.473	-1.80	1.34	0.346	0.025	0.371	-1.80	0.0941	0.467	-1.80	0.0941	0.467	-1.80	0.1044	0.450					
	12	0.067	0.067	1.50	0.187	0.033	0.220	-1.33	0.0411	0.506	-1.33	0.0411	0.506	-1.56	1.45	0.305	0.016	0.321	-1.56	0.0632	0.481	-1.56	0.0632	0.481	-1.52	0.0666	0.479					
	8	0.055	0.055	1.60	0.155	0.019	0.174	-1.04	0.0208	0.553	-1.04	0.0208	0.553	-1.16	1.59	0.250	0.009	0.259	-1.16	0.0312	0.535	-1.16	0.0312	0.535	-1.21	0.0850	0.528					
5.0	20	0.112	0.112	1.22	0.232	0.072	0.304	-1.87	0.0996	0.462	-1.87	0.0996	0.462	-1.90	1.17	0.369	0.036	0.405	-1.90	0.1324	0.445	-1.90	0.1324	0.445	-1.90	0.1436	0.441					
	16	0.076	0.076	1.32	0.210	0.053	0.263	-1.64	0.0671	0.479	-1.64	0.0671	0.479	-1.74	1.27	0.336	0.026	0.362	-1.74	0.0921	0.464	-1.74	0.0921	0.464	-1.80	0.1011	0.458					
	12	0.066	0.066	1.40	0.181	0.035	0.216	-1.34	0.0403	0.517	-1.34	0.0403	0.517	-1.45	1.36	0.293	0.018	0.311	-1.45	0.0677	0.488	-1.45	0.0677	0.488	-1.52	0.0642	0.491					
	8	0.054	0.054	1.49	0.149	0.021	0.170	-1.05	0.0204	0.568	-1.05	0.0204	0.568	-1.04	1.46	0.244	0.010	0.254	-1.04	0.0309	0.551	-1.04	0.0309	0.551	-1.24	0.0839	0.544					
0	20	0.040	0.040	1.58	0.113	0.010	0.123	-1.20	0.0082	0.648	-1.20	0.0082	0.648	-1.43	1.65	0.185	0.005	0.190	-1.43	0.0119	0.630	-1.43	0.0119	0.630	-1.62	0.0129	0.623					
	16	0.026	0.026	1.68	0.073	0.003	0.076	-1.42	0.0019	0.685	-1.42	0.0019	0.685	-1.01	1.66	0.120	0.001	0.121	-1.01	0.0022	0.655	-1.01	0.0022	0.655	-1.59	0.0129	0.623					
	12	0.026	0.026	1.68	0.073	0.003	0.076	-1.42	0.0019	0.685	-1.42	0.0019	0.685	-1.01	1.66	0.120	0.001	0.121	-1.01	0.0022	0.655	-1.01	0.0022	0.655	-1.59	0.0129	0.623					
	8	0.026	0.026	1.68	0.073	0.003	0.076	-1.42	0.0019	0.685	-1.42	0.0019	0.685	-1.01	1.66	0.120	0.001	0.121	-1.01	0.0022	0.655	-1.01	0.0022	0.655	-1.59	0.0129	0.623					

TABLE V.—Concluded
CALCULATED CHARACTERISTICS OF A FIVE-TERM LIFTING SURFACE AT ZERO CAVITATION NUMBER

(b) $A_1=0.150$; $C_{L,d}=0.392$

d/c	α , deg	α_i , radi-ans	Aspect ratio 1							Aspect ratio 3							Aspect ratio 5									
			α_i , radi-ans	m	CL_{L1}	$CL_{L,e}$	CL	ϵ_i , radi-ans	C_D	$\frac{x_{cp}}{c}$	α_i , radi-ans	m	CL_{L1}	$CL_{L,e}$	CL	ϵ_i , radi-ans	C_D	$\frac{x_{cp}}{c}$	α_i , radi-ans	m	CL_{L1}	$CL_{L,e}$	CL	ϵ_i , radi-ans	C_D	$\frac{x_{cp}}{c}$
0.25	20	0.183	0.104	1.29	0.286	0.085	0.371	-2.69	0.1140	0.509	0.062	1.21	0.452	0.043	0.495	-2.97	0.1505	0.493	0.045	1.18	0.514	0.028	0.542	-3.05	0.1648	0.489
	16		0.097	1.42	0.267	0.064	0.331	-2.27	0.0792	0.534	0.058	1.34	0.427	0.032	0.459	-2.52	0.1087	0.521	0.042	1.31	0.484	0.022	0.524	-2.94	0.1508	0.516
	12		0.086	1.54	0.242	0.044	0.286	-1.65	0.0509	0.570	0.052	1.48	0.391	0.022	0.413	-2.03	0.0720	0.554	0.039	1.46	0.448	0.015	0.463	-2.15	0.1198	0.546
	8		0.075	1.67	0.212	0.028	0.240	-1.77	0.0291	0.620	0.046	1.61	0.345	0.014	0.359	-1.30	0.0412	0.601	0.034	1.58	0.393	0.010	0.403	-1.43	0.0780	0.592
.5	20		0.062	1.80	0.175	0.016	0.191	-.40	0.0140	0.703	0.038	1.75	0.290	0.007	0.297	-1.16	0.0195	0.671	0.028	1.73	0.352	0.006	0.338	-.40	0.0210	0.661
	16	0.194	0.103	1.23	0.281	0.089	0.370	-2.63	0.1140	0.512	0.067	1.17	0.448	0.045	0.493	-2.94	0.1496	0.495	0.045	1.14	0.506	0.030	0.536	-2.94	0.1635	0.495
	12		0.096	1.35	0.264	0.068	0.332	-2.19	0.0791	0.537	0.057	1.28	0.420	0.034	0.454	-2.46	0.1079	0.525	0.047	1.25	0.476	0.023	0.499	-2.56	0.1185	0.522
	8		0.086	1.46	0.239	0.048	0.287	-1.57	0.0510	0.575	0.052	1.40	0.385	0.024	0.409	-1.93	0.0718	0.560	0.038	1.38	0.446	0.016	0.466	-2.06	0.0786	0.556
1.0	20		0.075	1.59	0.211	0.031	0.242	-.80	0.0299	0.621	0.046	1.53	0.342	0.015	0.357	-1.22	0.0416	0.606	0.038	1.49	0.387	0.010	0.397	-1.38	0.0460	0.596
	16		0.062	1.70	0.175	0.019	0.192	-.49	0.0140	0.704	0.038	1.66	0.288	0.008	0.296	-1.12	0.0195	0.678	0.028	1.64	0.331	0.006	0.337	-.53	0.0212	0.666
	4		0.048	1.83	0.135	0.007	0.142	----	----	----	0.029	1.78	0.223	0.004	0.227	----	----	----	0.022	1.77	0.258	0.002	0.260	----	----	----
	0																									
2.0	20	0.204	0.102	1.18	0.278	0.093	0.371	-2.55	0.1144	0.516	0.061	1.11	0.437	0.046	0.483	-2.80	0.1489	0.504	0.045	1.09	0.466	0.031	0.528	-2.85	0.1623	0.502
	16		0.094	1.27	0.257	0.071	0.328	-2.08	0.0791	0.542	0.057	1.22	0.412	0.035	0.447	-2.38	0.1076	0.530	0.042	1.19	0.466	0.024	0.490	-2.48	0.1172	0.525
	12		0.085	1.39	0.236	0.051	0.287	-1.46	0.0512	0.576	0.051	1.33	0.378	0.025	0.403	-1.84	0.0714	0.565	0.038	1.30	0.428	0.017	0.451	-1.95	0.0783	0.559
	8		0.075	1.51	0.209	0.033	0.242	-.72	0.0301	0.622	0.045	1.44	0.335	0.016	0.351	-1.13	0.0415	0.611	0.033	1.43	0.385	0.011	0.396	-1.31	0.0466	0.601
5.0	20		0.062	1.59	0.172	0.019	0.191	-.59	0.0139	0.707	0.038	1.56	0.284	0.009	0.293	-.07	0.0195	0.683	0.028	1.54	0.325	0.006	0.331	-0.24	0.0214	0.672
	16		0.048	1.72	0.136	0.008	0.144	2.68	0.0081	----	0.029	1.67	0.223	0.004	0.227	1.80	0.0073	----	0.022	1.66	0.257	0.003	0.260	1.53	0.0069	----
	12		0.101	1.13	0.272	0.095	0.367	-2.54	0.1144	0.518	0.060	1.06	0.434	0.047	0.481	-2.78	0.1496	0.506	0.044	1.04	0.492	0.032	0.544	-2.82	0.1620	0.503
	8	0.214	0.093	1.22	0.256	0.073	0.329	-2.07	0.0793	0.546	0.057	1.16	0.406	0.036	0.442	-2.35	0.1070	0.532	0.042	1.14	0.462	0.024	0.486	-2.44	0.1167	0.528
5.0	20		0.083	1.32	0.252	0.053	0.285	-1.36	0.0510	0.580	0.051	1.26	0.374	0.026	0.379	-1.80	0.0711	0.568	0.038	1.24	0.422	0.017	0.439	-1.89	0.0782	0.564
	16		0.074	1.43	0.206	0.034	0.240	-.62	0.0300	0.628	0.045	1.37	0.331	0.017	0.342	-1.08	0.0417	0.614	0.033	1.36	0.380	0.011	0.391	-1.24	0.0490	0.604
	12		0.062	1.52	0.172	0.020	0.192	-.70	0.0140	0.712	0.038	1.48	0.282	0.010	0.292	0	0.0200	0.687	0.028	1.46	0.322	0.006	0.328	-.18	0.0219	0.676
	8		0.049	1.68	0.136	0.011	0.147	2.89	0.0062	----	0.030	1.49	0.222	0.005	0.227	2.05	0.0083	----	0.044	1.01	0.485	0.033	0.518	-2.73	0.1612	0.507
5.0	20	0.224	0.100	1.08	0.270	0.100	0.370	-2.40	0.1148	0.522	0.060	1.03	0.428	0.050	0.478	-2.70	0.1478	0.511	0.044	1.01	0.485	0.033	0.518	-2.73	0.1612	0.507
	16		0.092	1.16	0.250	0.077	0.327	-1.88	0.0798	0.550	0.056	1.12	0.401	0.039	0.440	-2.23	0.1067	0.539	0.041	0.99	0.452	0.029	0.476	-2.31	0.1168	0.536
	12		0.084	1.26	0.230	0.056	0.286	-1.30	0.0515	0.584	0.050	1.21	0.367	0.028	0.395	-1.66	0.0710	0.576	0.037	1.19	0.417	0.019	0.438	-1.66	0.0788	0.578
	8		0.074	1.35	0.203	0.038	0.241	-.43	0.0298	0.635	0.045	1.31	0.328	0.019	0.347	-.90	0.0422	0.624	0.033	1.29	0.373	0.013	0.386	-1.06	0.0465	0.615
5.0	20		0.062	1.44	0.172	0.023	0.195	-1.06	0.0153	0.730	0.038	1.40	0.278	0.011	0.289	-.24	0.0207	0.699	0.028	1.38	0.317	0.008	0.325	-.03	0.0226	0.687
	16		0.049	1.52	0.136	0.011	0.147	2.89	0.0062	----	0.030	1.49	0.222	0.005	0.227	2.05	0.0083	----	0.022	1.49	0.257	0.004	0.261	1.77	0.0082	----
	12																									
	8																									
5.0	20																									
	16																									
	12																									
	8																									
5.0	20																									
	16																									
	12																									
	8																									
5.0	20																									
	16																									
	12																									
	8																									
5.0	20																									
	16																									
	12																									
	8																									
5.0	20																									
	16																									
	12																									
	8																									
5.0	20																									
	16																									
	12																									
	8																								</	